

AN ANALYTICAL AND EXPERIMENTAL STUDY OF
REFRACTIVE INDEX AND ABSORPTION CHANGES IN GaAs/AlGaAs
DH AND MQW DEVICES FOR OPTOELECTRONIC INTEGRATION

By
SANG SUN LEE

A DISSERTATION PRESENTED TO THE GRADUATE SCHOOL
OF THE UNIVERSITY OF FLORIDA
IN PARTIAL FULFILLMENT OF THE REQUIREMENTS
FOR THE DEGREE OF DOCTOR OF PHILOSOPHY

UNIVERSITY OF FLORIDA

1990

UNIVERSITY OF FLORIDA LIBRARIES

DEDICATED TO MY PARENTS AND LATE MOTHER-IN-LAW

ACKNOWLEDGMENTS

I wish to express my deep gratitude to my adviser Professor Ramu V. Ramaswamy, for his guidance, encouragement, and support throughout the course of this work. His leadership is directly responsible for the completion of this work without any interruption.

Several other professors provided valuable advisement and assistance. I would like to thank Professor Ramakant Srivastava for useful discussions and the well-organized operation of the Photonics Research Laboratory. He also served on my supervisory committee. I would also like to thank Professors Peter Zory, Dorothy E. Burk, and Timothy Anderson for their participation on my supervisory committee. I am deeply indebted to Dr. Luis Figueroa of the Boing High Technology Electronics Center who had been my adviser for more than one year. His enthusiasm stimulated my first interest in semiconductor optical devices. I am also grateful to Dr. V. S. Sundaram of the Boing High Technology Electronics Center for growing the first set of epitaxial layers.

I have to recognize other individuals who have provided invaluable assistance. I wish to thank Mr. James Chamblee and Mr. Jim Hales of the Microelectronics Laboratory for all the technical assistance they provided over the years.

Thanks are extended to my fellow graduate students, Hsing-Cheng, Song Jae Lee, Sang Kook Han, Hyoun Soo Kim, Ron Slocumb, Kirk Lewis, Chris Hussel, Amalia Millou, and Jamal Natour for helpful discussions. I

would especially like to thank Mr. Young-Soon Kim for his endless supply of MOCVD epitaxial layers, and his assistance in the various optical measurements. In addition, I wish to express my appreciation to my friends, Dr. Jae-Hoon Kim, Dr. Doo-Whan Lee, Mr. Jin-Young Choi, Mr. Young S. Park, and Mr. Gyu C. Hwang, whose encouragement as well as useful discussion made my stay at the University of Florida more memorable.

Lastly, but not the least, I am greatly indebted to my parents, my wife, daughter and son, my sisters and brother for their endless love, patience and confidence in the successful completion of this work, and support during all the years of this study. In particular, I wish to thank my late mother-in-law. Her devotional care and encouragement will be kept in my mind forever.

TABLE OF CONTENTS

	PAGE
ACKNOWLEDGMENTS.....	ii
ABSTRACT.....	vii
CHAPTER	
ONE INTRODUCTION.....	1
1.1. Necessity of Laser-Modulator Integration.....	1
1.2. Outline of The Present Work.....	4
1.2.1. Device Application of Optical Properties.....	5
1.2.2. Reduction of Semiconductor Laser Linewidth.....	6
1.2.3. High-Speed DH Phase Modulator.....	9
1.2.4. Integration of Laser and Phase Modulator.....	14
TWO OPTICAL PROPERTIES OF GaAs BULK AND QUANTUM WELL.....	19
2.1. Introduction.....	19
2.2. Absorption in Bulk GaAs.....	20
2.3. Refractive Index of Bulk GaAs	29
2.4. Quantum-Confining Stark Effect.....	37
THREE REFRACTIVE INDEX CHANGES IN GaAs P-N JUNCTION.....	48
3.1. Introduction.....	48
3.2. Forward Biased Condition.....	49
3.2.1. Free Carrier Plasma Effect.....	51
3.2.2. Band Shift Effect.....	52
3.3. Reverse Biased Condition.....	54
3.3.1. Carrier Depletion Effect.....	56
3.3.2. Linear Electro-Optic Effect.....	57
3.3.3. Quadratic Electro-Optic Effect.....	60
FOUR LASER GEOMETRY DEPENDENCE OF LINewidth IN (AlGa)As DIODE LASERS.....	62
4.1. Introduction.....	62

4.2.	Analytical Model for Linewidth Enhancement Factor....	64
4.3.	Laser Geometry Dependences.....	69
4.3.1.	Lasing Photon Energy, Gain Change, and Refractive Index Change.....	73
4.3.2.	Linewidth Enhancement Factor.....	78
4.3.3.	Linewidth.....	87
4.4.	Conclusion.....	89
FIVE	ANALYSIS AND OPTIMIZATION OF DH WAVEGUIDE PHASE MODULATOR.....	91
5.1.	Introduction.....	91
5.2.	Phase Shift in P-p-i-n-N Modulator.....	95
5.2.1.	Depletion Region and Electric Field.....	95
5.2.2.	Optical Field.....	100
5.2.3.	Phase Shift of Propagating Mode.....	102
5.3.	Fabrication and Characterization.....	105
5.4.	Result and Discussion.....	107
5.4.1.	Comparisons of Theory and Experiment.....	111
5.4.2.	Wavelength Dependence.....	117
5.4.3.	Carrier Concentration Dependence.....	121
5.4.4.	Intrinsic Layer Thickness Dependence.....	124
5.4.5.	Cut-Off Frequency and Power/Bandwidth.....	128
5.5.	Conclusion.....	132
SIX	NOVEL MQW STRUCTURE FOR LASER-PHASE MODULATOR INTEGRATED DEVICE.....	134
6.1.	Introduction.....	134
6.2.	Design Considerations for Laser-Modulator Integration.....	136
6.3.	Novel MQW Structure for Laser-Phase Modulator Integration.....	140
6.4.	Asymmetric SQW Laser.....	144
6.5.	Transverse MQW Intensity Modulator.....	148
6.6.	MQW Waveguide Phase Modulator.....	158
SEVEN	SUMMARY AND RECOMMENDATION.....	162
7.1.	Summary.....	162
7.2.	Recommendation for Further Study.....	167
7.2.1.	Completion of the SQW Laser- MQW Phase Modulator Integration.....	167
7.2.2.	Applications to Other Material Systems.....	169
7.2.3.	Future Study for Laser-Modulator Integration.....	171
REFERENCES.....	173	
BIOGRAPHICAL SKETCH.....	185	

Abstract of Dissertation Presented to the Graduate School
of the University of Florida in Partial Fulfillment of the
Requirements for the Degree of Doctor of Philosophy

AN ANALYTICAL AND EXPERIMENTAL STUDY OF
REFRACTIVE INDEX AND ABSORPTION CHANGES IN GaAs/AlGaAs
DH AND MQW DEVICES FOR OPTOELECTRONIC INTEGRATION

By

SANG SUN LEE

August 1990

Chairman: Ramu V. Ramaswamy
Major Department; Electrical Engineering

This dissertation describes the development of novel GaAs/AlGaAs double-heterostructures (DH) and multiple quantum-well (MQW) structures for high-speed lasers, phase modulators, and integrated devices, utilizing the refractive index and absorption changes in these structures. Theoretical analyses and experimental measurements have been performed on lasers and phase modulators in order to improve their operating characteristics and to develop efficient device structures.

In a laser-modulator integrated device, the laser is operated at constant injection current level. One of the important properties of such a light source is narrow linewidth for large modulation bandwidth. Analytical expressions for the linewidth are developed in terms of linewidth enhancement factor as a function of active layer thickness, laser length, facet reflectivity, and the type of laser structure. Thin active layer is found

more practical for the reduction of linewidth than the normally used approach of long cavity length and high facet reflectivity. The results show that a reduction of active layer thickness from 0.2 to 0.05 μm causes a reduction in the linewidth by a factor of 10.

A novel high-speed P-p-i-n-N GaAs/AlGaAs DH waveguide phase modulator is proposed, analyzed and tested. The model explains the phase modulation results in terms of the refractive index changes. An optimized high speed GaAs/AlGaAs waveguide phase modulator with phase shift efficiencies of 82 and 37.5 °/V.mm for the TE₀ mode at $\lambda = 1.06$ and 1.3 μm , respectively, while preserving low junction capacitance, has been developed. The cut-off frequency for π -phase shift is estimated to be about 4 GHz at $\lambda = 1.06 \mu\text{m}$ for a modulation voltage of 5V. It is shown that the p- and n-GaAs buffer layers in these structures are responsible for the high efficiencies, where we utilize the higher-order effects in GaAs rather than in AlGaAs as is the case with conventional modulators while keeping the applied electric field within the p-i-n GaAs active region.

A novel MQW structure for laser-phase modulator integration is proposed. This scheme utilizes either angled reactive ion etching (ARIE) or impurity induced disordering (IID), but without the complex epitaxial growth and fabrication techniques often encountered in integration of these devices. The proposed structure consists of 100 \AA single quantum-well (SQW) and 50 \AA MQW's, which serve as active layers for laser and phase modulator, respectively. A very low threshold current density of 0.577 KA/cm² in the 100 \AA SQW laser is demonstrated. Absorption measurements in 50 \AA MQW layers have been performed. These well sizes have been determined in order to ensure both high phase shift efficiency and sufficient wavelength detuning.

CHAPTER ONE INTRODUCTION

The advent of room-temperature semiconductor diode lasers stimulated significant interest in the development of semiconductor passive and active optical devices such as waveguides, modulators, couplers, switches, splitters, and detectors. This lead to the incorporation of these devices into potential monolithic opto-electronic integrated circuits (OEIC's) [Tie77, Wad87] which consist of high-speed optical and electronic devices on the same semiconductor substrate. In these circuits, optical signals are generated, modulated, transmitted, detected, and sometimes converted into electrical signals and vice versa. It is commonly believed that their performances should be superior to both electronic integrated circuits and hybrid OEIC's since optical circuits are characterized by low noise and abundant capacity of information bandwidth. Moreover, recent advances in material growth technologies such as molecular beam epitaxy (MBE) [Gos86] and metalorganic chemical vapor deposition (MOCVD) [Lud85] have rendered realization of these devices more feasible by providing fine semiconductor materials and precisely controlled structures.

1.1. Necessity of Laser-Modulator Integration

It is the laser-modulator integration that has been one of the most demanding tasks in OEIC's. There are three main reasons why integrated

devices with external laser modulation are more useful than directly modulated lasers: First, the modulation bandwidth can be increased to the tens of GHz range. Recent results of the external modulation have shown 3-dB bandwidths of 10 - 20 GHz [Wak89,Wan87], and phase modulators made of multiple quantum-well (MQW) structures [Zuc88a] have demonstrated the potential for higher bandwidths. On the other hand, the practical direct modulation bandwidth (without chirping i.e., change in lasing wavelength) of semiconductor lasers is commonly accepted to be in the lower gigahertz (< 1 - 2 GHz) range and is limited by the relaxation oscillation resonance. Even though it might be increased up to ~ 5 GHz, this is only possible at high current levels (more than twice as much as the threshold current), causing a lifetime reduction of the lasers by a factor of more than 10 and a severe restriction on the integration of a large number of lasers.

Second, large frequency chirping occurs when semiconductor lasers are modulated directly [Kis82, Tuc85]. It becomes larger as modulation speed increases. The chirp causes an enhancement of the laser linewidth and a decrease in the transmission bit rate when modulated light travels through a dispersive medium such as optical fiber. A remarkable reduction of the chirp has been demonstrated by using high-speed external electroabsorption modulators [Nod86], which is encouraging and shows that it is possible to develop an almost chirp-free light source extremely useful for light transmission systems.

Third, monolithically integrated light sources can reduce the coupling loss (or the insertion loss) significantly. Since the active layer of semiconductor lasers is very thin and has much higher refractive index than that of air, the output light beam diverges rapidly due to diffraction. By employing integrated modulator with wider guiding region and transition

waveguides between laser and modulator consisting of grating coupled waveguides [Zor73b] or tapered guides [Koc90], the modulated output beam can be coupled efficiently to the next device or optical fiber without large power losses. Thus, monolithic integration of optical modulators and lasers is indispensable to attain large bandwidth, small chirp, low insertion loss, and good reliability.

Thus far, the research on monolithic laser-modulator integration has been performed mostly on a pair of laser and electroabsorption modulator as intensity modulators. These devices are relatively simple to design and easy to fabricate. It is important to note, however, that the absorption modulators present potential problems such as heating, temperature and wavelength sensitivities, and photo-generated leakage current. Considering that one of the difficulties encountered in integrated optical circuits is the large amount of heat generated by diode lasers, it is not desirable to incorporate absorption modulators in the circuits because of their additional heat generation and temperature-sensitive operation. An alternative to the absorption modulator in laser-modulator integration schemes is the phase modulator. Since phase modulators are usually operated at photon energies far below the absorption edge, they do not exhibit excessive light absorption. In addition, phase modulation utilizes the change in the refractive index of waveguides similar to what occurs in couplers, switches, and interferometers [Don85a, Don85b, Tak89b]. Therefore, integration can easily be achieved with all and any of the optical devices to provide a variety of functions such as intensity modulation, beam splitting, multiplexing and demultiplexing.

In recent years, based on the promising characteristics, described above, intensive research are underway to develop small and efficient

waveguide phase modulators. Phase modulators with various structures developed so far have improved the phase shift efficiency, defined as the phase shift per unit length per unit bias voltage, achieving operation at bandwidths of a few or tens of GHz. Unfortunately, very few laser-phase modulator integration schemes have been reported and implemented [Kor88]. This is due to extremely complicated fabrication procedures needed to satisfy necessary conditions including wavelength detuning, small coupling loss, and good electrical isolation between laser and phase modulator. To date, this problem has been solved by multi-step epitaxial growth and complex etching techniques [Kaw87, Koc90, Suz87], which are presently immature and not quite suitable for integrated optical circuits with various optical devices.

1.2. Outline of The Present Work

The purpose of this work is to develop components of laser-phase modulator integrated devices with improved operating characteristics, and novel integration schemes, which can be implemented in particular, by simple fabrication techniques.

In a laser-modulator integrated device, laser usually works as a cw light source, and the light is modulated (intensity, phase, frequency, etc.) in the modulator section. Narrow linewidth for large modulation bandwidth and low threshold current for large scale integration are the most important properties in such diode lasers. In this work, first of all, we study extraordinarily broad linewidths in semiconductor diode lasers, and suggest practical methods for their reduction.

We choose phase modulation rather than the intensity modulation because of the several advantages mentioned in the previous section. Double-heterostructure (DH) semiconductor phase modulators recently developed [Alp87b, Fai87a, Fai87b, Men88] show a trade-off between the phase shift efficiency and junction capacitance, both of which determine the modulation speed, i.e., the modulation bandwidth. We develop a novel high-speed DH phase modulator by studying the physical phenomena (refractive index changes, absorption changes, optical and electric fields) induced in the phase modulator during operation.

Integration of lasers and modulators usually requires complicated growth and fabrication techniques, which is the main reason why the research in laser-modulator integrated devices has not progressed as rapidly as in other integrated devices in spite of the availability of well-developed individual components. We study the basic requirements for laser-modulator integration and develop a novel integration scheme for single quantum-well (SQW) lasers and multiple quantum-well (MQW) phase modulators, avoiding many of the complex techniques employed by other researchers [Kaw87b, Kor88, Suz87].

Following the introduction chapter, the contents of the dissertation included in chapters two through six, can be divided into four major categories described below. The results are summarized in chapter seven.

1.2.1. Device Application of Optical Properties

Semiconductor optical devices are based on the optical properties such as absorption and refractive index, and their changes depending on the bias condition. For example, laser utilizes the absorption change by

injecting carriers into the active layer, changing the absorption into gain. The light is efficiently guided by the refractive index difference between the active and cladding layers, causing lasing to occur at low thresholds. The refractive index also suffers a change due to the injected carriers, causing undesirable characteristics. The refractive index change is, however, invaluable for various other optical devices including the phase modulator whose operating principle is based on such changes. Therefore, a comprehension of the material optical properties and their changes is inevitable for designing and developing useful optical devices.

In chapter two, we review the theoretical and experimental optical properties in bulk GaAs/AlGaAs as well as their quantum-well structures. In chapter three, we discuss the refractive index change induced in a GaAs p-n junction under forward and reverse bias conditions. We present simple but useful equations, which are necessary for theoretical calculations in the following chapters. Theories and experiments accomplished in this work are based on GaAs/AlGaAs material system. It should be noted, however, that the theories and design concepts developed are applicable to other III-V and II-VI semiconductor material systems by using appropriate material parameters.

1.2.2. Reduction of Semiconductor Laser Linewidth

As carriers are injected into the active layer of a diode laser, the material property of the active layer changes from absorption to gain. The gain has a peak value at the lasing photon energy. However, the gain change, defined as the net absorption change (i.e., the sum of absorption change and gain) by carrier injection, has a peak value above the lasing

photon energy [Nas73, Hen81] as is shown in Fig.1.1. Disagreement between peak positions of the gain and the gain change is a distinct characteristic of diode lasers coming from band-to-band transitions of injected carriers, unlike other types of lasers represented by discrete energy-level transitions. The gain change then induces positive and negative refractive index changes across the peak gain change, which is well described by a Kramers-Kronig dispersion relationship [Hen81]. Note that the refractive index change is not zero at the lasing photon energy (i.e., the peak gain) as is shown in Fig.1.1.

Extraordinarily broad linewidths measured in diode lasers are a result of non-zero refractive index changes at the lasing photon energies as pointed out by Henry [Hen82]: Spontaneous emission not only causes an instantaneous optical intensity and phase change, but also brings an additional phase fluctuation coupled with the intensity change due to non-zero dispersion of the refractive index change at the peak gain. The additional phase change results in linewidth broadening by a factor of $(1 + \alpha^2)$. The α parameter is called the linewidth enhancement factor. It represents the coupling of intensity and phase physically, and the ratio of real and imaginary refractive index changes mathematically. Similar linewidth broadenings such as dynamic wavelength shift and dynamic spectral broadening, occurring in diode lasers modulated at high speeds, are also attributed to the intensity and phase coupling.

A large number of papers have been published on the α parameter and linewidth. Experimental values of α range from 0.5 to 8, depending on the laser structures and such factors as lateral waveguiding, active layer thickness, waveguide length, facet reflectivity, etc. A few theoretical analyses have been reported as a function of photon energy and injection

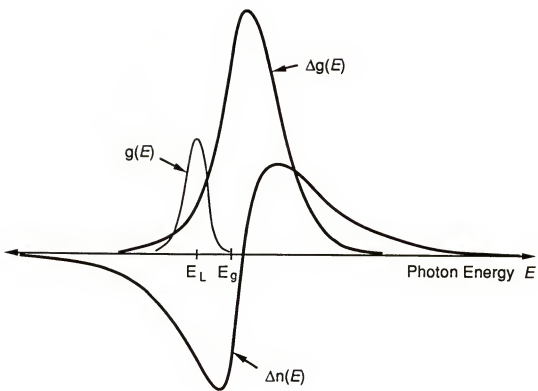


Figure 1.1 Gain $g(E)$, gain change $\Delta g(E)$, and refractive index change $\Delta n(E)$ in the active layer of diode lasers at threshold. Note that the gain is exaggerated to show a clear picture. E_L is the lasing photon energy and E_g is the bandgap energy.

current [Ara85, Oga84, Vah83]. Because of their parabolic-band assumptions, and hence unreal lasing wavelength evaluations, however, they could only explain the loss dependence of α qualitatively, and could not yet elucidate the wide distribution of α measured in various kinds of diode lasers. A quantitative analysis capable of clarifying the α variation was not available until the present analysis for the laser geometry dependence of the linewidth enhancement factor and linewidth in GaAs/AlGaAs laser diodes [Lee89a] as described in chapter four.

The analysis includes rigorous derivations of analytical expressions for the refractive index change and α . It is shown that the derived equations can reflect any loss arising in the cavity. The α and linewidth dependence on laser type, active layer thickness, and laser length is estimated by using these expressions and previously measured experimental absorption spectra. The results are discussed in detail and compared with reported experimental data. Based on the discussions, practical methods for the reduction of linewidth are suggested.

1.2.3. High-Speed DH Phase Modulators

Double-heterostructure waveguide is a very efficient structure for carrier injection, confinement, and light guiding. It is an indispensable part for semiconductor laser diodes to generate light. DH waveguide is also useful for semiconductor phase modulators because carriers can be injected or depleted efficiently, causing refractive index variations due to strong electric field which develops across the thin active layer with small voltage. Furthermore, it provides structural compatibility for integration of lasers and phase modulators.

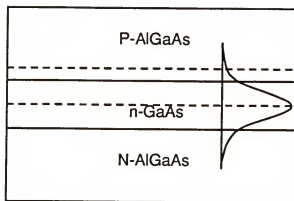
Phase modulators can be operated at either forward-biased or reverse-biased condition. However, most of the practical phase modulators have been operated under reverse bias because of their beneficial high-speed characteristics, even though forward-biased modulators provide much larger phase shift efficiencies. For example, carrier injection of the order of 10^{18} cm^{-3} causes refractive index changes of 0.02 - 0.03 [Hen81, Man83], an order of magnitude larger than those obtainable in reverse-biased devices. However, modulation speed is limited by carrier lifetime, resulting in modulation bandwidths of less than a GHz which are much slower than those of reverse-biased devices.

Earlier work on reversed-biased semiconductor phase modulators is based on the linear electro-optic (LEO) effect [Cam75, Don85b, Hou84, Rei72], leading to either long interaction lengths or high voltages because this effect is small in semiconductors. For example, the LEO effect in GaAs is approximately 6 times smaller than that in LiNbO_3 , mainly due to the LEO coefficient (r_{41}) in GaAs which is 25 times smaller than the r_{33} coefficient in LiNbO_3 . However, it has been shown recently [Alp87b, Fai87b] that, besides the LEO effect, there are three more effects encountered in reverse-biased DH phase modulators. These are the free carrier plasma (PL), bandgap shift (BS), and quadratic electro-optic (QEO) effects. The first two are associated with carrier depletion from the junction, and the latter and the LEO effect are caused by the electric field developed across the depletion region. Combined contributions of the four effects in GaAs/AlGaAs phase modulators becomes comparable to, or even larger than the LEO contribution in LiNbO_3 .

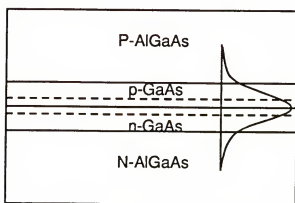
Recently, improved phase shift efficiencies of the order of 60 - 100 $^{\circ}\text{V}\cdot\text{mm}$ at $\lambda = 1.06 - 1.09 \mu\text{m}$, have been reported for P-n heterojunction

[Alp87b, Fai87a] and p-n homojunction [Men88] GaAs/AlGaAs DH phase modulators, shown in Figs.1.2a and 1.2b, respectively. These high efficiencies could be achieved by depleting a large number of free carriers from highly-doped (5×10^{17} - 2×10^{18} cm $^{-3}$) junctions and, hence, developing large electric fields in a very narrow depletion region, fully utilizing the higher-order (QEO and BS) effects as well as the LEO and PL effects. However, the narrow depletion regions not only cause large junction capacitances, resulting in lower speeds, but also increase propagation losses due to large electroabsorption. A P-i-N DH modulator with thick intrinsic layer (Fig.1.2c) [Fai87b], on the other hand, exhibits very low junction and dynamic capacitances, but also a relatively small phase shift efficiency as it utilizes primarily the LEO effect. The reduction of the intrinsic layer thickness will increase the electric field and, hence, the efficiency. However, a large portion of the overlap integral of optical and electric fields occurring in the AlGaAs cladding layers will result in smaller QEO and BS effects than those in GaAs. In addition, the main feature of low junction capacitance is significantly degraded by carrier spilling into the intrinsic GaAs layer from highly-doped AlGaAs cladding layers [Fai87a, Fai87b].

In this work, we propose and demonstrate a novel, high performance, P-p-i-n-N GaAs/AlGaAs DH waveguide phase modulator [Lee89b] with high phase shift efficiency as well as low junction capacitance, both of which determine the modulation speed. Fig.1.2d shows the P-p-i-n-N DH phase modulator, where the guiding region consists of p-i-n GaAs layers. High efficiency is achieved by utilizing the QEO and BS effects in GaAs rather than AlGaAs. At the same time, low junction capacitance and, hence, high speed is achieved by keeping the depletion

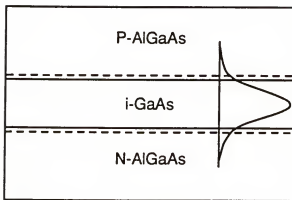


(a)

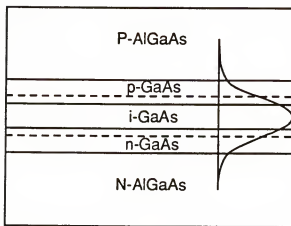


(b)

Figure 1.2 Various structures of high-efficiency GaAs/AlGaAs DH waveguide phase modulators
(a) P-n heterojunction DH phase modulator
(b) p-n homojunction DH phase modulator



(c)



(d)

Figure 1.2 Continued

(c) P-i-N DH phase modulator
(d) P-p-i-n-n DH phase modulator

region within the p-i-n guiding layers. Phase shift efficiencies of 82 and 37.5 %/V·mm at $\lambda = 1.06$ and $1.3 \mu\text{m}$, respectively, were obtained for the TE_0 mode. These correspond to highest values for P-n heterojunction and p-n homojunction GaAs/AlGaAs DH phase modulators.

The phase efficiency and junction capacitance depend on the intrinsic layer thickness and carrier concentrations in the p- and n-GaAs layers. Choice of these parameters offers a number of opportunities for the design of DH phase modulators. For example, as we decrease the intrinsic layer thickness and increase the carrier concentration, the P-p-i-n-N phase modulator essentially become a p-n homojunction DH phase modulator with increasing phase shift efficiency and junction capacitance. Decrease in carrier concentration down to an intrinsic level results in a P-i-N DH modulator. Therefore, a detailed analysis for the P-p-i-n-N phase modulator [Lee90] not only provides performance comparisons of the three types of modulators but also facilitates optimization of DH phase modulators in terms of high-speed operation.

In chapter five, we present a detailed analysis of P-p-i-n-N GaAs/AlGaAs DH phase modulators, use it to optimize DH phase modulators and, by comparisons with experimental results, extract physical coefficients unknown to date. Device fabrication and phase shift measurement are described. Excellent agreement between experimental and theoretical results, which includes phase shift dependences on wavelength, carrier concentration, and intrinsic layer thickness, is obtained. Based on the present and previously reported results, we suggest design criteria of double-heterostructure semiconductor phase modulators for high-speed modulation.

1.2.4. Integration of Laser and Phase Modulator

The transmission of information at Gbit/s rate in dispersive medium, in general, imposes limitations on the performance of directly modulated semiconductor lasers and has led to the search of external modulation of laser light. The reduction of the chirp has also been demonstrated for high-speed external modulators [Nod86, Dec90]. Thus, monolithic integration of an optical modulator with a laser is recognized to be imperative for high-speed applications. Fig.1.3 shows a schematic diagram of a typical laser-modulator integrated device, where laser is operated at a constant injection level I_L , emitting constant power, and modulator is driven with modulation bias voltage V_m . For the purpose of efficient overlap of optical and modulating fields, modulator is usually designed to have thicker active layer than the laser. In addition, modulation bias voltage has to be isolated from laser, not affecting lasing condition. Therefore, the intermediate region between the two components has to provide efficient optical coupling and good electrical isolation.

It is, of course, not easy to meet the above conditions at the same time. The common difficulty confronted by integrated optics designers is that the bandgaps required for various semiconductor optical components are usually different. For example, to obtain large on-off ratio, exciton resonance peaks of MQW absorption modulators have to be tuned to the lasing photon energy determined by the bandgap of the laser [Woo88]. On the other hand, the exciton resonance peaks of MQW phase modulators have to be at much higher photon energies (at least 50 ~ 70 meV) than the lasing photon energy, to avoid serious absorption loss in the modulator

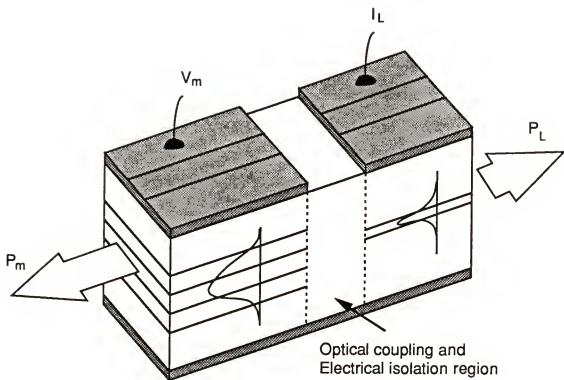


Figure 1.3 Schematic diagram of typical laser-modulator integrated device. V_m is the modulation voltage and I_L is the injection current.

section [Wei87, Zuc88a]. This is called the wavelength detuning between the integrated optical components. Recently, several monolithic integration schemes of DFB lasers and electroabsorption modulators [Kaw87, Sak86, Suz87] showing gigahertz operations with low chirps, have been reported. However, most of these devices had to utilize multi-step growth techniques such as three-step vapor phase epitaxy (VPE) or liquid phase epitaxy (LPE)/MBE hybrid growth, to satisfy the wavelength detuning condition, which complicates fabrication procedures.

Monolithic integration of MQW laser and MQW electroabsorption modulator utilizing room-temperature exciton features has also been reported for single-step grown structures [Tar86]. However, absorption losses were significant in the modulators and the loss changes caused by the modulation bias voltages affected laser operation, causing threshold current instability and wavelength shift. Integrated devices using the same schemes could generate short optical pulses (i.e., Q-switching) rather than modulate light efficiently [Ara86a]. Furthermore, these devices are not suitable for future integration, as they would still need regrown waveguides for low-loss interconnects of the guided light.

A low-loss waveguide phase modulator is, therefore, more desirable than an electroabsorption modulator as an integrated partner for the laser. Extremely large phase shift efficiencies of 520 °/V·mm have been reported for GaAs/AlGaAs MQW waveguide phase modulators at wavelengths as far as 400 Å below excitonic resonance [Zuc88a]. π -phase shifts were possible with waveguide lengths of the order of 100 ~ 200 μm for unit applied voltage, which correspond to tens of GHz operation. However, a recent report [Kor88] of MQW laser-phase modulator integration also demanded both a regrowth process and precise etching techniques.

In chapter six, we propose a novel scheme for monolithic integration of GaAs/AlGaAs SQW lasers and MQW phase modulators, utilizing angled reactive ion etching (ARIE) [Tak89a] and impurity induced disordering (IID) [Tho88] on as-grown MQW samples. The proposed structure contains SQW and MQW regions in the active layer, where the well thickness of SQW should be larger than that of MQW's to satisfy the wavelength detuning condition. For the purposes of determination of suitable well thicknesses, and investigation of electroabsorption near exciton resonance, transverse MQW absorption modulators with different well thicknesses are fabricated and characterized. Before integration, SQW lasers are fabricated and characterized. Results show that desirable characteristics such as low threshold current density in the SQW lasers can easily be achieved. The MQW phase modulators employing thin (50 Å) QW's are being characterized, and the IID research necessary for integration is currently being carried out at the Photonics Research Laboratory by using both diffusion and implantation of impurities. Although integrated devices are yet to be realized, we discuss advantages of thin MQW phase modulators, possible structures for integration and other considerations necessary for the integration, including ARIE, IID, coupling efficiency, and electrical isolation.

CHAPTER TWO OPTICAL PROPERTIES OF GaAs BULK AND QUANTUM WELL

2.1. Introduction

There was a great deal of activity in optical experiments in GaAs during 50's to 60's as the supply of single crystals became available. The main purpose of the experiments was to investigate band structures by means of band-to-band transitions of carriers absorbing light. These days, the changes of absorption and refractive index near the bandgap have attracted great interest for opto-electronic applications since these effects form the corner-stone of most of the GaAs/AlGaAs optical devices.

In this chapter, we look into variations of the absorption and refractive index with external perturbations, which indicate means to alter the optical properties from those in intrinsic GaAs, including doping concentration, AlAs mole fraction, and electric field. We describe the variations in GaAs bulk in sections 2.2 and 2.3. Recent advances in semiconductor growth techniques made it possible to fabricate complex quantum-well (QW) structures with extremely useful linear and nonlinear optical properties, quite different from the bulk material. Among them, the quantum-confined Stark effect (QCSE) [Mil84], that is, large electroabsorption featured by excitonic resonances at room-temperature, is of great interest to us due to its versatile applications in modulators, self-

electrooptic effect devices (SEED's), and polarization-sensitive devices. It is discussed in section 2.4.

2.2. Absorption in Bulk GaAs

It is convenient to divide the absorption spectrum of GaAs into three distinct regions; i) fundamental absorption ($E = 1.3 \sim 2$ eV), ii) infrared absorption ($E < 1.3$ eV), and iii) high-energy absorption ($E > 2$ eV). The most interesting optical phenomena of semiconductors are involved in the fundamental absorption, which consists of allowed-direct band-to-band transitions, transitions between band tails, and excitonic transitions. Fig.2.1 shows a typical fundamental absorption spectrum [Mo61].

Assuming parabolic conduction and valence bands, the absorption coefficient due to the direct transitions is given by [Mos61, Ste64]

$$A(E) = A_1 (E - E_g)^{1/2} \quad (2.1)$$

where E is the photon energy and E_g is the bandgap energy. A_1 is a constant determined by the effective masses of the carriers and transition probability. The absorption coefficient complying with the above equation is shown in Fig.2.1 as the dotted line. According to Eq.(2.1), there is no absorption below E_g , i.e., within the bandgap. However, experimental results show gradual decrease of absorption as photon energy decreases from E_g to lower energies. This broadening reduces the utility of GaAs absorption modulators for large on-off ratio.

Ionized impurities exert coulombic forces on conduction electrons and valence holes, disturbing band edges to form exponential tails of states

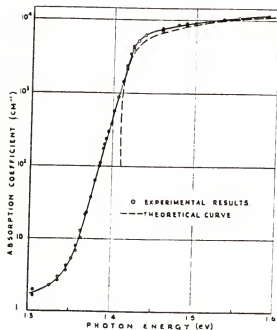


Figure 2.1 Absorption spectrum near the bandgap in gallium arsenide [Mos61].

into the bandgap. With the absorption of photons having energies less than E_g , electrons in the valence band tails of states move up to conduction band in n-type GaAs, or electrons in valence band move up to the conduction band tails of states in p-type GaAs. Hence, the absorption coefficient just below the bandgap will be exponential [Hwa69, Ste64];

$$A(E) = A_2 \exp\left(\frac{E-E_g}{E_u}\right), \quad E_a < E < E_g \quad (2.2)$$

where E_u is the Urbach coefficient, representing the slope of the exponential absorption edge, and E_a is the energy below which the infrared absorption becomes dominant. The exponential absorption edge is a function of carrier concentration and temperature [Hil64, Hwa69, Kud62].

The infrared absorption refers to complex transitions occurring below the absorption edge, of which three dominant processes are free carrier, impurity level-to-band, and intersubband absorptions. Fig.2.2 shows the infrared absorptions of n-GaAs at room-temperature [Sp59]. The fundamental absorption edge is seen at wavelengths less than 1 μm . Free carrier absorption is dominant at long wavelengths, greater than 4 μm . It is caused by scattering with acoustic phonons ($\sim \lambda^{1.5}$), optical phonons ($\sim \lambda^{2.5}$) and ionized impurities ($\sim \lambda^3$ or $\lambda^{3.5}$). Thus, free carrier absorption should be a weighted sum of the three processes [Pan71], but frequently used in optical device analyses is a semi-classical formula;

$$A_f(\lambda) = \frac{N q^3 \lambda^2}{4 \pi^2 n m^* \mu \epsilon_0 c^3} \quad (2.3)$$

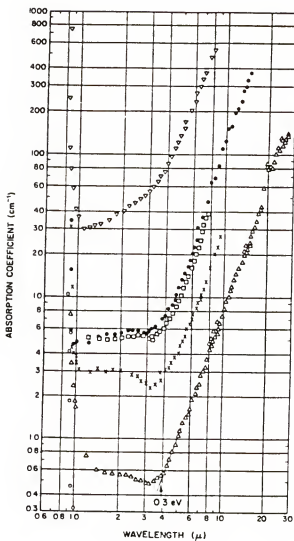


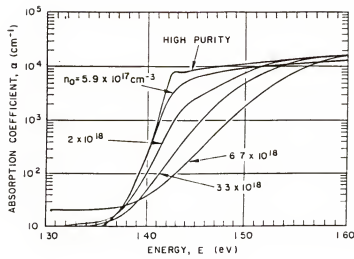
Figure 2.2 Infrared absorption spectra of n-GaAs at room temperature for six samples of different doping, the electron concentration increasing from $1.3 \times 10^{17} \text{ cm}^{-3}$ for the lowest curve to $5.4 \times 10^{18} \text{ cm}^{-3}$ for the upper curve [Sp59].

where N is the carrier concentration, n is the refractive index, m^* is the effective mass, μ is the mobility, and ϵ_0 is the free space permittivity. From Eq.(2.3), free carrier absorption is found to be proportional to $\sim \lambda^3$ since n is approximately proportional to $1/\lambda$, which agrees well with the experimental results in Fig.2.2.

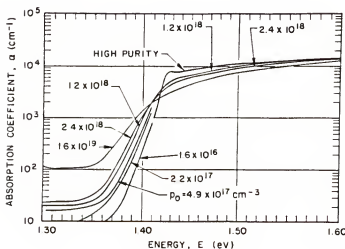
Relatively flat absorption in the middle part of the spectra ($1 < \lambda < 4 \mu\text{m}$) is a combination of free carrier absorption and additional absorption composed of impurity and intersubband absorptions. Impurity absorption due to transitions between impurity levels and bands is dominant at lower energies of the exponential absorption edge, smoothing out exponential decrease of absorption near $\lambda = 1 \mu\text{m}$. Intersubband absorption occurs dominantly in the range of $2 \sim 4 \mu\text{m}$. In n-GaAs, it is mainly due to transitions from Γ -band to X-band, and decreases monotonically as photon energy decreases. However, p-GaAs shows more complicated intersubband absorption [Bra62]. The valence band of most semiconductors consists of three subbands and, hence, three types of direct transitions are allowed; (a) from light-hole to heavy-hole band, (b) from split-off to heavy-hole band, and (c) from split-off to light-hole band. Since direct transitions are possible between them, intersubband absorption in p-GaAs is much stronger than that in n-GaAs.

Higher-energy absorption ($E > 2 \text{ eV}$) is characterized by transitions between conduction and split-off valence bands, L-band direct transitions, and X-band direct transitions. Even though this region is beyond our interest for device applications, it should be noted that the higher-energy absorption plays an important role in determining the refractive index.

The carrier concentration dependence of absorption edge is shown in Figs.2.3a and 2.3b for n- and p-GaAs at 297 °K, respectively [Cas75]. For n-



(a)



(b)

Figure 2.3 Absorption spectra near the bandgap for (a) n-GaAs and (b) p-GaAs as a function of carrier concentration [Cas75].

GaAs, the absorption edge moves to higher energies with an increase of carrier concentration. The exponential absorption edge is broadened at the same time. The absorption edge shift is called the Burstein shift [Bur54] (or the band-filling effect) due to the filling of conduction band by free electrons. The increase of ionized impurities induces stronger disturbances on band edges, broadening the exponential absorption edge [Cas75, Hil64, Hwa69]. The infrared absorption is seen below 1.35 eV, increasing with an increase of carrier concentration as mentioned above.

In p-GaAs, the absorption edge shifts in a different way from n-type GaAs. As the carrier concentration increases, the band filling of carriers and the rigid contraction of bandgap (i.e., the bandgap shrinkage effect) [Cas76] occur simultaneously, regardless of carrier type. However, as a result of much larger number of states at valence band edge, the band-filling rate by holes is much slower than that by electrons, and is comparable to the bandgap contraction rate. The absorption edge, therefore, looks like moving to lower energies as is shown in Fig.2.3b. Note that the infrared absorption is also larger in p-GaAs than n-GaAs. These are the main reasons why optical devices, except lasers, employ n- or intrinsic GaAs active layer.

In the presence of an electric field, the band edges are tilted. As a result, the effective thickness of the energy barrier for the valence electrons to overcome and appear in the conduction band is reduced. Barrier height is also reduced by photon absorption, which is equivalent to additional reduction of barrier thickness. This means that there is a greater probability of finding an electron inside the bandgap, or a greater transition probability at lower energies than the bandgap. Therefore, absorption increases below the bandgap with applied electric field (Fig.2.4). This is

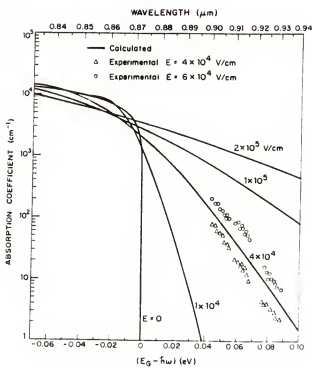


Figure 2.4 Experimental and theoretical electric field dependence of absorption coefficient (the Franz-Keldysh effect) near the fundamental absorption edge in GaAs [Sti76].

called the Franz-Keldysh effect [Cal63, Tha63], and is represented by the following equation:

$$A(E, F) = \sum_j A_j F^{1/3} \left[\left(\frac{dAi(z)}{dz} \right)_{\beta_j}^2 - \beta_j |Ai(\beta_j)|^2 \right] \quad (2.4)$$

where $A_j = \frac{7.65 \times 10^5}{nE} \left(\frac{2m_j^*}{m} \right)^{4/3}$

$$\beta_j = 1.1 \times 10^5 \left(\frac{2m_j^*}{m} \right)^{1/3} (E_g - E) F^{-2/3}$$

F is the electric field in V/cm. Ai is the Airy function. m_j^* is the reduced effective mass. E_g and E are in eV. The sum is over the light- and heavy-hole valence bands.

Interest in electroabsorption due to the Franz-Keldysh effect has been significant because of the application to intensity modulation [Sti76]. However, considerable broadening, not actual shift, of the absorption edge reduces its usefulness. Instead, there has been an increased interest in utilizing the refractive index change by the electroabsorption as well as the band-filling effect for phase modulation, which will be discussed in detail in chapter five.

Very few absorption data for AlGaAs have been reported. It is difficult to investigate the absorption properties of AlGaAs compared to GaAs. Nevertheless, it is possible to discuss absorption spectrum of AlGaAs in a qualitative manner by comparing physical parameters of AlGaAs and GaAs such as the bandgap energy and effective masses. The fundamental absorption edge of pure GaAs can be used for pure AlGaAs, by simply shifting it to higher energies by the bandgap difference.

Intentionally undoped AlGaAs has carrier concentrations of the order of $10^{15} - 10^{16} \text{ cm}^{-3}$, and the slope of the exponential absorption edge, i.e., the inverse of the Urbach coefficient in Eq.(2.2) is about $130 - 140 \text{ eV}^{-1}$. The slope in pure GaAs with carrier concentrations of less than $1 \times 10^{13} \text{ cm}^{-3}$, is $140 - 150 \text{ eV}^{-1}$. This indicates that the coulombic perturbation between ionized impurities and free carriers is much smaller for AlGaAs than GaAs, due to the larger bandgap of AlGaAs. In addition, the absorption coefficient of AlGaAs should be larger at a given energy near the bandgap than that of GaAs since the density of states at conduction and valence band minima are larger for AlGaAs than GaAs, due to heavier effective masses.

The band-filling effect is a dominant effect in n-GaAs. However, it has been reported that, even in n-AlGaAs with a small amount of AlAs mole fraction (~ 8 percent) [Hen80], the bandgap shrinkage effect becomes comparable to the band-filling effect as a result of increased effective masses. The absorption and refractive index change in AlGaAs with the increase of carrier concentration, thus, will be small due to the two opposite effects, discussed in detail in chapter four.

2.3. Refractive Index of Bulk GaAs

Because of their importance in development of optoelectronic devices, refractive indices of GaAs and $\text{Al}_x\text{Ga}_{1-x}\text{As}$ have been thoroughly investigated experimentally and theoretically. In this section, we review experimental data frequently referred to in various papers, and introduce analytical models for the refractive index of these materials. Finally, empirical formulae are presented for calculation of the refractive index of ternary semiconductors.

Even though a large number of measurements of the refractive index of GaAs have been reported at particular photon energies, more accurate and organized data had not been available until Marple [Mar64] reported refractive indices of GaAs at photon energies from 0.7 eV up to the absorption limit set by the bandgap. The prism refraction method was used by preparing GaAs prisms from "boat-grown" single crystals with doping concentrations of $\sim 6 \times 10^{16} \text{ cm}^{-3}$. Fern and Onton [Fer71] also reported refractive indices of AlAs ($x=1$) measured at photon energies of 0.5 - 2.2 eV. These data at both ends of AlAs mole fraction have been precious informations for justifying experimental results and completing theoretical models of $\text{Al}_x\text{Ga}_{1-x}\text{As}$ refractive indices.

The most accurate and systematic measurements were made at room temperature by Casey et al. [Cas74], using the double-beam reflectance method. Samples used were unintentionally doped n-type. Possible errors in the measured refractive index values were within ± 0.005 , and mainly came from the assignment of AlAs composition. The refractive index dependence on AlAs mole fraction is shown in Fig.2.5 as a function of photon energy. These experimental values of the refractive index of GaAs show a good agreement with the values obtained on GaAs prisms by Marple, if a small change of refractive index due to the carrier concentration is taken into account. Furthermore, it was possible in the double-beam reflection method to measure the refractive index at photon energies near and above the bandgap, which was hard to obtain in the prism refraction method.

The carrier concentration dependence of refractive index in n- and p-GaAs was reported by Sell et al. [Sel74], using the double-beam reflectance. Fig.2.6a shows the results for n-GaAs. As the carrier concentration

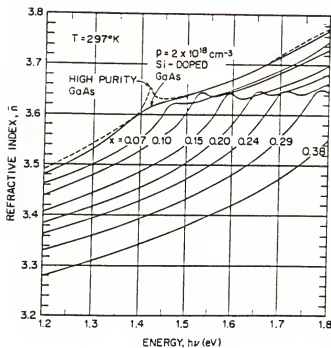
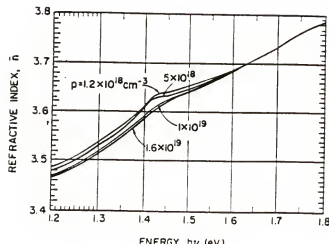
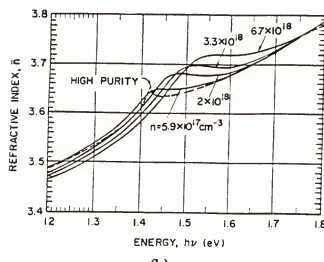


Figure 2.5 Refractive index dispersion for $\text{Al}_x\text{Ga}_{1-x}\text{As}$. For purposes of comparison, the high-purity GaAs and Si-doped GaAs is also given [Cas74].



(a)



(b)

Figure 2.6 Carrier concentration dependence of refractive index near the bandgap for (a) n-GaAs and (b) p-GaAs [Sel74].

increases, the refractive index below the bandgap decreases, and the peak near the bandgap shifts to higher energies. This behavior is expected from the Burstein shift of absorption edge with increasing electron concentration. For the interesting range of electron concentration in several useful optical devices ($\leq 1 \times 10^{18} \text{ cm}^{-3}$), unfortunately, the change of refractive index below the bandgap was found to be smaller than uncertainties of ± 0.005 inherent in the measurements. This is confirmed by recent phase modulation results utilizing the band-filling effect which estimate refractive index changes of 0.002 - 0.003 below the bandgap. Note that the peak near the bandgap broadens with increasing carrier concentration, which represents smaller slopes of the exponential absorption edge with large concentrations as shown in Fig.2.3. The changes of refractive index for p-GaAs samples (Fig.2.6b) are similar to n-GaAs, but much smaller. This is due to the smaller shift of the absorption edge by the band-filling and bandgap shrinkage effects.

A large number of attempts to calculate the refractive index of GaAs and $\text{Al}_x\text{Ga}_{1-x}\text{As}$ have been made, theoretically and semi-empirically. Stern [Ste64] did pioneering theoretical work on the refractive indices of semiconductors. Absorption of many semiconductors at energies above the bandgap can be characterized by one or more sharp peaks in the imaginary part of the dielectric constant, ϵ_2 . Therefore, using a Kramers-Kronig dispersion relation, Stern derived a useful equation for the refractive index in semiconductors:

$$n(E) = \left[1 + k^2(E) + \sum_j \frac{G_j}{E_j^2 - E^2} \right]^{1/2} \quad (2.5)$$

where k is the extinction coefficient (the imaginary part of the refractive index), and G_j and E_j are the strength and position of the j th peak in the imaginary part of the dielectric constant, respectively. In addition, Stern included the effect of the absorption edge on the refractive index via the Kramers-Kronig relation:

$$\Delta n(E) = \frac{hc}{2\pi^2} \int_0^{E_s} \frac{A(E)}{E^2 - E^2} dE \quad (2.6)$$

where h is the Planck's constant, c is the speed of light, and E_s is an arbitrary energy separating the absorption edge region from the high-energy absorption region. E_s is well above the absorption edge, and also lies below the energy E_j of the peaks. The utility of Eq.(2.6) is noteworthy: For example, the refractive index change due to carrier injection in laser diodes, carrier depletion or applied electric field in phase modulators can be estimated by using this equation. We have also used this equation for theoretical calculations in our work. Stern's results, calculated from Eqs.(2.5) and (2.6) using Sturge's absorption data [Stu62], are shown in Fig.2.7 along with Marple's prism data [Mar64].

The spectral range of interest for GaAs optoelectronic devices is usually between energies far above the free carrier plasma frequencies and below the bandgap. Therefore, several authors reported simple and useful equations for the refractive index calculation in this spectral range. Blakemore [Bla82] presented a very simple first-order Sellmeier equation for GaAs, using the high-frequency dielectric constant $\epsilon_{\infty}(=n_{\infty}^2)$ measured at frequencies well above the longitudinal phonon frequency (32 - 50 meV) but below the absorption edge. Earlier, Boyd [Boy72] suggested a similar

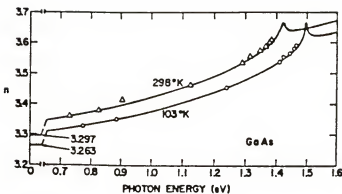


Figure 2.7 Refractive index dispersion calculated by Eqs.(2.5) and (2.6) for relatively pure GaAs [Ste64]. Open triangles are taken from the prism measurements of Marples [Mar64]. The indicated values at zero photon energy are the long wavelength limits of the index at 103 °K and 298 °K in the absence of the lattice vibration and free-carrier contributions.

Sellmeier equation for the analysis of GaAs thin-film waveguides, which can also evaluate the refractive index of $\text{Al}_x\text{Ga}_{1-x}\text{As}$. However, Boyd's calculation was less accurate than Blakemore's for GaAs, and showed significant discrepancy for AlAs from experimental data of Fern and Onton [Fer71]. Recently, Adachi [Ada85] reported a universal expression for zinc-blende semiconductors below the bandgap. The expression seems to be more physical than others and includes band structure parameters such as the first critical-point energy (or the bandgap energy) and spin-orbit splitting energy (or the split-off bandgap energy). However, it has a complicated form and also gives inaccurate values near the bandgap.

An interesting semi-empirical method for calculating the refractive index of $\text{Al}_x\text{Ga}_{1-x}\text{As}$ below the bandgap was presented by Afromowitz [Afr74]. The calculation of the refractive index of semiconductors rests largely on a single-effective-oscillator, in which one approximates the spectrum of imaginary dielectric constant $\epsilon_2(E)$ with a delta function of strength $\pi E_d/2$ at an energy E_0 . Below the bandgap, we can express Eq.(2.5) for the single-effective-oscillator, as follows;

$$n^2(E) - 1 = \frac{E_0 E_d}{E_0^2 - E^2} \quad (2.7)$$

However, refractive indices calculated by Eq.(2.7) differ substantially from experimental data at energies approaching the bandgap. This is due to the effect of the low-energy side of the ϵ_2 spectrum, i.e., the absorption edge.

Instead of a delta function, Afromowitz employed an empirical form describing well the low-energy side of the ϵ_2 spectrum. Taking a power series expansion of the Kramers-Kronig dispersion relation and using empirical ϵ_2 spectra, Eq.(2.7) was modified to the following equation,

$$n^2(E) - 1 = \frac{E_d}{E_0} \left[1 + \left(\frac{E}{E_0} \right)^2 + \frac{E^4}{2E_0^2(E_0^2 - E_\Gamma^2)} \ln \left(\frac{2E_0^2 - E_\Gamma^2 - E^2}{E_\Gamma^2 - E^2} \right) \right] \quad (2.8)$$

$$\text{where } E_0 = 3.65 + 0.871x + 0.179x^2 \quad (2.9)$$

$$E_d = 36.1 - 2.45x$$

$$E_\Gamma = 1.424 + 1.266x + 0.26x^2$$

E_Γ is the bandgap energy and x is the AlAs mole fraction. Refractive indices calculated by the above equations are shown in Fig.2.8 as open circles for $x=0.0$ to 0.38 . They reproduce refractive indices measured by Casey et al. [Cas74] (solid lines) extremely well up to the bandgap. Looking at Eq.(2.8) closely, we observe that the first two terms correspond to the approximation of Eq.(2.7) when $(E/E_0) \ll 1$. Thus, the last term is found responsible for the excellent agreement of refractive indices near the bandgap. On the other hand, the last term has a negligible effect far from the bandgap. This means that the first two terms, i.e., Eq.(2.7), are sufficient to calculate the refractive index at energies far from the bandgap. The boundary for validity of Eq.(2.7) is given to be $(E/E_0) \sim 0.1$ (i.e., $\lambda = 1.05 \mu\text{m}$).

2.4. Quantum-Confined Stark Effect

In the last two decades, development of new methods for semiconductor epitaxial growth has been very successful. Especially, growth techniques such as MBE and MOCVD can produce high-purity heterojunctions with atomically abrupt and smooth interfaces by manipulating growth rate as low as 1 \AA/sec . In addition, such slow growth

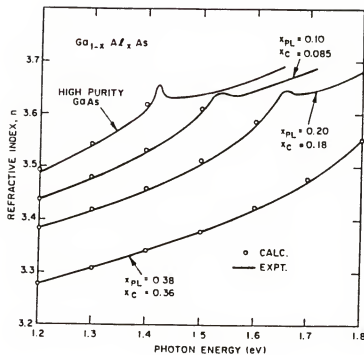


Figure 2.8 Comparison of refractive index data and calculation results of Afrumowitz [Afr74] for $\text{Al}_x\text{Ga}_{1-x}\text{As}$. Solid curves represent data measured by Casey et al. [Cas74], and x_{PL} denotes the experimentally determined alloy composition. Circles denote calculated values.

rates permit the fabrication of useful stacks of ultrathin layers called quantum-well (QW) or superlattice structures, which exhibit novel optical and electronic properties not observable in the bulk material. In this section, we discuss the optical properties of QW structures and describe some of the recent applications to QW modulators.

In QW structures, where a low bandgap, quantum-well layer is sandwiched between two barrier layers of a high bandgap material and the well thickness is comparable to the Bohr radius in the bulk material (~ order of 100 Å), free carrier behavior in the low-bandgap layer (quantum well) is radically modified due to the confinement in the direction perpendicular to the layers. The motion of electrons and holes is now subject to two-dimensional behavior in the plane of the layers. This restriction of carrier motion causes a set of discrete energy levels, as shown schematically in Fig.2.9a. Therefore, the conduction and valence bands become sets of two-dimensional sub-bands with step-like densities of states [Ara86b]. This increases the number of states at the discrete energy levels, which in turn enhances the optical transitions at the absorption edge, actually sharpening the absorption edge. Hence the absorption spectra of QW structures are significantly different from those of bulk materials. QW structures have been used for improving the performance of QW modulators and for developing very low threshold QW lasers. Here, we need to be precise about the definitions of QW structures since bandgap discontinuities are often encountered at the heterojunctions (Fig.2.9a). If the bandgap discontinuities are large enough and the barriers are wide enough, then there is little interaction between the wavefunctions of carriers in the adjacent low bandgap layers. The carriers confined in each QW layer behave almost independently and a collection of such QW,s are

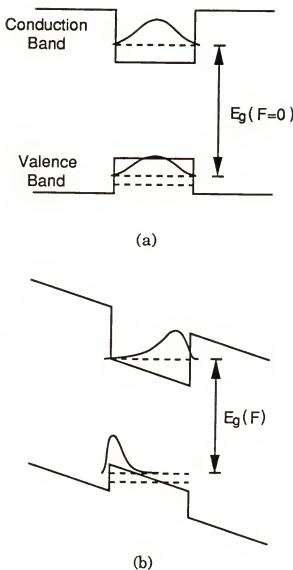


Figure 2.9 Schematic band diagram of a quantum well and distributions of carrier wavefunction (a) without, and (b) with an applied electric field perpendicular to the quantum well layers. With the electric field, the bandgap is reduced effectively and the wavefunctions of electron and hole are pulled out to opposite walls of the quantum well, which prevent the carriers from tunnelling through barrier layers.

called QW structures. If the energy of a state is comparable to the bandgap discontinuities or when the barriers become narrow, the interaction between adjacent layers becomes important. The wavefunction of carriers is extended perpendicularly to the layers, so the behavior of the carriers is modified by the periodic long-range modulation superimposed upon the crystalline potential. Such structures are called superlattices.

The utility of QW structures on optical devices is based on excitonic absorptions resolvable at room temperature. When a high purity semiconductor absorbs a photon, the electron jumps to the conduction band and interacts with the hole left in the valence band. The electron and hole can form a hydrogen-like bound-state called exciton. This interaction produces a set of discrete energy states and very strong absorption lines just below the bottom of the conduction band. Because the binding energy of the excitons is normally very small, excitons are easily dissociated by thermal phonons and usually observed only at low temperatures in bulk semiconductors [Stu62].

In a QW structure with layer thicknesses smaller than the Bohr radius, the exciton wavefunction is modified to accommodate the narrowing of the well and the low bandgap: The electron and the hole are forced to orbit closer to each other, i.e., the exciton wavefunction flattens and shrinks. Moreover, the binding energy increases by a factor of two or three. This added stability makes the excitonic resonances observable at room temperature, as demonstrated clearly by the absorption spectrum shown in Fig.2.10 [Mil85]. This spectrum was measured at room temperature in a high-quality GaAs/AlGaAs MQW structure. The peaks are so apparent in QW structures not only because of the increased exciton binding energy but also because the confinement strongly enhances the

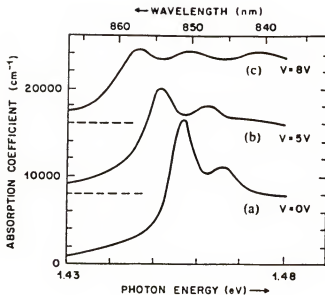


Figure 2.10 Room temperature absorption spectra for a MQW sample at various applied electric fields perpendicular to the quantum well layers; (a) 1×10^4 V/cm, (b) 5×10^4 V/cm, and (c) 7×10^4 V/cm. The zeros of curves (b) and (c) are displaced for clarity as shown by the dashed lines [Mil85].

contrast with the continuum. The reduced symmetry of QW structures, however, produces two valence bands, i.e., heavy-hole and light-hole bands, and hence the presence of two exciton peaks seen at the onset of the first transition.

Excitons in QW materials are sensitive to electrostatic perturbations. Because the carrier wavefunctions extend to about 100 \AA , and because the confinement or binding energies are only $10 \sim 100 \text{ meV}$, moderate electric fields of order $10 \text{ mV per } 100 \text{ \AA}$, or 10^4 V/cm , cause significant perturbations. When an electric field is applied to a three-dimensional exciton, it induces a Stark effect analogous to that seen in atoms. There is a small shift in energy levels that is quickly masked because in the bulk material the energy levels are broadened by the exciton's ionization under the influence of the electric field. However, in QW structures, a large shift of the absorption edge can be observed even under a large electric field, still retaining the clear exciton resonances. The radical change of the optical absorption spectrum is due to the quantum confinement of carriers in one dimensional potential wells, thus, this phenomenon is defined as quantum-confined Stark Effect (QCSE) [Mil84].

Here, we need to distinguish two different cases. It is well known that distinct effects are observed for fields both parallel and perpendicular to QW layers. In both cases, large changes in the absorption spectra near the exciton peaks are observed primarily due to excitonic resonances. In the parallel-field case, the excitons broaden with field, disappearing at fields of 10^4 V/cm . This behavior is qualitatively similar to that seen in the bulk material. In the perpendicular-field case, however, as can be seen in Fig.2.10, the exciton peaks shift to lower energies by up to 2.5 times the zero-field binding energy with the excitons remaining resolved at fields of up to

10^5 V/cm. This behavior is qualitatively different from that of the corresponding bulk material.

The mechanism of QCSE with applied electric field perpendicular to the QW layers is explained qualitatively as follows. Electric field perpendicular to the QW layers pull the electrons and holes toward opposite sides of the layers, resulting in an overall net reduction in energy of an electron-hole pair (Fig.2.9b) and a corresponding Stark shift in the exciton absorption. Also the walls of the QW impede the electron and hole from tunneling out of the well due to rapid field ionization. Furthermore, because the well is narrow ($\sim 100 \text{ \AA}$) compared to three dimensional exciton size ($\sim 300 \text{ \AA}$), the electron-hole interaction is still strong although weakened by the separation of electron and hole. Thus, exciton resonances can persist at much higher fields than would be possible in the absence of this confinement.

Fig.2.10 shows the electric field dependence of the electroabsorption in MQW structure with light propagating perpendicular to the well layers. In this case, light can propagate with its electric field vector only parallel to the plane of the well layers. However, if light made to propagate along the plane of the layers, it can propagate with its electric field vector either in the plane of the layers or perpendicular to the plane. The latter polarization, shows different selection rules for electron-hole transition.

Weiner et al. [Wei85] performed experiments using a p-i-n- leaky waveguide MQW structure which had two QW's and made only the fundamental mode propagate. Fig.2.11 shows the absorption spectra at different electric fields for light polarization parallel and perpendicular to the plane of the layers. For light polarized parallel to the plane both the heavy-hole (hh) and light-hole (lh) excitons appear as expected in the same

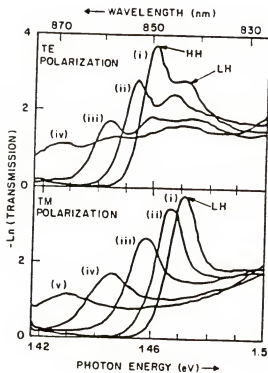


Figure 2.11 Absorption spectra of a quantum-well waveguide with applied electric fields perpendicular to the quantum well layers: (a) Incident polarization parallel to the plane of the layers (TE polarization) for fields of (i) 1.6×10^4 , (ii) 1×10^5 , (iii) 1.3×10^5 , and (iv) 1.8×10^5 V/cm. (b) Incident polarization perpendicular to plane of the layers (TM polarization) for fields of (i) 1.6×10^4 , (ii) 1×10^5 , (iii) 1.4×10^5 , (iv) 1.8×10^5 , and (v) 2.2×10^5 V/cm [Wei85].

polarization in Fig.2.10. For light polarized perpendicular to the plane, the hh exciton absorption effectively vanishes and its strength is transferred to the single remaining lh peak at higher photon energy. Consequently, the absorption without field is strongly dichroic for light propagating in the planes of the layers. The spectra were taken for even higher fields than those in the previous MQW structure, yet the exciton peaks remain well resolved. The absorption edge remains sharp and the dichroism persists, which make MQW structures extremely useful as absorption modulators and polarization-sensitive optical devices. This waveguide device was operated as a modulator by tuning the laser to a fixed incident photon energy below the zero-field absorption edge. Modulation depths, defined as the ratio of the maximum to minimum transmission of light, of 10.2 and 9.2 dB were obtained for light polarized perpendicular and parallel to the plane of the layers, respectively. In comparison, the conventional transverse modulators exhibit a 2.3 dB modulation depth.

Recently, there has been increased interest in utilizing large refractive index changes associated with the QCSE in MQW structures [Gli86, Wei87, Zuc88b]. The large change in electroabsorption due to the QCSE causes a significant dispersion of refractive index near the bandgap. The refractive index change in MQW structures has been known to be due to the linear and quadratic electro-optic effects, which are much larger than those in the bulk material [Zuc88a]. This means that it is possible to develop extremely efficient phase modulators and electro-optic devices by using MQW structures. These applications will be further discussed later in chapter six.

Although we limit our discussion only to the QCSE of QW structures, there are number of other useful optical and electronic properties not

mentioned in this section. For example, significant nonlinear optical properties capable of producing fast all-optical switches and mode-locked diode lasers, are a case in point. Self-electrooptic effect device (SEED) for fast optical switching is another example that only QW structures can provide. Besides the optical devices, high-speed electronic devices and high-gain avalanche photodetectors are some other examples where QW structures with some modifications such as graded bandgaps and modulation doping are often used.

CHAPTER THREE REFRACTIVE INDEX CHANGE IN GaAs P-N JUNCTION

3.1. Introduction

The p-n junction, formed by bringing together and contacting p- and n-semiconductors metallurgically, is a basic structure for electronic devices as well as optical devices which utilize efficient carrier injection and depletion. The p-n junctions are characterized by a space charge region (or the depletion region) near the junction, resulting in an electric field across the depletion region. The resultant electric field causes drift current in the direction opposite to that of diffusion current by the electrons and holes. Build-up of the resultant electric field is continued by depleting more carriers from the junction boundaries until the net current by diffusion and drift becomes zero. It is said at this point that the p-n junction is at equilibrium. Since any gradient of the Fermi level implies a net current, the Fermi levels of the p- and n-type materials should be constant at equilibrium throughout the device including the junction. Hence, this causes a built-in potential barrier across the junction, splitting the bands of both sides, as the Fermi levels for the p- and n-type materials are different. The built-in potential can be obtained by integrating the resultant electric field over the depletion region. It acts as a potential barrier impeding the majority carriers to diffuse, balancing the current components produced by the diffusion and drift.

The material property in the depletion region is changed due to the carrier depletion and the resultant electric field. As discussed in chapter two, absorption in the depletion region is expected to be different from the neutral region outside the space charge region. Any absorption change causes a refractive index change in the depletion region via the Kramers-Kronig relation, given in Eq.(2.6). As we apply bias voltages in order to inject or deplete more carriers, additional refractive index change occurs.

In this chapter, we discuss the refractive index changes induced in a p-n GaAs junction under the forward and reverse biased conditions. Since the two bias states correspond to the operating conditions of lasers and modulators, results concluded in this chapter will be very useful for us to analyze the optical devices in the next two chapters. The refractive index changes are known to be due to complex physical phenomena caused by the presence of free carriers and the electric field. Hence, in order to include them systematically in theoretical calculations, it is desirable to formulate them with simple equations each representing the corresponding physical mechanism.

3.2. Forward Biased Condition

As a forward bias voltage is applied to a p-n GaAs junction, a current flows through the junction. The current flow is attributed to the disturbance of equilibrium condition in the junction by the applied voltage: The equilibrium built-in potential is lowered by the applied voltage, decreasing the electric field in the depletion region. The built-in potential of a GaAs p-n junction is typically around 1 eV, and application of a small forward bias voltage is sufficient to annul this electric field. Decrease of the electric field

allows the carriers to compensate ionized impurities, reducing the depletion region. As a result, the balance between the diffusion and drift forces is broken, resulting in a net current mainly due to carrier diffusion over the reduced potential barrier. Large numbers of electrons and holes are injected into the p- and n-type neutral regions near the depletion edges by diffusion current.

The presence of excess carriers then causes significant changes in the optical properties. The refractive index change due to carrier injection is associated with variations of two kinds of absorption phenomena: One is the change of free carrier absorption far below the bandgap (Fig.2.2), which leads to the free carrier plasma (PL) effect. The other is the change of fundamental band-to-band absorption near the bandgap (Fig.2.3), which leads to the bandgap shift (BS) effect. The free carrier absorption increases by the injection of free carriers, due to an increased number of free carriers participating in the intraband and intersubband transitions in the conduction or valence band. On the other hand, the probability of band-to-band transitions decreases with decreasing empty states in the conduction band or filled states in the valence band. The fundamental absorption, hence, decreases just above the bandgap.

As a result of these absorption changes, the refractive index in the injection region is altered by the Kramers-Kronig dispersion relation given by Eq.(2.6) [Ste64]. Eq.(2.6) was used to estimate the effect of the fundamental absorption edge on the refractive index, but here we need refractive index changes by only the changes of the fundamental and free carrier absorptions. Hence, the absorption coefficient $A(E)$ in Eq.(2.6) has to be replaced by the absorption change $\Delta A(E)$;

$$\Delta n(E) = \frac{hc}{2\pi^2} \int_0^E \frac{\Delta A(E)}{E^2 - E^2} dE \quad (3.1)$$

Eq.(3.1) predicts that both the mechanisms of absorption changes by the injection of free carriers make the refractive index decrease in the infrared region below the bandgap, which is the wavelength range of interest for optical devices. For example, the free carrier absorption is prominent far below the bandgap due to small energy transitions within the bands, and its change is positive. Then, the denominator and numerator in Eq.(3.1) have opposite signs, and Δn will be negative. For the fundamental absorption, they have also opposite signs, making Δn negative.

3.2.1. Free Carrier Plasma Effect

The PL effect was investigated in detail by Stern [Ste64] with the intraband and intersubband transitions of free carriers in GaAs conduction and valence bands. The effect of intraband absorption on the refractive index was modeled by a single-oscillator located at the free carrier plasma frequency. Since the frequency is far below the bandgap, the refractive index change due to the intraband absorption could be calculated with sufficient accuracy near the bandgap by using Eq.(3.1) and the single-oscillator model:

$$\Delta n_{\text{intra}}(E) = -6.9 \times 10^{-22} \left(\frac{m_0}{m^*} \right) \frac{\Delta N}{nE^2} \quad (3.2)$$

where E is the photon energy in eV, m_0 is the electron mass, m^* is the effective mass of free carrier, ΔN is the concentration of injected carrier in

cm⁻³, and n is the refractive index at the photon energy. Eq.(3.2) is applicable to electron and hole injections in GaAs and AlGaAs with proper effective masses and refractive indices.

The refractive index change due to the intersubband absorption was found to be significant only in hole injection because of direct transitions between the heavy-hole, light-hole, and split-off bands, and is expressed by an empirical equation;

$$\Delta n_{\text{inter}}(E) = -6.3 \times 10^{-22} \frac{\Delta P}{E^2} \quad (3.3)$$

where ΔP is the injected hole concentration. It is found from Eqs.(3.2) and (3.3) that for hole injection, the intersubband contribution to the refractive index change is larger than the intraband contribution. Eq.(3.3) is also used for hole injection in AlGaAs in our calculations under the assumption that the valence band structure does not change significantly in AlGaAs with an AlAs mole fraction of less than 0.4.

3.2.2. Band Shift Effect

As we discussed in section 2.2, the band-filling (BF) and bandgap shrinkage (BGS) effects occur near the bandgap simultaneously by the injection of free carriers. Therefore, we define the BS effect as a combined effect of the BF and BGS effects. The refractive index change Δn_{BS} due to the BS effect has been extensively studied for doped GaAs [Sel74, Zor73a], and for carrier injection in semiconductor diode lasers [Hen81, Man83, Men80]. As free carriers are injected, the conduction band states will be filled by electron injection and the valence band states will be empty by hole

injection. This corresponds to an increase of an effective optical bandgap, i.e., the band-filling effect. Hence, the fundamental absorption edge looks like shifting to higher energies, decreasing absorption just above the bandgap. However, the decrease of absorption is somewhat compensated by a bandgap decrease, i.e., the bandgap shrinkage effect, which is due to reduced coulombic interaction by carrier screening. Then, the net absorption change by carrier injection near the bandgap causes a refractive index change via the Kramers-Kronig relation of Eq.(3.1).

Mendoza-Alvarez et al. [Men87, Men88] reported results of the refractive index change due to the band-filling effect in GaAs and AlGaAs, calculated from the theoretical absorption spectra $A(E)$ using a parabolic-band model. Recently, Faist and Reinhart [Fai90] reported semi-empirical expressions of Δn_{BS} including the band-filling and bandgap shrinkage effects. Both results show linear dependence of Δn_{BS} on the carrier concentration and good agreements with Henry's data [Hen81] below the bandgap. However, we discovered a large difference between their results of Δn_{BS} by electron and Δn_{BS} by hole. For example, although at given electron and hole concentrations, the sum of the refractive index changes by both types of carriers is almost the same in both the models, Mendoza's results show a 20:1 ratio between electron and hole contributions, and Faist's results give a 1.4:1 ratio. On the other hand, according to our calculations, using the experimental absorption spectra reported by Casey et al. [Cas75], the ratio is found to be 3.5 for the same concentrations of electrons and holes ($5 \times 10^{17} - 3 \times 10^{18} \text{ cm}^{-3}$).

Therefore, using this ratio and a single-oscillator model for the fundamental absorption change by carrier injection, a semi-empirical equation for Δn_{BS} in $\text{Al}_x\text{Ga}_{1-x}\text{As}$ is derived as follows;

$$\Delta n_{BS}(E) = - B(E) \Delta N \quad (3.4)$$

where

$$B(E) = \frac{S_b}{2n [E_b(x)^2 - E^2]}$$

$$S_b = 1.37 \times 10^{-20} \text{ eV}^2 \text{cm}^3 \quad \text{for electron}$$

$$3.91 \times 10^{-21} \text{ eV}^2 \text{cm}^3 \quad \text{for hole}$$

$$E_b(x) = 1.45 + 1.247 x$$

$B(E)$ is the BS coefficient, $E_b(x)$ and S_b are the position and strength of the single-oscillator for the fundamental absorption change near the bandgap, x is the AlAs mole fraction, and ΔN is the injected carrier concentration. Refractive index changes for electron concentration of 1×10^{18} and hole concentration of $1.3 \times 10^{18} \text{ cm}^{-3}$, calculated by using Eq.(3.4), is presented in Fig. 3.1. They shows excellent agreements up to $E = 1.4 \text{ eV}$ with Henry's data measured in GaAs/AlGaAs diode lasers with the same amount of carrier injection. Refractive index changes by hole injection are much smaller than those by electron injection, which implies that the bandgap shrinkage effect is significant for the hole injection case. The BS coefficient is a strong function of photon energy. It increases dramatically as the photon energy approaches the bandgap energy because the absorption change due to the BS effect occurs dominantly near the bandgap.

3.3. Reverse Biased Condition

As a reverse bias voltage is applied to a p-n GaAs junction, most of the applied voltage appears across the junction, increasing the potential

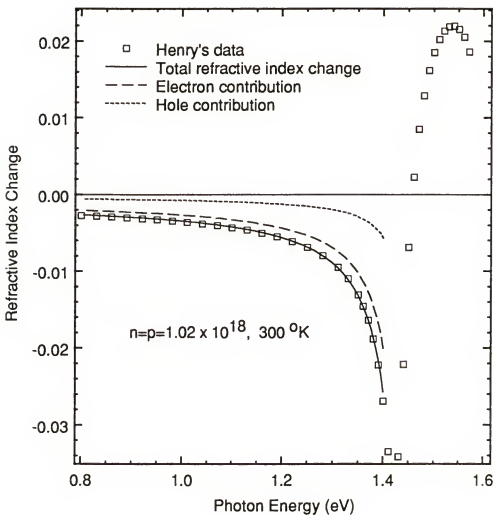


Figure 3.1 Calculated refractive index changes due to the bandgap shift (BS) effect by using Eq.(3.4). The same amount of electrons and holes ($1.02 \times 10^{18} \text{ cm}^{-3}$) is injected. The ratio of refractive index changes due to the electrons and holes is estimated to be 3.5.

barrier between the p- and n-type materials. Responding to the increased potential barrier, free carriers are removed from the depletion edges which widens the depletion region, and hence increases the electric field inside the depletion region. The carrier depletion causes refractive index change which is reverse to the carrier injection case. The presence of electric field increases absorption near the bandgap via the Franz-Keldysh effect (Fig.2.4), causing an additional refractive index change in the depletion region. Regardless of the absorption change, the well-known linear electro-optic effect is always present.

3.3.1. Carrier Depletion Effect

The carrier depletion is an exact reverse process to the carrier injection. Hence, all the equations for the refractive index change developed in the previous section can be applied to the reverse biased junction by changing the sign. In the carrier injection case, the same amount of electrons and holes are injected into each side of the junction at the same time. But, in the carrier depletion case, the majority carriers, i.e., electrons from the n-type GaAs and holes from the p-type GaAs, are completely depleted. Therefore, we just need to consider one type of carriers in each side, replacing the injected carrier concentration ΔN with the majority carrier concentration N in the equations.

The PL, BF, and BGS effects were developed for the carrier injection case or for highly-doped semiconductors, and they are well understood conceptually. Generation of new terminologies for the carrier depletion case might cause confusion and be useless. Hence, we are going to use the same terminologies for the depletion case as used in the injection case.

3.3.2. Linear Electro-Optic Effects

When we apply an electric field to certain optically isotropic but non-centrosymmetric crystals they become birefringent. The induced birefringence is the result of the linear electro-optic effect (or the Pockel's effect) and is proportional to the applied electric field. Namba [Nam61] has studied the LEO effect in zinc-blende crystals by using an index ellipsoid with the electric field applied along various crystal directions. In the presence of the electric field for crystals of the zinc-blende such as GaAs, the perturbed index ellipsoid can be expressed by

$$\frac{1}{n^2} (x^2 + y^2 + z^2) + 2r_{41} (F_x y z + F_y x z + F_z x y) = 1 \quad (3.5)$$

where r_{41} is the LEO coefficient, and F_x , F_y , and F_z are the x, y, and z components of the applied electric field, respectively.

For an applied electric field F along the [001] direction (Fig.3.2), which is the most practical direction for compound semiconductor devices, the principal axes (x' , y') of the perturbed index ellipsoid are rotated by 45° from the major axes (x, y) of the unperturbed index ellipsoid. The directions x' and y' are the [110] and $[\bar{1}10]$ crystal directions, respectively. Assuming $F \cdot r_{41} \ll n^{-2}$, the refractive indices along the [110] and $[\bar{1}10]$ directions are given by

$$n_{[110]} = n + \frac{n^3}{2} r_{41} F \quad (3.6)$$

$$n_{[\bar{1}10]} = n - \frac{n^3}{2} r_{41} F$$

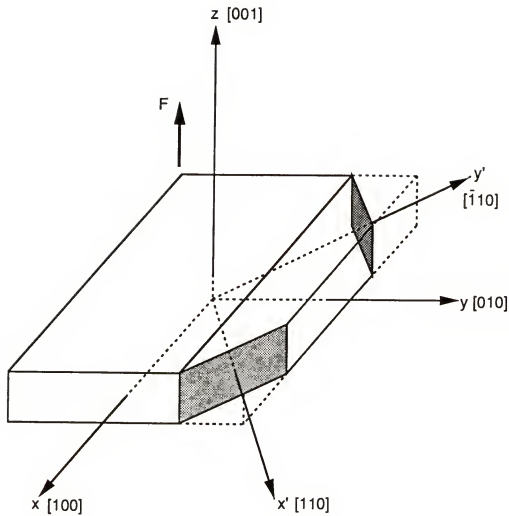


Figure 3.2 Principal axes of index ellipsoid and corresponding crystal directions. The new axes of the perturbed index ellipsoid are rotated by 45 degree from the major axes of the unperturbed index ellipsoid.

Therefore, the refractive index change due to the LEO effect is given by

$$\Delta n_{\text{LEO}} = \pm \frac{n^3}{2} r_{41} F \quad (3.7)$$

The plus and minus signs corresponds to the [110] and [−110] directions, respectively, as seen in Eq.(3.6).

A propagating optical field experiences a different refractive index depending on its polarization and the propagation direction. For example, if we consider a TE mode propagating along the [−110] direction, it experiences an increased refractive index (the plus sign in Eq.(3.7)) since its electric component is parallel to the [110] direction. On the other hand, a TE mode propagating along the [110] direction sees a decreased refractive index indicated by the minus sign in Eq.(3.7). In the latter case, the LEO contribution to the refractive index change subtracts from the contributions of the PL and BS effects which are independent on the propagating direction and induce a positive index change in the depletion region. For a TM mode with its electric component polarized along the [001] direction, no contribution due to the LEO effect occurs for an electric field applied along the [001] direction.

Faist et al. [Fai87b] have reported the propagation direction and polarization dependences of the LEO effect experimentally in GaAs/AlGaAs phase modulators. Recently, these authors have also shown a dispersion of r_{41} near the bandgap [Fai90]. The r_{41} values of $1.72 - 1.68(\pm 0.08) \times 10^{-10} \text{ cm/V}$ were measured at $\lambda = 1.09 - 1.15 \mu\text{m}$, which are slightly larger than the commonly used value of $1.5 \times 10^{-10} \text{ cm/V}$ far from the bandgap.

3.3.3. Quadratic Electro-Optic Effect

As discussed in section 2.2, the conduction and valence bands are tilted in the depletion region by the electric field. This increases the probability of finding an electron within the band gap and consequently absorption increases below the fundamental absorption edge. The absorption edge appears to shift to lower energies, but actually broadens, which is known as the electroabsorption or the Franz-Keldysh effect [Cal63, Tha63]. It is a companion effect of the electrorefraction. They are related to each other by the Kramers-Kronig relation in Eq.(3.1), making the refractive index increase at photon energies below the bandgap in the same way as the BS effect.

Recently, the refractive index change due to the Franz-Keldysh effect was shown to have a quadratic dependence on the applied electric field [Alp87a, Fai87b]. The refractive index change due to the quadratic electro-optic (QEO) effect can be represented by

$$\Delta n_{\text{QEO}}(E) = \frac{n^3}{2} R(E) F^2 \quad (3.8)$$

where R is the QEO coefficient. Experimental and theoretical values of R near the GaAs bandgap [Fai87b, Men88] show that the QEO effect is independent of both the propagation direction and polarization of the guided mode. However, very recently, Faist and Reinhart [Fai90] have reported certain polarization dependence of R experimentally. This effect, if any, was too small to be measured. The QEO coefficient depends on photon energy as strongly as the BS coefficient $B(E)$ in Eq.(3.4). As the photon

energy shifts toward the GaAs bandgap, the QEO effect will increase more dramatically than the BS effect because the absorption change due to the QEO effect occurs at lower energies than that due to the BS effect. The absorption edge of AlGaAs is far above the operating photon energies useful for GaAs /AlGaAs phase modulators. Thus, the QEO effect in AlGaAs is considerably smaller than that in GaAs at the operating photon energies. The P-p-i-n-N structure, designed to achieve high performance phase modulation [Lee90], which is the subject of detailed study in chapter five, overcomes this problem, by utilizing the QEO effect of the buffer GaAs layers.

CHAPTER FOUR LASER GEOMETRY DEPENDENCE OF LINewidth IN (AlGa)As LASERS

4.1. Introduction

It is well known that the lasing photon energy in a semiconductor diode laser does not coincide with the energy at which the refractive index change is zero, because of carrier transitions between conduction and valence bands [Hen81, Nas73]. This causes beam profiles to alter and additional phase fluctuations due to intensity variations broaden the laser linewidth. The refractive index change due to the gain change in semiconductor diode lasers has been an important parameter since it was introduced as an antiguiding factor for finding out beam profiles including phenomena related to the spatial hole burning [Kir77, Lan79, Str79, Str81]. In addition, the linewidth broadening of single-mode (AlGa)As lasers measured by Fleming and Mooradian [Fl81] was successfully accounted for by Henry [Hen82] employing the linewidth enhancement factor.

A significant amount of data related to the linewidth enhancement factor α has been reported. The values of α range between 0.5 and 8 for (AlGa)As lasers. Since each value of α was measured in a particular laser structure, the reason for such a wide distribution has not been clarified. Some researchers [Oga84, Vah83] have calculated variation of α as a function of carrier density injected into the active layer, assuming parabolic conduction and valence bands. The results show that α decreases with an

increase of the injected carrier density, and hence of the lasing photonenergy, and even becomes negative at higher photon energies. However, the lasing photon energy of a conventional diode laser usually lies below the bandgap energy [Hen80, Hen81, Str83] and the exact value of the injected carrier density is hard to evaluate both experimentally and theoretically. Thus, the previous results only provide a general trend of the α dependence on injection level and hardly account for its dependence on laser geometry. Arakawa and Yariv [Ara85] showed that α decreases with an increase of the loss, which consists of the internal waveguide loss and the mirror loss. The loss was used to estimate the quasi-Fermi levels in parabolic conduction and valence bands. Although this calculation also has the same problem as the above case, it was shown in a qualitative manner that α depends on laser length and facet reflectivity.

In this chapter, we propose a reliable method for calculating the linewidth enhancement factor and its dependence on laser geometry. The method utilizes absorption data of the active layer in (AlGa)As lasers. As a fundamental parameter of the material itself, the absorption coefficient is a function of the injection level, and its variation has been used to calculate the refractive index change Δn via the Kramers-Kronig dispersion relations in Eq.(3.1). By using a simple exponential absorption edge, Streifer et al. [Str83] derived a formula for the lasing photon energy dependence on device parameters including the active layer thickness, laser length, etc. We have combined these calculations to obtain an analytical relation between α and the laser geometry, which is described in section 4.2.

In section 4.3, the lasing photon energy, the gain change, the refractive index change, and α are evaluated as functions of active layer thickness and laser length based on an assumption, which simplifies the

calculations and still ensures relatively small errors. These calculated results are presented and compared to the reported experimental data in order to verify the utility of our calculation model and the validity of the assumptions. In addition, the α dependence on laser type is discussed qualitatively. The α dependence on the lateral waveguide structure of semiconductor lasers has been analyzed by Furuya [Fur85], introducing an effective α . Theoretical calculations show that α is enhanced from its intrinsic value in weak index-guide and gain-guide structures, which correspond to CSP(channel-substrate-planar) and stripe-geometry lasers, respectively. Comparing the reported experimental data to Furuya's analysis, it is found that not only is the intrinsic α strongly dependent on waveguide structure, but also its dependence on waveguide structure is more dominant than the effective α dependence. This will be discussed in detail in section 4.3. Lastly, using the calculated results, we suggest a practical method for the reduction of the linewidth in a diode laser, by reducing the active layer thickness, increasing the device length, and applying high reflectivity coatings. The latter two techniques have been previously discussed qualitatively [Ara85, Len84].

4.2. Analytical Model for Linewidth Enhancement Factor

To obtain analytical expressions for the gain change Δg and the refractive index change Δn , the absorption coefficient has to be given in a form integrable in the Kramers-Kronig dispersion relation. As a result of carrier transitions involving band tails (Eq.(2.2)), an exponentially increasing absorption edge is widely used up to an energy E_c near the bandgap [Ste64, Str83, Man83]. The exponential absorption edge plays an

important role in our model since most of conventional diode lasers lase in this region. Stern [Ste64] suggested two expressions for the absorption coefficient in the region above E_c . The first expression is the square-root expression (Eq.(2.1)) representing allowed-direct transitions between conduction and valence bands, but not integrable. As can be seen later in this section, we need two absorption spectra (without and with pumping) to calculate the dispersion of Δn . The second expression has an integrable form, and describes well the absorption spectrum with pumping which shows relatively slow variation near the bandgap energy [Hen81]. However, it does not fit the absorption spectrum without pumping or with low pumping because of the rapid increase of the absorption coefficient near the bandgap energy. Therefore, a practical expression which is integrable and fits both cases is suggested in order to obtain useful results.

In the above expressions, the entire absorption spectrum was divided into two parts at E_c so that two different equations could describe the absorption over the entire range. The absorption coefficient A can be approximated by the following expression:

$$A(eV, E) = B \exp [\sigma (E - E_c)] , \quad E \leq E_c \quad (4.1)$$

$$B \left[1 + \frac{(E - E_c)}{E_1} \right] , \quad E_c \leq E \leq E_c$$

$$B \left[1 + \frac{(E - E_c)}{E_2} \right] , \quad E_c \leq E$$

where eV is the separation of the quasi-Fermi levels in conduction and valence bands [Hen80], E_c is the upper limit to which the exponential

expression for A can be applied, and E_c' is chosen suitably by curve fitting to the experimental absorption data. The parameter σ represents the steepness of the exponential absorption edge, and varies depending on doping level, temperature and aluminum mole fraction of the active layer in a diode laser [Cas75, Hen80, Hen81]. B' is given by setting the second and the third equations in Eq.(4.1) equal at E_c' . This expression provides a convenient way to find out the unknowns involved in Eq.(4.1) from the measured absorption spectra.

The gain spectrum is given by [Hen81, Str83]

$$g(eV, E) = A_p(eV, E) - A(eV, E) \quad (4.2)$$

where $A_p(eV, E)$ is the pumping dependent gain, which represents the actual material gain supplied by pumping during the transition from absorption to gain. Then, using Eq.(4.1), the pumping dependent gain can be represented as

$$A_p(eV, E) = B_p \exp[(\sigma - k)(E - E_c)] , \quad E \leq E_c \quad (4.3)$$

$$B_p \left[1 + \frac{(E - E_c)}{E_1} \right] \exp[-k(E - E_c)] , \quad E_c \leq E \leq E_c'$$

$$B_p' \left[1 + \frac{(E - E_c)}{E_2} \right] \exp[-k(E - E_c)] , \quad E_c' \leq E$$

where $k = (\kappa T)$ is the reciprocal Boltzman temperature equivalent and $B_p = B \exp[k(eV - E_c)]$. B_p' is determined in the same way as in Eq.(4.1). Assuming that lasing occurs at the maximum gain energy near the absorption edge,

we can obtain the lasing photon energy E_L and the magnitude of the pumping dependent gain at threshold $(B_p)_{th}$ by setting the derivative of Eq.(4.2) equal to zero [Str83].

$$E_L = E_c + \frac{1}{\sigma} \ln \left\{ \frac{(\sigma - k)}{k\Gamma B} \left[\frac{1}{2L} \ln \left(\frac{1}{R_1 R_2} \right) + \alpha_i \right] \right\} \quad (4.4)$$

$$(B_p)_{th} = \frac{\sigma B}{(\sigma - k)} \exp \left[k (E_L - E_c) \right] \quad (4.5)$$

where Γ is the mode confinement factor perpendicular to the waveguide, L the laser length, R_1 and R_2 the power reflectivities of both facets, and α_i the internal waveguide loss. The significance of Eqs.(4.4) and (4.5) is that they allow us to evaluate Δg , Δn , and α as a function of only the material properties of the active layer and waveguide parameters, without using uncertain parameters such as injected carrier density and quasi-Fermi levels.

The gain change $\Delta g(eV, E)$ is defined as the absorption change with pumping when the bias voltage across the active layer varies from zero to V , and is given by

$$\Delta g(eV, E) = g(eV, E) + A(0, E) \quad (4.6)$$

where $A(0, E)$ is the absorption spectrum without pumping. In addition, the refractive index change $\Delta n(eV, E)$ can be calculated by using Eq.(4.6) via the Kramers-Kronig dispersion relation in Eq.(3.1).

$$\Delta n(eV, E) = \frac{hc}{2\pi^2} \int_0^{E_s} \frac{A_p(eV, E) - A(eV, E) + A(0, E)}{E^2 - E^2} dE \quad (4.7)$$

where E_s is chosen as an energy above which $A(eV, E)$ and $A(0, E)$ have a constant value so that the integration of these terms from E_s to infinity should be zero. Above E_s , the only possible contribution to Δg and Δn comes from the pumping gain $A_p(eV, E)$, but it is also negligible as can be seen in Eq.(4.3). Hence, Eq.(4.7) is expected to be sufficiently accurate. After elaborate derivations, the integration of each term in Eq.(4.7) is given by

$$2E \int_0^{E_s} \frac{A_p(eV, E)}{E^2 - E^2} dE = B_p e^{(\sigma-k)(E-E_c)} Ei((\sigma-k)(E_c - E)) + \quad (4.8)$$

$$B_p \left(1 + \frac{(E-E_c)}{E_1} \right) e^{-k(E-E_c)} \{ Ei(-k(E_c - E)) - Ei(-k(E_c + E)) \} +$$

$$B_p \left(-1 + \frac{(E+E_c)}{E_1} \right) e^{k(E+E_c)} \{ Ei(-k(E_c + E)) - Ei(-k(E_c - E)) \} +$$

$$B_p \left(1 + \frac{(E-E_c)}{E_2} \right) e^{-k(E-E_c)} \{ Ei(-k(E_s - E)) - Ei(-k(E_c - E)) \} +$$

$$B_p \left(-1 + \frac{(E+E_c)}{E_2} \right) e^{k(E+E_c)} \{ Ei(-k(E_s + E)) - Ei(-k(E_c + E)) \}$$

$$2E \int_0^{E_s} \frac{A(eV, E)}{E^2 - E^2} dE = B e^{\sigma(E - E_c)} Ei(\sigma(E_c - E)) + \quad (4.9)$$

$$B \left(1 + \frac{(E-E_c)}{E_1} \right) \ln \frac{|E_c - E|}{|E_c + E|} + B \left(-1 + \frac{(E+E_c)}{E_1} \right) \ln \frac{E_c + E}{E_c - E} +$$

$$B \left(1 + \frac{(E-E_c)}{E_2} \right) \ln \frac{E_s - E}{|E_c - E|} + B \left(-1 + \frac{(E+E_c)}{E_2} \right) \ln \frac{E_s + E}{E_c + E}$$

where $Ei(x)$ is the exponential integral [Bey81].

The linewidth enhancement factor α is defined as the ratio of the refractive index change to the gain change induced by small variation of injected carriers at the operating point.

$$\alpha \equiv \left(\frac{4\pi}{\lambda_L} \right) \left(\frac{\Delta n}{\Delta g} \right) \quad (4.10)$$

where λ_L is the lasing wavelength. In a GaAs/(AlGa)As (GaAs active layer) laser, the dependence of the gain on injected carrier density dg/dN is almost linear and that of the refractive index dn/dN is slightly sublinear [Hen81]; hence, the direct ratio of $\Delta n(eV_{th}, E_L)$ and $\Delta g(eV_{th}, E_L)$ can be used for the α calculation with only a small error. However, in lasers with an (AlGa)As active layer, dg/dN is negligible at low injection due to the bandgap shrinkage [Hen80], which shifts the absorption edge to the lower energy side and prevents the increase of Δg with increasing N , and the resultant dn/dN is presumed to be nonlinear, discussed in detail in section 4.3. This makes the direct ratio useless for (AlGa)As lasers. Therefore, following the definition of α , Δg and Δn between two injection levels near threshold will be used, and this provides more accurate values of α since dg/dN and dn/dN are linear near and above threshold for both GaAs/(AlGa)As and (AlGa)As lasers [Hen80, Hen81, Man83].

4.3. Laser Geometry Dependences

For our calculations of α , we adopted the absorption data of GaAs/AlGaAs and (AlGa)As lasers in Refs.[Hen81] and [Hen80], respectively. The values of unknown parameters used in our calculations

are listed in Table 4.1 where $A(eV_{th}-\Delta eV, E)$ is the absorption spectrum at an injection level less than threshold by ΔeV and it was estimated for the (AlGa)As laser from measured spontaneous emission spectra. Using Eqs.(4.1)-(4.9) and the absorption data, we can calculate the dispersions of $\Delta g(eV, E)$ and $\Delta n(eV, E)$ for two injection levels of eV_{th} and $eV_{th}-\Delta eV$. Since dg/dN and dn/dN are linear near threshold and are functions of wavelength, the dispersion of α can be estimated from the calculated dispersions of $\Delta g(eV, E)$ and $\Delta n(eV, E)$. Therefore, if we know the E_L dependence on laser geometry, the α dependence can be obtained.

As can be seen from Eq.(4.4), E_L involves the parameters E_c , σ , and B of the absorption spectrum at threshold, which changes with laser geometry due to the change of threshold carrier density. In our calculations, we assume that the absorption spectrum at threshold does not change with laser geometry so that $A(eV_{th}, E)$ in Table 4.1 can be used for the calculations of the E_L dependence on laser geometry. Therefore, it is important to estimate the errors in E_L and α caused by this assumption.

The threshold carrier density can be approximated by

$$N_{th} = \frac{\eta_i \tau_s}{q} \left(\frac{J_{th}}{t} \right) \quad (4.11)$$

where η_i is the laser internal efficiency, τ_s is the radiative recombination lifetime, and t is the active layer thickness. Since devices used in our calculations have the exponential slope σ of 88-130 and the refractive index step of 0.25 - 0.3 [Hen80, Hen81], we estimate from prior publications [Bot79, Str83] that J_{th}/t increases by a factor of 2 as t decreases from 0.25 to 0.05 μm . On the other hand, η_i decreases with the decrease of t mainly due to the

Table 4.1 Numerical values used for the calculated curves of Figures 4.1 - 4.3.

Active Layer	$A(eV, E)$	B [cm $^{-1}$]	σ [eV $^{-1}$]	E_c [eV]	E_c' [eV]	E_1 [eV $^{-1}$]	E_2 [eV $^{-1}$]	E_s [eV]	ΔeV [eV]
GaAs	$A(0, E)$	4500	100	1.424	1.44088	0.01899	0.16343	1.5748	---
	$A(eV_{th} - \Delta eV, E)$	1200	89	1.424	1.4632	0.012379	0.05332	---	0.0179
	$A(eV_{th}, E)$	900	86	1.424	1.4508	0.013	0.02688	---	---
AlGaAs	$A(0, E)$	2800	130	1.5248	1.5413	0.006666	0.20609	1.6529	---
	$A(eV_{th} - \Delta eV, E)$	1450	112	1.5248	1.5661	0.01006	0.08458	---	0.0124
	$A(eV_{th}, E)$	1200	107	1.5248	1.5744	0.00895	0.08619	---	---

* The internal waveguide loss, $\alpha_i = 20 \text{ cm}^{-1}$ and the facet reflectivity, $R = 0.31$ have been used for both devices.

decrease of carrier confinement in the narrow active region [Cas78]. τ_s also becomes smaller with the increase of injected carriers. Therefore, the threshold carrier density and the absorption spectrum at threshold are expected to change slightly as t varies between 0.05 and 0.25 μm , which is the t region of our interest. This qualitative analysis can be partially supported by the experimental results of Manning et al. [Man83], which show that J_{th}/t increases by 40 percent and N increases only by 16 percent as t decreases from 0.19 to 0.07 μm for (AlGa)As lasers with $L = 250 \mu\text{m}$.

In order to estimate the errors in E_L and α caused by our assumption, let us assume that $A(eV_{\text{th}}, E)$ and $A(eV_{\text{th}} - \Delta eV, E)$ in Table 4.1 are the absorption spectra at threshold for two GaAs/(AlGa)As lasers with different active layer thicknesses. The injected carrier densities for the above absorption spectra differ by 30 percent [Hen81]. When we calculate E_L from these absorption spectra for the same geometry of $t = 0.2 \mu\text{m}$ and $L = 300 \mu\text{m}$, we find from Eq.(4.4) that the calculated values of E_L differ by only $\sim 15 \text{ \AA}$. This difference in E_L causes an error of less than 1 in the calculated value of α , as will be seen in Fig.4.6. Also, from the absorption spectra for carrier densities of 2×10^{18} and $3.3 \times 10^{18} \text{ cm}^{-3}$ [Cas75], the E_L difference is estimated to be ~ 20 and $\sim 40 \text{ \AA}$ for $t = 0.2$ and $0.1 \mu\text{m}$, respectively. The resultant error in the magnitude of α is ~ 1 . The dispersions of α calculated by Vahala et al. [Vah83] and Ogasawara et al. [Oga84] also show that the magnitude of α increases by ~ 0.7 at a fixed photon energy when the injected carrier density increases from 1.8 and 2×10^{18} to 2.5 and $3 \times 10^{18} \text{ cm}^{-3}$, respectively. Therefore, the calculated values of α under the assumption are expected to be accurate within the magnitude error of less than 1 in the geometry range of interest.

4.3.1. Lasing Photon Energy, Gain Change, and Refractive Index Change

Fig.4.1 shows the E_L dependence of a GaAs/(AlGa)As laser on active layer thickness with laser length as a parameter, which has also been reported by Streifer et al. [Str83] with the exponential slope of the absorption spectrum as a parameter. The lasing photon energy moves up toward E_c as t and L decrease, and shifts ~ 0.023 eV between $t = 0.25$ and 0.05 μm , which agrees well with the results of Streifer et al. The effects of t and L variations are involved in the mode confinement factor and the threshold gain in Eq.(4.4), respectively. Since Γ is proportional to t^2 for small values of t in a symmetrical waveguide, the effect of the t variation is much larger than the L variation. The same dependence is found in an (AlGa)As laser except that the shift is a little smaller due to the larger exponential slope of the absorption spectra than that in a GaAs/(AlGa)As laser.

The gain change and the refractive index change at threshold are given in Figs.4.2 and 4.3, respectively. As can be seen in Eqs.(4.2) and (4.6), the gain change at threshold is obtained by summing up the absorption difference $\Delta A = A(0, E) - A(eV_{th}, E)$ and the pumping dependent gain $A_p(eV_{th}, E)$. $\Delta g(eV_{th}, E)$ significantly increases due to the rapid increase of these two terms as t and L decrease. ΔA arises from the band-filling effect resulting from the injected carriers, and the maximum change occurs above the bandgap [Hen80, Hen81]. Therefore, ΔA increases as E_L moves to higher energies in the exponential absorption edge. $A_p(eV_{th}, E)$ also increases with the increase of E_L , as can be seen in Eqs.(4.3) and (4.5), which show that it increases by a factor of 2.4 for an E_L increase of 0.01 eV in the GaAs/(AlGa)As laser.

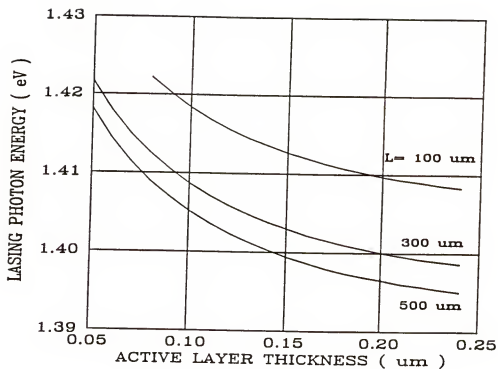


Figure 4.1 Dependence of lasing photon energy on active layer thickness with laser length as a parameter for GaAs/AlGaAs lasers.

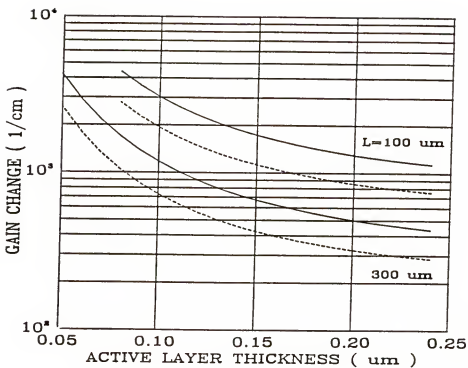


Figure 4.2 Dependence of gain change at threshold on active layer thickness with laser length as a parameter: Solid lines for GaAs/AlGaAs lasers and dashed lines for (AlGa)As lasers with active layer of AlAs mole fraction, $x = 0.08$.

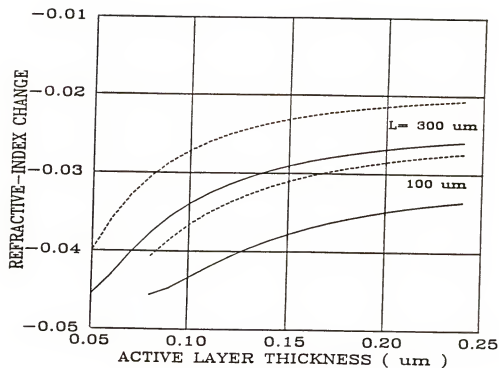


Figure 4.3 Dependence of refractive index change at threshold on active layer thickness with laser length as a parameter: Solid lines for GaAs/AlGaAs lasers and dashed lines for (AlGa)As lasers with active layer of AlAs mole fraction, $x = 0.08$.

Figs.4.2 and 4.3 compare the differences of $\Delta g(eV_{th}, E_L)$ and $\Delta n(eV_{th}, E_L)$ between GaAs/(AlGa)As and (AlGa)As lasers, respectively. As mentioned in section 4.2, dg/dN is nonlinear, particularly at low injection in the (AlGa)As lasers [Hen80]. This is because the bandgap shrinkage effect is comparable to the band-filling effect in (AlGa)As active layers. The band-filling effect is the dominant mechanism for GaAs active layers, and shifts the absorption spectrum to higher energies [Hen81]. On the other hand, the bandgap shrinkage effect shifts the absorption spectrum to lower energies. These opposite effects restrain the absorption spectrum from shifting as a function of injected carrier, and the pumping dependent gain is also negligible at low injection. Therefore, dg/dN in the (AlGa)As lasers is almost zero at low injection for photon energies below the bandgap, and we know from Eqs.(4.6) and (4.7) that Δg and Δn should be smaller in an (AlGa)As laser than a GaAs/(AlGa)As laser for the same laser geometry due to small ΔA of an (AlGa)As laser.

Butler and Botez [Bu82] have reported $\Delta n = 0.028$ and 0.02 for $t \approx 0.086$ and $0.14 \mu\text{m}$, respectively, which agree well with the calculated values of Δn for (AlGa)As lasers with $L = 350 - 400 \mu\text{m}$. Refractive index changes of $0.03 - 0.06$ have been reported for (AlGa)As lasers with $L = 200 - 430 \mu\text{m}$ and $t = 0.05 - 0.19 \mu\text{m}$ by Manning et al. [Man83]. Our calculations in Fig.4.3 predict Δn values in the range of $0.022 - 0.043$ for a similar laser geometry. This discrepancy is considered to come from very high N_{th} ($3.2 - 4.7 \times 10^{18} \text{ cm}^{-3}$) of the (AlGa)As lasers used in the measurement. However, if we consider small increments of Δn at low injection levels as discussed above, this discrepancy can partly come from the fact that the large experimental values of Δn were obtained by assuming that Δn increases linearly as the injected carrier density changes from zero to threshold. To support our

hypothesis, we have calculated Δn by shifting the absorption spectrum so that dg/dN at $E = E_L$ could be linear. The amount of shift was 0.012 eV, which corresponds to the bandgap shrinkage reported by Henry et al. [Hen80]. The calculated Δn was found to be 0.028 - 0.05, which is comparable to the reported experimental values except extremely large Δn of 0.063.

4.3.2. Linewidth Enhancement Factor

Various values of the calculated α and the reported experimental α are given in Figs.4.4, 4.5, and 4.6 as a function of laser length, active layer thickness, and lasing wavelength, respectively. α decreases monotonically with the decrease of t and L due to the increase of E_L , which indicates that the increasing rate of Δg is much larger than that of Δn . Any significant difference in the calculated α between GaAs/ AlGaAs and (AlGa)As lasers is not found in spite of the large difference of Δn as in Fig.4.3. This implies that dg/dN and dn/dN near threshold are almost the same in both lasers. The reported experimental values of α and device parameters are summarized in Table 4.2.

Since we calculated α by using the absorption data measured in BH (buried heterostructure) lasers the calculated values of α coincide considerably well with the experimental data measured in strong index-guide lasers [Ara85, Hen81, Sch83], which are marked as open circles in Figs.4.4 and 4.5. For CSP (channeled substrate planar) [Hen83, Kik83, Kik85, Len84, Oga84], PCW (plano-convex waveguide) [Str80, Str81], and MCRW (metal-clad ridge waveguide) [Sch84] lasers which have a similar lateral waveguiding scheme, on the other hand, the calculated values are

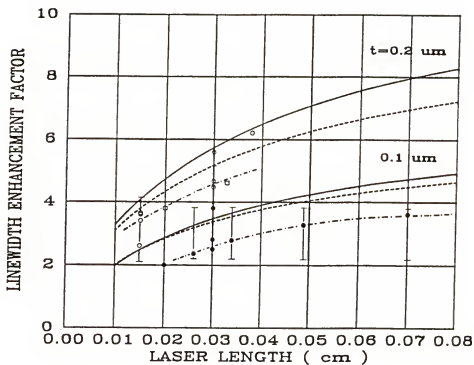


Figure 4.4 Calculated and experimental dependences of linewidth enhancement factor on laser length with active layer thickness as a parameter: Solid lines for GaAs/AlGaAs lasers and dashed lines for (AlGa)As lasers with active layer of AlAs mole fraction, $x = 0.08$. Experimental data are given in Table 4.2 with device parameters [Ara85, Hen81, Hen83, Kik85, Oga84, Sal83, Sch83, Sch84, Str80, Str81, Tur79, Vah83, Wel82].

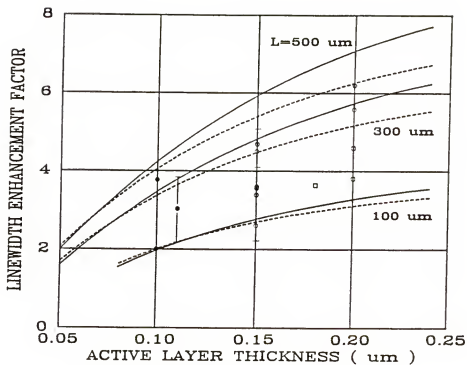


Figure 4.5 Calculated and experimental dependences of linewidth enhancement factor on active layer thickness with laser length as a parameter: Solid lines for GaAs/AlGaAs lasers and dashed lines for (AlGa)As lasers with active layer of AlAs mole fraction, $x = 0.08$. Experimental data are given in Table 4.2 with device parameters [Ara85, Har83, Hen81, Hen83, Kir77, Kik83, Kik85, Oga84, Sal83, Sch83, Str79, Str80, Tur79, Wel82].

Table 4.2 Experimental values of α and device parameters used for comparisons with calculated α in Figs.4.4 - 4.6.

Structure	Length [μm]	Active Layer Thickness [μm]	Laser Wavelength [μm]	α	Reference
BH	150	0.15*	0.8282	2.6 \pm 0.5	[Ara85]
			0.8303	3.6 \pm 0.5	
			0.8325	3.7 \pm 0.5	
	300	0.15*	0.8347	3.4 \pm 0.5	
			0.8386	4.5 \pm 0.5	
			0.8397	4.7 \pm 0.5	
BOG	---	---	0.816	4.6 \pm 1.0	[Har83]
BH	380	0.2	0.8867	6.2	[Hen81]
CSP	300	---	0.85	2.8	[Hen83]
Stripe- geometry	---	---	0.81	1.4	[Kir77]
			0.813 - 0.815	0.5 - 0.7	
			0.825	2	
			0.859	1.87	
			0.875	2.4 - 3.0	
CSP	---	---	0.84	1.3 - 2.0	[Kik83]
CSP	300	---	0.84	2.2 - 2.8	[Kik85]
CSP	300	$\sim 0.1^*$	0.824	3.8	[Oga84]

Table 4.2 Continued.

Stripe-geometry	275	0.18±0.02	0.83	3.5 - 3.8	[Sal83]
Index-guided DH	300	0.2	---	5.6	[Sch83]
Stripe-geometry	400	0.3	0.85 0.847	3 2.5	[Str79]
PCW	200	0.2 - 0.15**	0.8707	2	[Str80]
	275	0.14 - 0.12**	0.8387	2	
PCW	200	0.1	0.8512	2	[Str81]
MCRW	260 - 930	0.11	---	3±0.8	[Sch84]
TJS	329	0.2	0.83	4.6	[Tur79] [Hen82]
---	300	---	---	3.2 - 4.2	[Vah83]
TJS	200	0.2	0.842	3.8	[Wel82]
CDH-LOC	150 - 300	0.141 - 0.09 0.086 - 0.06	0.83 0.81	6 - 8 6 - 8	[But82]

* Estimated from the confinement factor or comparisons with the calculated α .

** Laterally tapered active regions.

larger by 1 - 1.5 than the experimental data, marked by closed circles. Recently, similar observations have been made by Osinski et al. [Osi87] for the reported experimental data, which show that strong index-guide lasers have larger α than CSP-type lasers. One possible reason for this discrepancy may be due to the additional absorption loss outside the channel region, which induces an increase of the total loss, and hence lasing photon energy. The other possible reason is due to a different choice of the internal waveguide loss and facet reflectivity. While we chose $\alpha_i = 20 \text{ cm}^{-1}$ in the calculations for both lasers, the recently reported values of α_i range between 30 and 45 cm^{-1} in CSP-type (AlGa)As lasers, which indicates a further reduction of the calculated α in (AlGa)As lasers.

Very large values of α were reported in CDH-LOC (constricted double-heterojunction large-optical-cavity) lasers [But82], which have thin active and guiding layers varying in thickness laterally. The reported values of α range between 6 and 8, not marked in Figs.4.4 to 4.6. Hardly explained by our model, these values may be related to the fact that a relatively small Δg (240 - 250 cm^{-1}) induced a large Δn (0.02 - 0.03) at the center region of the active layer where the optical confinement is very strong. Note that the increasing rate of Δn as a function of Δg in CDH-LOC lasers is more than twice as much as those in other laser structures [Hen81, Hen82, Oga84, Str79, Str81]. A similar discrepancy as in CSP-type lasers occurs in the experimental data measured in stripe-geometry [Kir77, Sal83, Str79] and TJS (transverse junction stripe) [Tur79, Wel82] lasers, marked by open squares. In particular, simple stripe-geometry lasers show the lowest α values of 0.5 - 2 [Kir77]. This may be due to the weak lateral mode guiding and the current spreading. The significantly increased loss and threshold carrier density make stripe-geometry lasers lase at shorter

wavelengths where α becomes small in accordance with the previous results [Ara85, Oga84, Vah83].

Recently, Furuya [Fur85] pointed out theoretically that an effective α should be enhanced from an intrinsic α by weak index-guide and gain-guide in the lateral direction (CSP-type and stripe-geometry lasers), and almost the same as an intrinsic α in strong index-guide lasers. However, according to the reported experimental data, α is much smaller for CSP-type and stripe-geometry lasers than index-guide lasers [Osi87]. Comparing the experimental data to Furuya's analysis, it is found from Eq.(3.5) of Ref.[Fur85] that the intrinsic α should be strongly dependent on waveguide structure and very small for CSP-type and stripe-geometry lasers. Furthermore, for a small value of the intrinsic α , the effective α does not change much from the intrinsic value in the range of reasonable values of waveguide parameters. Therefore, the intrinsic α is indeed a dominant factor of the α dependence on waveguide structure, and it is hard to predict an actual α with Furuya's analysis without knowing an intrinsic value.

It has been reported that the experimental values of α distribute over some range depending on laser type and measurement method [Osi87]. Thus, rather than make a direct numerical comparison, it is informative to notice the geometry dependence of α . Little data showing the geometry dependence have been reported. Arakawa and Yariv [Ara85] presented the α dependence on laser length for BH (AlGa)As lasers with $L= 150$ and 300 μm . The experimental data are connected by a predicted curve of the α variation in Fig.4.4. Its variation is consistent with our calculation, and it is possible for us to estimate the active layer thickness used ($t = 0.15$ μm). Schimpe et al. [Sch84] reported $\alpha = 3 \pm 0.8$, which was measured in MCRW lasers with $L= 260 - 930$ μm and $t= 0.11$ μm . The experimental data are

marked by closed circles and connected in the same manner in Fig.4.4. Although a common α for all lasers was used in their calculations of FM noise, the standard deviation of α was 1.6, which corresponds to the variation of the calculated α for the same range of laser length.

The wavelength dependence of α is shown in Fig.4.6 with the AlAs mole fraction x as a parameter. The dashed lines represent the experimental dispersions of α which have been measured in active layers with the same AlAs mole fraction [Ara85, Hen81, Kir77, Str79, Str80]. The experimental and calculated dispersions of α show that α decreases gradually as wavelength approaches the bandgap. On the contrary, the prior calculations by Vahala et al. [Vah83] and Ogasawara et al. [Oga84] show that α increases very rapidly as photon energy decreases to the bandgap. This was due to the assumption of parabolic bands.

However, most of conventional diode lasers lase below and near the bandgap, and have relatively small α values of 2 - 6 [Hen80, Hen81, Man83, Str80, Str81, Str83]. Thus, the dispersions of α in Fig.4.6 are considered practical and dependable. According to the results of the above authors, the dispersion of α is also a function of injected carrier density, and the magnitude of α increases by ~ 0.7 as the carrier density increases from $1.8 - 2 \times 10^{18}$ to $2.5 - 3 \times 10^{18} \text{ cm}^{-3}$. This can explain the discrepancy between the experimental and the calculated dispersions of α in Fig.4.6. Since the absorption spectrum measured at a constant N_{th} has been used in our calculations, the calculated α should increase slightly with the increase of N_{th} , i.e., with the decrease of λ_L near the bandgap, and vice versa far from the bandgap.

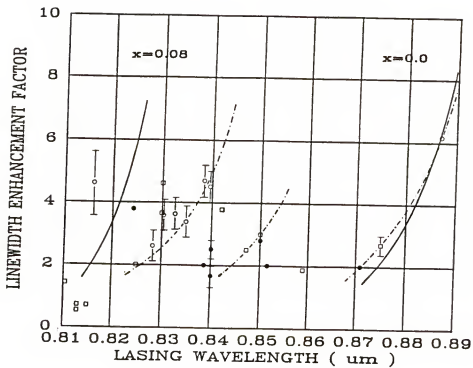


Figure 4.6 Calculated (solid lines) and experimental (dashed lines) dispersions of linewidth enhancement factor as a function of lasing wavelength. Experimental data are given in Table 4.2 with device parameters [Ara85, Har83, Hen81, Hen83, Kir77, Kik83, Kik85, Oga84, Sal83, Sch83, Str79, Str80, Str81, Tur79, Wel82].

4.3.3. Linewidth

The power-dependent term of the linewidth has been given by [Hen82]

$$\Delta f = \frac{v_g^2 h f_L n_{sp} \alpha_m (\alpha_m + \alpha_i)}{8\pi P_o} (1 + \alpha^2) \quad (4.12)$$

where v_g is the group velocity, n_{sp} is the spontaneous emission factor, α_m is the mirror loss, α_i is the internal waveguide loss, and P_o is the output power per facet. Lenth [Len84] has reduced the linewidth by applying a high reflectivity coating on one of the facets of an (AlGa)As laser. Arakawa and Yariv [Ara85] have suggested that Δf can be reduced by increasing facet reflectivity and laser length although α is increased due to the decrease of the lasing photon energy. This means that the threshold gain $(\alpha_m + \alpha_i)$ and the mirror loss α_m in Eq.(3.12) are dominant factors in determining the linewidth. However, the increase of L not only diminishes high speed performance of semiconductor lasers, but reduces packing density, and the application of high reflectivity coatings should accompany technological difficulties in integrated optical circuits. One possible method to avoid these kinds of adverse situations is to reduce the active layer thickness, achieving a substantial reduction of the linewidth as given in Fig.4.7. The linewidth has been calculated assuming that $v_g = c/4.33$, $n_{sp} = 2.3$, $P_o = 1\text{mW}$, and $\alpha_i = 20\text{ cm}^{-1}$; $h f_L$ and α are given in Figs.4.1 and 4.5, respectively. The change of active layer thickness has an effect only on α , neglecting small variations of v_g , $h f_L$ and n_{sp} , and the linewidth is proportional to $(1 + \alpha^2)$. Therefore, the linewidth reduces much faster than α as t decreases.

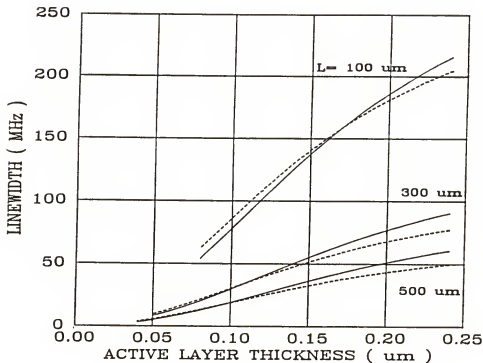


Figure 4.7 Predicted linewidth dependence on active layer thickness with laser length as a parameter. Parameters used for linewidth calculations; $V_g = c/4.33$, $n_{sp} = 2.3$, $P_0 = 1$ mW, $\alpha_i = 20$ cm^{-1} , $R_1 = R_2 = 0.31$, hf_L in Fig.4.1 and α in Fig.4.5. Solid lines for GaAs/AlGaAs lasers and dashed lines for (AlGa)As lasers with active layer of AlAs mole fraction, $x = 0.08$.

A significant reduction of α and the linewidth has been observed in QW (quantum well) lasers [Nod87, Oga85], mainly due to the enhancement of the differential gain dg/dN . Since the extreme case of a thin active layer is a QW structure, our suggestion for lowering α and the linewidth may have something to do with QW lasers. For both QW lasers and conventional DH lasers, dg/dN increases with the increase of photon energy and has the maximum value far above the lasing photon energy [Oga84, Oga85, Vah83].

QW lasers have a large magnitude of the density of states at the step-like conduction band edge, which leads to enhance dg/dN . As t decreases and the waveguide loss increases in conventional DH lasers, E_L moves up to a high photon energy above the parabolic conduction band edge and the density of states increases. Therefore, if E_L meets the photon energy where the density of states is large enough to supply the same order of dg/dN as in QW lasers, a significant reduction of α is also expected in conventional DH lasers. This can be well explained by Ogasawara's comparisons of dn/dN and dg/dN in QW lasers and a CSP laser [Oga85].

4.4. Conclusion

We have described a new calculation method for the dependence of the linewidth enhancement factor and the linewidth on laser geometry. Simple expressions of the absorption spectrum were suggested to calculate the gain change, the refractive index change, and the linewidth enhancement factor. The expressions were chosen to be integrable in the Kramers-Kronig dispersion relations so that analytical calculations for the linewidth enhancement factor as a function of laser geometry could be achieved.

As the active layer thickness and the laser length decrease, the lasing photon energy increases toward E_c , which is the limit of the calculation model. The gain change and the refractive index change also increase with an increase of the lasing photon energy. However, since the gain change increases much faster than the refractive index change, the linewidth enhancement factor decreases gradually. Results show that the linewidth enhancement factor reduces by a factor of 3 - 3.5 with the reduction of active layer thickness from 0.2 to 0.05 μm and by a factor of 2.4 with the reduction of laser length from 800 to 100 μm .

Lastly, we have speculated that the reduction of active layer thickness should be a very efficient method for achieving a significant reduction of the linewidth since it does not suffer a serious degradation of high-speed performance or technological difficulties which may be present with other linewidth reduction factors (laser length, high reflectivity coatings, and external cavities).

CHAPTER FIVE ANALYSIS AND OPTIMIZATION OF DH WAVEGUIDE PHASE MODULATOR

5.1. Introduction

The refractive index change in waveguide structures has very important applications for optical devices such as couplers, switches, and modulators [Alf82, Che88, Ino89, Kor87, Rei72]. These devices are essential for optical communication and high-speed signal processing. For optoelectronic integrated circuits (OEIC's), the refractive index change in III-V semiconductor waveguides has attracted special interest due to potential monolithic integration of the devices with other optical and electronic devices [Kor88, Sch89], close velocity matching between the optical wave and microwave for wide-bandwidth traveling-wave modulators [Wan87], and mature fabrication and processing techniques compatible with other semiconductor devices.

Semiconductor waveguide phase modulators are typical optical devices utilizing the refractive index change. Recent reports [Col87, Fai87a, Zuc88a] of very large phase shift efficiencies of the phase modulators have proven multi-gigahertz operations with a low drive voltage, reducing the length of the modulators to less than 500 μm . As a principal element of optical interferometric switches and/or couplers [Don85a, Don85b, Tak89b], phase modulators can also provide intensity modulation without suffering drawbacks which may occur in absorption modulators. Furthermore, in

terms of integration with a diode laser, the phase modulators should be a better counterpart than the absorption modulators since they utilize only a small change of the refractive index without an absorption change, ensuring a stable output from the diode laser.

The semiconductor phase modulators usually employ a p-n junction double heterostructure (DH) in order to inject or deplete free carriers from the junction and to guide light efficiently. Most of them are operated in the reverse bias condition rather than the forward bias condition because of the potential high-speed. By applying a reverse bias voltage, free carriers are depleted from the junction and electric field is developed across the depletion region. Consequently, the local refractive index changes and, hence, the phase of the propagating wave changes. It has been well known that the electro-optic and free carrier effects are involved in the refractive index change [Fai90, Men88]. The electro-optic effect includes the linear electro-optic (LEO) and quadratic electro-optic (QEO) effects. The free carrier effect includes the free carrier plasma (PL) and bandgap shift (BS) effects, where the BS effect is defined as a combination of the band-filling (BF) and bandgap shrinkage (BGS) effects. All these mechanisms have been introduced in section 3.3.

Recent research on the development of high-speed DH phase modulators has shown trade-off problems between phase shift efficiency and junction capacitance, which determines the speed of modulation. For example, highly-doped p-n junction DH phase modulators provide high phase shift efficiencies, but with large junction capacitances due to narrow depletion regions. P-i-N DH phase modulators, on the other hand, provide low junction capacitances, but with relatively small efficiencies. Here we propose and demonstrate a P-p-i-n-N DH structure for a high-performance

phase modulator by optimizing the phase shift efficiency and junction capacitance [Lee89b].

Fig.5.1 shows the P-p-i-n-N DH phase modulator, where the guiding region consists of p-i-n GaAs layers. A phase shift efficiency of $37.5 \text{ }^{\circ}/\text{V}\cdot\text{mm}$ at $\lambda = 1.3 \text{ } \mu\text{m}$ was obtained, which corresponds to the highest value reported for a P-n heterojunction GaAs/AlGaAs DH phase modulator [Alp87b]. By varying the intrinsic layer thickness and the carrier concentration, the P-p-i-n-N phase modulator can be a p-n homojunction DH phase modulator, or a P-i-N DH phase modulator. Therefore, a detailed analysis of the P-p-i-n-N phase modulator can not only provide performance comparisons of the three types of modulators but also facilitate optimization of DH phase modulators in terms of high-speed operation. In this chapter, we discuss the optimization of DH waveguide phase modulators by means of theoretical analysis and experiment.

A theoretical analysis for P-i-N junction electro-optic waveguide phase modulators, employing the LEO and free carrier effects by Marshall and Katz [Mar85] is already available. Recently, a theoretical analysis for P-n and p-n junction GaAs/AlGaAs phase modulators has been reported by Mendoza-Alvarez et al. [Men88], accounting for their experimental results successfully by including the electrorefraction and BF effect with the LEO and PL effects. Based on extensive experimental data, Faist and Reinhart [Fai90] have obtained semi-empirical equations for these effects. We present a detailed theoretical analysis of the P-p-i-n-N GaAs/AlGaAs phase modulator in section 5.2, which is used to optimize DH phase modulators and also extract physical parameters unknown to date by comparisons with experimental results. Device fabrication and phase shift measurement are described in section 5.3. Excellent agreement between experimental and

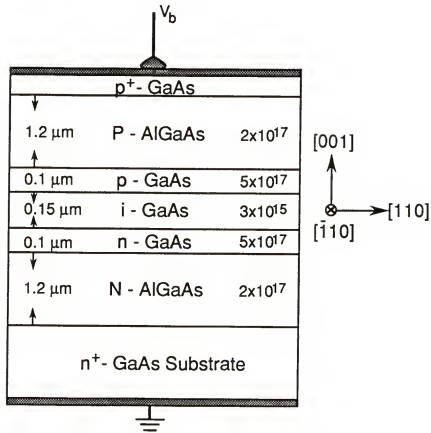


Figure 5.1 Schematic diagram of the P-p-i-n-N phase modulator. The guiding region consists of p-, n-, and intrinsic GaAs layers, which are designed to confine electric fields within them over the entire bias range. Incident light is guided by the double heterostructure.

theoretical results, which includes phase shift dependences on wavelength, carrier concentration, and intrinsic layer thickness, is presented in section 5.4. Based on our present work and previously reported results, we suggest design criteria of the DH phase modulators for high-speed operation.

5.2. Phase Shift in P-p-i-n-N Modulator

When a reverse bias voltage is applied to the P-p-i-n-N phase modulator along the [001] direction (Fig.5.1), the depletion region extends from its initially equilibrium position corresponding to $V_b = 0$ into neighboring neutral regions, removing free carriers and developing a higher electric field as shown in Fig.5.2. Then, the local refractive index in the depletion region experiences changes due to the free carrier and electro-optic effects discussed in chapter three. As a result, the phase of the optical mode propagating along the waveguide is affected, and the magnitude of the phase shift will depend on the effective portion of optical power occupied by the extended depletion region and the associated increase in the electric field. Therefore, for the calculation of the phase shift, it is necessary to estimate 1) the distribution of the depletion region, 2) the electric field distribution, and 3) the optical field distribution of the propagating mode and its overlap with the modulating field in the depletion region.

5.2.1. Depletion Region and Electric Field

Since the P-p-i-n-N phase modulator has been designed to utilize the QEO and BS effects in GaAs which is hardly used in P-i-N phase

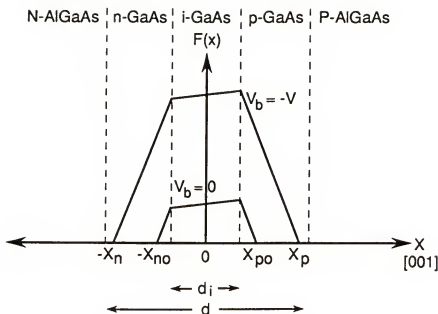


Figure 5.2 Depletion region and electric field distributions with and without reverse bias voltage in the P-p-i-n-N structure. As the reverse bias voltage is applied, the depletion region extends into adjacent neutral region by removing free carriers, and the electric field increases within the depletion region. The intrinsic layer thickness is d_i and the p-i-n GaAs guiding thickness is d .

modulators, the depletion region is usually confined within the p-i-n GaAs active region over the entire bias condition. However, depending on the thickness and doping concentration of the GaAs active layers and the reverse bias voltage, the depletion region may extend into the AlGaAs cladding layers. For the sake of simplicity, we will consider both the cases here; (i) when the depletion region remains in the p-i-n GaAs guiding region, and (ii) the p-i-n GaAs guiding region is entirely depleted and the depletion edges are in the AlGaAs cladding layers. It is assumed that the layers are doped uniformly and the intrinsic GaAs layer is slightly n-type doped. (See Fig.5.2). The p-i and n-i homojunctions are located at $x = \pm d_i/2$, where d_i is the thickness of the intrinsic GaAs layer. The P-p and N-n heterojunctions are located at $x = \pm d/2$, where d is the total thickness of the GaAs guiding layers.

If we solve the Poisson's equation for the 3-layer case by using the depletion approximation and applying four boundary conditions at the p-i and n-i homojunctions, and the depletion edges, the depletion width can be obtained as follows;

$$x_n \cdot \frac{d_i}{2} = \frac{-d_i \left(1 + \frac{N_i}{N_a} \right) + \sqrt{d_i^2 \left(1 + \frac{N_i}{N_a} \right) \left(1 + \frac{N_i}{N_a} \right) + \frac{2\epsilon_1}{q} \left(\frac{1}{N_a} + \frac{1}{N_d} \right) (V_0 - V_b)}}{\left(1 + \frac{N_d}{N_a} \right)}$$

$$x_p \cdot \frac{d_i}{2} = \frac{N_i d_i + N_d \left(x_n \cdot \frac{d_i}{2} \right)}{N_a} \quad (5.1)$$

where ϵ_1 is the GaAs permittivity, V_0 is the built-in potential, V_b is the reverse bias voltage, and N_i , N_a , and N_d are the doping concentrations of the intrinsic, p-type, and n-type GaAs layers, respectively. The built-in

potential can be easily obtained from a simple energy band diagram of the p-i-n structure: $qV_0 = E_g - \Delta E_{Fn} - \Delta E_{Fp}$ where E_g is the GaAs bandgap energy, ΔE_{Fn} is the energy difference between the conduction band edge and the Fermi level of the n-GaAs layer, and ΔE_{Fp} is the energy difference between the Fermi level and the valence band edge of the p-GaAs layer. The corresponding electric field is given by

$$\begin{aligned}
 F(V_b, x) &= \frac{q N_d}{\epsilon_1} (x + x_n), & -x_n \leq x \leq -\frac{d_i}{2} \\
 &= \frac{q N_1}{\epsilon_1} \left(x + \frac{d_i}{2} \right) + \frac{q N_d}{\epsilon_1} \left(x_n - \frac{d_i}{2} \right), & -\frac{d_i}{2} \leq x \leq \frac{d_i}{2} \\
 &= -\frac{q N_a}{\epsilon_1} (x - x_p), & \frac{d_i}{2} \leq x \leq x_p
 \end{aligned} \tag{5.2}$$

Note that we have not considered the internal electric fields located at the N-n and P-p isotype heterojunctions, which are formed by accumulating the majority carriers on one side of the isotype heterojunctions and providing the same amount of ionized dopants on the other side. However, since the reverse bias voltage is applied mostly across the p-i-n GaAs layers, it hardly affects the internal fields at the heterojunctions; the electric field expressed by Eq.(5.2) is, therefore, sufficient to calculate phase shift contributions from the electro-optic effects as long as the depletion region stays within the p-i-n GaAs layers.

As the reverse bias voltage increases, the depletion edge will meet the internal electric field described above. For the doping concentrations (1×10^{16} $\sim 1 \times 10^{18} \text{ cm}^{-3}$) of interest to us, the internal electric fields have the same direction as the external electric field in the p-i-n GaAs layers. The

majority carriers are accumulated on the GaAs side and the ionized dopants are distributed on the AlGaAs side. According to results of PISCES simulation [Pin85], the external electric field expels the accumulated charges with a further increase of the reverse bias voltage, extending into the AlGaAs cladding layers. The required bias voltage to eliminate the internal electric field should correspond to the built-in potential of the isotype heterojunction. Therefore, the same method used in the 3-layer case can be applied to the 5-layer case by including the effect of the built-in potentials.

From six boundary conditions at the p-i and n-i homojunctions, the N-n and P-p heterojunctions, and the depletion edges, we obtain a quadratic equation for the depletion width. The equation is rather complicated although it can be solved analytically. Assuming useful conditions such that the doping concentrations in the n- and p-type GaAs are the same ($N=N_d=N_a$) and the intrinsic layer is doped slightly ($N_i \ll N$), the depletion width is approximated by

$$x_n \cdot \frac{d}{2} = \frac{-\left(\frac{\epsilon_2 d}{\epsilon_1} + \frac{N_i d_i}{N_A}\right) + \sqrt{\left(\frac{\epsilon_2 d}{\epsilon_1} + \frac{N_i d_i}{N_A}\right)^2 + \frac{\epsilon_2}{\epsilon_1} \left(\frac{1}{N_A} + \frac{1}{N_D}\right) \left[\frac{2\epsilon_1 (V_0' - V_b)}{q} \cdot N_i d_i^2 \cdot \frac{N(d^2 - d_i^2)}{2}\right]}}{\left(1 + \frac{N_D}{N_A}\right)} \quad (5.3)$$

$$x_p \cdot \frac{d}{2} = \frac{N_i d_i + N_D (x_n \cdot \frac{d}{2})}{N_A} \quad (5.3)$$

where ϵ_2 is the AlGaAs permittivity, and N_A and N_D are the doping concentrations of the P- and N-AlGaAs layers, respectively. $V_0' = V_0 - V_{DP} - V_{DN}$ where V_{DP} and V_{DN} are the built-in potentials of the P-p and N-n heterojunctions [Cas78]: $qV_{DP} = \Delta E_v + \Delta E_{FP} - \Delta E_{FP}$ where ΔE_v is the valence

band discontinuity, ΔE_{Fp} and ΔE_{Fn} are the energy differences between the Fermi level and the valence band edge in the p-type GaAs and AlGaAs layers, respectively: $qV_{DN} = \Delta E_c + \Delta E_{Fn} - \Delta E_{Fn}$ where ΔE_c is the conduction band discontinuity, ΔE_{Fn} and ΔE_{Fn} are the energy differences between the conduction band edge and the Fermi level of the n-type GaAs and AlGaAs layers, respectively. The corresponding electric field is given by

$$\begin{aligned}
 F(V_b, x) &= \frac{q N_D}{\epsilon_2} (x + x_n), & -x_n \leq x \leq -\frac{d}{2} \\
 &= \frac{q N}{\epsilon_1} \left(x + \frac{d}{2} \right) + \frac{q N_D}{\epsilon_1} \left(x_n - \frac{d}{2} \right), & -\frac{d}{2} \leq x \leq -\frac{d_i}{2} \\
 &= \frac{q N_i}{\epsilon_1} \left(x - \frac{d_i}{2} \right) + \frac{q N}{\epsilon_1} \left(\frac{d}{2} - \frac{d_i}{2} \right) + \frac{q N_D}{\epsilon_1} \left(x_n - \frac{d}{2} \right), & -\frac{d_i}{2} \leq x \leq \frac{d_i}{2} \\
 &= -\frac{q N}{\epsilon_1} \left(x - \frac{d}{2} \right) + \frac{q N_A}{\epsilon_1} \left(x_p - \frac{d}{2} \right), & \frac{d_i}{2} \leq x \leq \frac{d}{2} \\
 &= -\frac{q N_A}{\epsilon_2} (x - x_p), & \frac{d}{2} \leq x \leq x_p
 \end{aligned} \tag{5.4}$$

It is found from Eq.(5.4) that there are electric field discontinuities at the P-p and N-n heterojunctions due to the different permittivities of the GaAs and AlGaAs. The electric field at $\pm d/2$ is larger in the AlGaAs layer than the GaAs layer by a ratio of ϵ_1/ϵ_2 .

5.2.2. Optical Field

The free carrier effects, field induced electro-optic effects and the associated index change vary along the transverse (x) direction as a

function of the reverse bias voltage. Therefore, it is sufficient to consider the one dimensional solution to the optical modal field. Practical devices employ thick cladding layers to prevent the free carrier absorption loss in the contact layer and the substrate and a thin GaAs active region to support only the fundamental transverse mode. Thus, optically, the structure can be considered as a 3-layer slab waveguide. The optical field, described by a cosine function in the guiding region and exponentially decaying functions in the cladding layers can be determined, provided the refractive indices of the GaAs and AlGaAs are known at the operating wavelength.

In section 2.3, we discussed a semi-empirical equation (Eq.(2.8)) for the refractive index dispersion in GaAs and AlGaAs, developed by Afromowitz [Afr74]. Eq.(2.8) showed an excellent agreement with experimental refractive indices [Cas74] near the GaAs bandgap energy, and can be simplified above $\lambda = 1.05 \mu\text{m}$ to the following equation:

$$n^2(E, x) - 1 = \frac{E_o(x) E_d(x)}{E_o(x)^2 - E^2} \quad (5.5)$$

where $E_o(x) = 3.65 + 0.871x + 0.179x^2$

$$E_d(x) = 36.1 - 2.45x$$

E is the photon energy, $E_o(x)$ and $E_d(x)$ are the position and the strength of a modified single-oscillator for representing the absorption spectrum, and x is the AlAs mole fraction in $\text{Al}_x\text{Ga}_{1-x}\text{As}$.

5.2.3. Phase shift of Propagating Mode

For the optical mode propagating along a planar (1-D) waveguide in which the refractive index changes, the variation of the effective refractive index is expressed by a first-order perturbation theory [Hau84] as follows;

$$\Delta n_{\text{eff}} = \frac{1}{n_{\text{eff}}} \int_{-\infty}^{\infty} n(x) \Delta n(x) \psi^2(x) dx \quad (5.6)$$

where n_{eff} is the effective refractive index of the propagating mode, $n(x)$ is the refractive index in the waveguide, $\Delta n(x)$ is the refractive index change, and $\psi(x)$ is the normalized optical field. whose total power is one (i.e., integration of $\psi^2(x)$ from minus infinity to infinity corresponds to one). The refractive index varies along the x -direction in the P-p-i-n-N phase modulator under the bias condition, and $\Delta n(x)$ in a reverse biased junction is very small compared to $n(x)$. Since the refractive index change occurs primarily in the guiding layer, $n(x)/n_{\text{eff}} \approx 1$. Therefore, Eq.(5.6) can be reduced to a one-dimensional integration, and the phase shift is approximated by

$$\Delta\phi = \frac{2\pi L}{\lambda} \int_{-\infty}^{\infty} \Delta n(x) \psi^2(x) dx \quad (5.7)$$

where L is the waveguide length and λ is the wavelength. Since $\Delta n(x)$ consists of the contributions from the PL, BS, LEO, and QEO effects, it is more convenient to decompose Eq.(5.7) into individual phase shifts due to the corresponding effects.

As mentioned earlier (Fig.5.2), the depletion region at equilibrium ($V_b=0$) has its depletion edges at x_{p0} and $-x_{n0}$. In the presence of the reverse bias voltage, the edges move to x_p and $-x_n$, extending the depletion region. Therefore, for an applied bias voltage V_b , the phase shift due to the PL effect is represented by

$$\Delta\phi_{PL} = \frac{2\pi L}{\lambda} \left[\int_{-x_n}^{x_p} \Delta n_{PL}(x) \psi^2(x) dx - \int_{-x_{n0}}^{x_{p0}} \Delta n_{PL}(x) \psi^2(x) dx \right] \quad (5.8)$$

where $\Delta n_{PL}(x)$ is the refractive index change due to the PL effect in the depletion region, which has been discussed in section 3.2 for the carrier injection case, and hence is expressed by Eqs.(3.2) and (3.3) without the minus signs. Since Δn_{PL} depends on the carrier concentration, dopant type, and AlAs mole fraction, Eq.(5.8) should be further partitioned into the same number of integrals as the depleted layers, and each integral can be expressed as Δn_{PL} times the optical power confined in that region.

Following the same procedure, the phase shift due to the BS effect is derived from Eqs.(3.4) and (5.7) and represented as follows:

$$\Delta\phi_{BS} = \frac{2\pi L}{\lambda} \left[\int_{-x_n}^{x_p} B(x) N(x) \psi^2(x) dx - \int_{-x_{n0}}^{x_{p0}} B(x) N(x) \psi^2(x) dx \right] \quad (5.9)$$

The BS coefficient depends on the dopant type and AlAs mole fraction. Since we assumed the depletion approximation and uniform doping in the doped layers, $B(x)$ and $N(x)$ are constant in each depletion layer. Then, B and N can be taken out of the bracket in Eq.(5.9), reducing the integrals to a change of the optical confinement in that depletion layer for the applied bias voltage.

The phase shift due to the LEO effect can be represented from Eqs.(3.7) and (5.7) as follows:

$$\Delta\phi_{\text{LEO}} = \pm \frac{\pi n^3 L}{\lambda} r_{41} \int_{-L}^{0} [F(V_b, x) - F(0, x)] \psi^2(x) dx \quad (5.10)$$

where $F(V_b, x)$ is the electric field for the reverse bias voltage V_b and is a function of position even in the same depleted layer as seen by Eqs.(5.2) and (5.4). As discussed in section 3.3, the plus and minus signs are associated with the $[\bar{1}10]$ and $[110]$ propagation directions, respectively. Since the electric field goes to zero outside the depletion region, Eq.(5.10) is reduced to an integration in the depletion region.

Finally, the phase shift due to the QEO effect is represented from Eqs.(3.8) and (5.7) as follows:

$$\Delta\phi_{\text{QEO}} = \frac{\pi n^3 L}{\lambda} R \int_{-L}^{0} [F^2(V_b, x) - F^2(0, x)] \psi^2(x) dx \quad (5.11)$$

Now, we consider the total phase shift due to the PL, BS, LEO, and QEO effects. For TE modes propagating along the $[\bar{1}10]$ and $[110]$ directions, the total phase shift is obtained as a sum of the individual effects:

$$\Delta\phi_{\text{TE}} = \Delta\phi_{\text{PL}} + \Delta\phi_{\text{BS}} + \Delta\phi_{\text{LEO}} + \Delta\phi_{\text{QEO}} \quad (5.12)$$

As discussed in chapter three, the PL, BF, and QEO contributions have the same sign regardless of the propagation direction and polarization. The LEO contribution adds to the other terms for the $[\bar{1}10]$ propagation direction

and subtracts for the [110] propagation direction. For TM modes, the total phase shift will be

$$\Delta\phi_{\text{TM}} = \Delta\phi_{\text{PL}} + \Delta\phi_{\text{BS}} + \Delta\phi_{\text{QEO}} \quad (5.13)$$

since there is no contribution from the LEO effect for TM modes.

5.3. Fabrication and Characterization

The PpinN structure shown in Fig.5.1 was grown on a (001) oriented Si-doped GaAs substrate by metal-organic chemical vapor deposition (MOCVD) at the Boeing High Technology Center. A 1.2 μm thick N-Al_{0.38}Ga_{0.62}As ($N_D=2\times10^{17}\text{cm}^{-3}$) cladding layer was grown first, followed by n-i-p GaAs guiding layers of a total thickness of 0.35 μm . The GaAs guiding region consisted of a 0.1 μm thick n-GaAs ($N_d=5\times10^{17}\text{cm}^{-3}$), a 0.15 μm i-GaAs (unintentionally n-type doped $N_i=3\times10^{15}\text{cm}^{-3}$) and a 0.1 μm p-GaAs ($N_a=5\times10^{17}\text{cm}^{-3}$) layer. A 1.2 μm thick P-Al_{0.38}Ga_{0.62}As ($N_A=2\times10^{17}\text{cm}^{-3}$) cladding layer was grown followed by a p⁺-GaAs contact layer. Ohmic contacts were formed by evaporating Cr/Au-Zn/Au on the top side for a p-type ohmic contact and Au-Ge/Ni/Au on the bottom side for an n-type contact, followed by thermal annealing at 450 °C for 2 minutes in H₂-N₂ (5-95 %) forming gas ambient. Prior to metal evaporation for the n-type contact, the sample was lapped down to approximately 4 mils to obtain mirror-like facets after cleaving. Breakdown voltages were between -5.5 and -6.5 V.

Phase shift measurements were performed on three samples with different waveguide lengths, viz., L= 630, 755, and 1730 μm , by using a

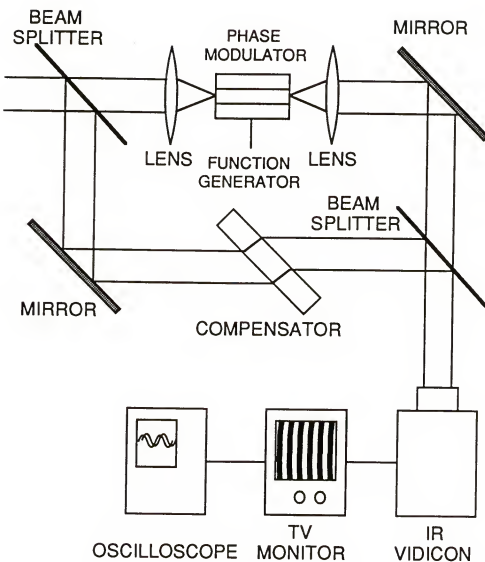


Figure 5.3 Mach-Zehnder interferometer used in phase shift experiment. Interference fringes are formed by two beams passing through the reference and waveguide arms.

Mach-Zehnder interferometer as shown in Fig.5.3. A 1.06 μm Nd-Yag laser or a 1.3 μm InGaAs laser diode was end-fire coupled onto the [110] facet of the waveguide phase modulator using a microscope objective. The polarization of the incident light was controlled prior to the first beam splitter of the interferometer so that either TE_0 or TM_0 mode can be excited. Interference fringe patterns were obtained by aligning the two optical beams propagating through the reference arm and the waveguide arm in the Mach-Zehnder interferometer. By adjusting the optical path difference and intensities of the optical beams, excellent intensity contrast (defined as $(I_{\max}-I_{\min})/(I_{\max}+I_{\min})$ where I_{\max} and I_{\min} indicate the maximum and minimum intensities of the interference fringe, respectively) of the order of 60 to 70 % in the interference fringe pattern was easily obtained (Fig.5.4a). Application of reverse bias voltage causes the fringe pattern to shift laterally due to the phase change experienced by the optical mode of the waveguide phase modulator. Fig.5.4b shows the shifts of the interference patterns of the TE_0 mode in a sample with $L= 630 \mu\text{m}$ as the reverse bias voltage is increased from 0 to 5V in a 1 V step.

5.4. Result and Discussion

Following the procedures outlined in section 5.2, theoretical estimation of the phase change has been performed for the P-p-i-N phase modulator using the waveguide parameters specified in section 5.3. Physical parameters of $\text{Al}_x\text{Ga}_{1-x}\text{As}$ [Ada85, Joy78] used in our calculations of the depletion width and electric field are shown in Table 5.1. The subscripts Γ , X , and L indicate the direct and indirect conduction bands, and V indicates the valence band represented by a combined effective mass

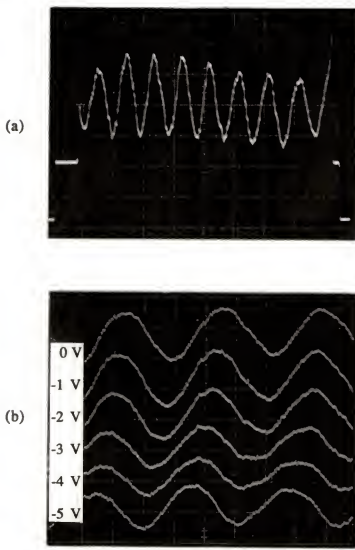


Figure 5.4 Observed interference fringe patterns. (a) Typical fringe patterns used in phase shift measurements with excellent intensity contrasts of 60 - 70 percent. (b) Shift of fringe patterns for $V_b = 0$ to $-5V$ with a 1V step. Due to changes of the local refractive index in the waveguide, the phase of a propagating mode changes, shifting interference fringes. The distance between consecutive peaks corresponds to 2π .

Table 5.1 Physical parameters of $\text{Al}_x\text{Ga}_{1-x}\text{As}$ used in theoretical calculations [Ada85, Joy78]

Dielectric constant	$\epsilon_r(x) = 13.18 - 3.12x$
Effective density of density	$N_j = 2.51 \times 10^{19} \left(\frac{m_j}{m_o} \right)^{2/3} \left(\frac{300}{T} \right)^{2/3}, \quad j = \Gamma, L, X, V$
Effective mass	$m_\Gamma = (0.067 + 0.083x) m_o$ $m_L = (0.55 + 0.12x) m_o$ $m_X = (0.85 - 0.07x) m_o$ $m_V = (0.48 + 0.31x) m_o$
Bandgap energy	$E_\Gamma = 1.424 + 1.247x, \quad 0 \leq x \leq 0.45$ $E_L = 1.708 + 0.642x$ $E_X = 1.900 + 0.125x + 0.143x^2$
Bandgap discontinuity	$\Delta E_c : \Delta E_v = 0.6 : 0.4$
Electron and hole Fermi energy	$E_c - E_F = -kT \left[\ln \left(\frac{N}{N_{c1}} \right) + 0.35355 \left(\frac{N}{N_{c1}} \right) \left(\frac{N_{c2}}{N_{c1}} \right) \right]$ $E_F - E_V = -kT \left[\ln \left(\frac{P}{N_V} \right) + 0.35355 \left(\frac{P}{N_V} \right) - 4.95 \times 10^{-3} \left(\frac{P}{N_V} \right)^2 \right]$ $N_{ci} = N_\Gamma + N_L \exp \left[-\frac{i(E_L - E_\Gamma)}{kT} \right] + N_X \exp \left[-\frac{i(E_X - E_\Gamma)}{kT} \right]$ $i = 1, 2$

of the heavy-hole and light-hole effective masses. The Fermi energy represents the energy difference between the conduction band edge and the Fermi level in n-type $\text{Al}_x\text{Ga}_{1-x}\text{As}$, or the energy difference between the Fermi level and the valence band edge in p-type $\text{Al}_x\text{Ga}_{1-x}\text{As}$. Energy and carrier concentration in Table 5.1 are in units of eV and cm^{-3} , respectively.

The P-p-i-n-N waveguide structure, used for our study, consists of a $0.35\text{ }\mu\text{m}$ thick GaAs guiding region with a p- and an n-type $\text{Al}_{0.38}\text{Ga}_{0.62}\text{As}$ cladding layers on each side. The waveguide supports only the fundamental transverse mode over the wavelength region of interest, i.e., the TE_0 or TM_0 mode depending on the polarization of incident light. The guided mode can then be described by a cosine function in the GaAs guiding region and an exponentially decaying function in the AlGaAs cladding layers. In addition, the modal field has been normalized so that a definite integral of the modal field within a specified region is the confinement factor of optical power in that region.

As discussed in chapter three, we assume that the intersubband transitions are negligible in the N-AlGaAs cladding layer and the expression Eq.(3.3) for p-GaAs is applicable to the P-AlGaAs cladding layer. The BS coefficient for the AlGaAs layers was obtained by shifting those of GaAs to the AlGaAs bandgap energy. These approximations may cause a small error for calculations of the PL and BS effects in the AlGaAs layers. However, those contributions are less important in our theoretical results because the depletion region stays within the GaAs guiding region for the most part and the optical intensity in the AlGaAs cladding layers is indeed very small. Since the LEO contribution can be obtained from experimental phase shifts for the TE_0 and TM_0 modes, the linear electro-optic coefficient can be deduced and compared with other published results in the

wavelength region of interest. The only fitting parameter in the theoretical calculations is the QEO coefficient R , which is estimated by comparing the theoretical and experimental results.

5.4.1. Comparisons of Theory and Experiment

The theoretical phase shifts for the TE_0 and TM_0 modes at $\lambda = 1.06$ and $1.3 \mu\text{m}$ are shown in Figs.5.5a and 5.5b, respectively, as a function of the reverse bias voltage. These figures also show individual contributions from the PL, BS, LEO and QEO effects. The total phase shift for the TE_0 mode appears to increase almost linearly with the reverse bias voltage. This can be understood in a qualitative manner as follows: The depletion width ($x_n + x_p$) and the electric field F exhibit a $V_b^{1/2}$ dependence as seen in Eqs.(5.1) and (5.2). The PL and BS contributions in Eqs.(5.8) and (5.9) are proportional to both ($x_n + x_p$) and the non-uniform modal field across the depletion region, so the contributions are a sublinear function of V_b . The LEO contribution in Eq.(5.10) is approximately proportional to $(x_n + x_p) \cdot F$ and hence it varies linearly with V_b . The QEO contribution in Eq.(5.11) becomes superlinear following similar reasoning. Thus, the combined contribution from the PL, BS, and QEO effects appears to vary linearly with V_b when the individual contributions have comparable magnitudes. However, as the QEO effect becomes significant with the wavelength approaching the bandgap, the total phase shift shows a superlinear dependence as is the case for the TM_0 phase shift at $\lambda = 1.06 \mu\text{m}$ and observed in most of quantum-well modulators [Wei87, Zuc88a].

Measured phase shifts are also shown in Fig.5.5 as closed circles for the TE_0 mode and open squares for the TM_0 mode with excellent

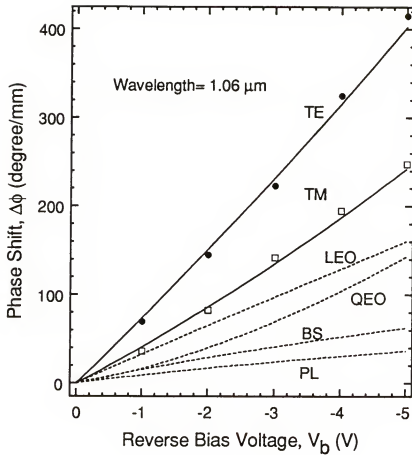


Figure 5.5 Experimental and theoretical phase shifts as a function of reverse bias voltage. The total phase shift for the TE_0 mode (TE) is obtained by summing up individual contributions from the LEO, QEO, BS, and PL effects. For the TM₀ mode, it is obtained as a sum of the QEO, BS, and PL contributions.

(a) Phase shifts at $\lambda = 1.06 \mu\text{m}$ with significantly enhanced QEO contributions.

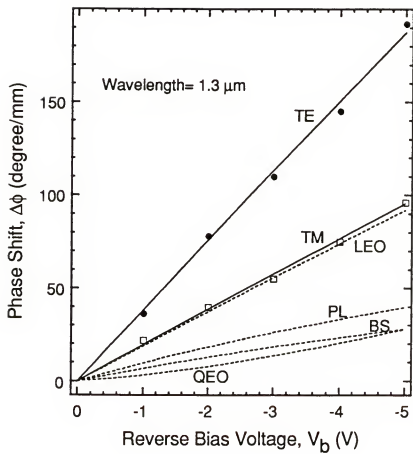


Figure 5.5 Continued.

(b) Phase shifts at $\lambda=1.3 \mu\text{m}$ with dominant LEO contributions.

agreements at both wavelengths with the theory. The LEO effect is only dominant effect at $\lambda=1.3\text{ }\mu\text{m}$ as is the case with conventional semiconductor phase modulators, but not necessarily so at $\lambda=1.06\text{ }\mu\text{m}$. The phase shift efficiency is estimated to be 82 and $37.5\text{ }^{\circ}\text{V}\cdot\text{mm}$ for the TE_0 mode at $\lambda=1.06$ and $1.3\text{ }\mu\text{m}$, respectively. These values are close to the reported highest efficiencies at the same wavelengths for p-n homojunction and P-n heterojunction GaAs/AlGaAs phase modulators [Alp87b, Men88].

The significant improvement of the phase shift efficiency of the P-p-i-n-N modulators at $\lambda=1.06\text{ }\mu\text{m}$ is mainly due to the dramatic increase in the QEO contribution (Fig.5.5a) while the LEO and BS effects were the two major contributions for the highest reported efficiencies in the other two cases [Al87a, Me88]. For example, the LEO and BS effects accounted for 70 % of the phase shift efficiency and the QEO effect for only 18 % in the p-n homojunction modulators. On the other hand, in our devices, the QEO contribution is 35 % and the LEO contribution is 39 % at $V_b=-5\text{ V}$.

Thus, the P-p-i-n-N modulator operates like a P-i-N phase modulator, obtaining most of the phase shift from the electro-optic effects. It should be noted that the LEO effect is the only dominant factor in the P-i-N phase modulators and it is hard to achieve a high phase shift efficiency solely by using the LEO effect. Therefore, the electric field was increased by reducing the intrinsic layer thickness in order to utilize the QEO effect with its wavelength dependence (section 3.3). In addition, the depletion region was confined within the GaAs guiding region including the p- and n-GaAs buffer layers, thus utilizing higher QEO and BS effects in GaAs rather than those in AlGaAs. As a result, a high phase shift of $82\text{ }^{\circ}\text{V}\cdot\text{mm}$ could be achieved, yet maintaining advantages of the P-i-N phase modulators such as low junction and dynamic capacitances, relatively low absorption loss,

and negligible intensity modulation. These characteristics as well as high phase shift efficiency are very important for high speed operations of the phase modulators.

The LEO contribution can be extracted from measured phase shift difference between the TE_0 and TM_0 modes. The LEO coefficient was estimated to be $1.8 \times 10^{-10} \text{ cm/V}$ at $\lambda = 1.06 \mu\text{m}$ and $1.6 \times 10^{-10} \text{ cm/V}$ at $\lambda = 1.3 \mu\text{m}$, showing its dispersive nature near the bandgap. The r_{41} values are slightly larger than those reported by Faist and Reinhart [Fai90]. From the experimental results, the QEO coefficient R has been estimated to be $4.3(\pm 0.5) \times 10^{-16}$ and $1.3(\pm 0.5) \times 10^{-16} \text{ cm}^2/\text{V}^2$ at $\lambda = 1.06$ and $1.3 \mu\text{m}$, respectively. These values are given as closed circles in Fig.5.6 with other reported data. Faist and Reinhart [Fai90] have reported experimental values of R at wavelengths of 1.09 and $1.15 \mu\text{m}$, shown as open squares. Mendoza-Alvarez et al. [Men88] have also reported a theoretical dispersion for the QEO coefficient ($R \sim \exp(3/\lambda^3)$), plotted as a solid line. The dashed line has been drawn to fit the experimental data at $\lambda = 1.06$ and $1.3 \mu\text{m}$ by using the theoretical dispersion with different magnitude. It shows a good agreement with the experimental value. Our data show an increase of $20 - 25 \%$ over those reported by Faist and Reinhart and a factor of 2 larger than the theoretical values reported by Mendoza-Alvarez et al. An apparent polarization dependence of the QEO coefficient seen by Faist and Reinhart was not observed.

The free carrier effects are responsible for only a small portion of the total phase shift despite the high doping concentration of $5 \times 10^{17} \text{ cm}^{-3}$ in the p- and n-GaAs layers. This is due to a small variation of the depletion width or the depletion confinement factor, defined as the optical power fraction confined in the depletion region:

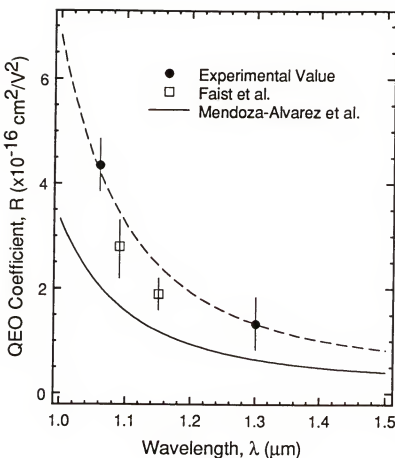


Figure 5.6 Wavelength dependence of the quadratic electro-optic (QEO) coefficient near the GaAs bandgap. The QEO coefficients measured experimentally in this work (closed circles), by Faist and Reinhart [Fai90] (open circles), and analysis of Mendoza-Alvarez et al. [Men88] (solid line) are shown. The QEO coefficient evaluated at $\lambda = 1.06$ and $1.3 \mu\text{m}$ by comparing the theory and experiment (Fig.5.5) show the same variation of R as the theoretical dispersion($\sim \exp(3/\lambda^3)$).

$$\Gamma_d(V_b) = \int_{x_n}^{x_p} \psi^2(x) dx \quad (5.14)$$

Fig.5.7 shows variations of the depletion width and the depletion confinement factor for reverse bias voltage changes from $V_b = 0$ to $-5V$.

The $0.15 \mu m$ thick intrinsic GaAs layer has already been depleted at $V_b=0$. With the application of reverse bias V_b , significant part of V_b and the electric field are found across the layer with the adjacent p- and n-GaAs layers becoming depleted due to the rest of the bias voltage. The depletion width increases only 40 % as Γ_d increases from 0.45 to 0.6 at $\lambda=1.06 \mu m$. Considering the depletion width change of 100 % and Γ_d change of 0.25 for the high-efficiency p-n homojunction phase modulator [Men88] for the same V_b range, these variations are so small that the PL and BS phase shifts contribute only 50 % as much as in the p-n homojunction modulator. However, the large value of Γ_d and little variation with V_b in the P-p-i-n-N phase modulator means low junction and dynamic capacitances necessary for high-speed operation.

5.4.2. Wavelength Dependence

The phase shift increases by a factor of 2.2 for the TE_0 mode and a factor of 2.6 for the TM_0 mode as the wavelength is decreased from 1.3 to $1.06 \mu m$. These variations can be understood in terms of the four effects and their wavelength dependences as is shown in Fig.5.8 for $V_b = -5V$. We have chosen a wavelength region of $1.0 - 1.5 \mu m$ since λ less than $1.0 \mu m$ is not useful for GaAs/AlGaAs phase modulators due to large absorption loss and

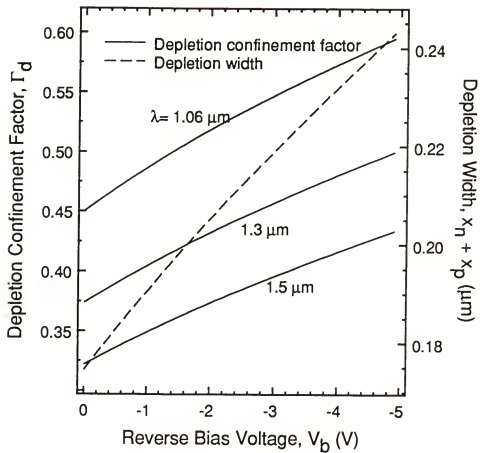


Figure 5.7 Reverse bias voltage dependence of the depletion confinement factor and depletion width with wavelength as a parameter. Γ_d increases with decreasing wavelength, and the change in Γ_d with bias voltage is larger for shorter wavelength.

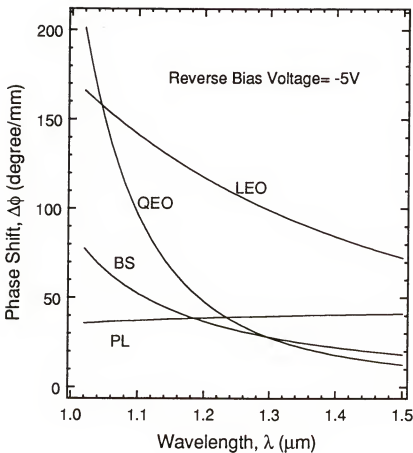


Figure 5.8 Wavelength dependence of individual phase shifts from the LEO, QEO, BS, and PL effects at $V_b = -5V$. A significant increase in the QEO effect is seen as the wavelength approaches the GaAs bandgap. The increase in the LEO effect is mainly due to the increase of Γ_d (Fig.5.7). The free carrier (BS and PL) effects show limited contributions due to a small change of Γ_d for the bias range.

intensity modulation. Both the electro-optic and BS contributions increase with decreasing wavelength while the PL contribution barely decreases. These variations can be understood by analyzing wavelength dependent terms in the corresponding phase shift equations (Eqs.(5.8) - (5.11)).

First, for the PL effect, $\Delta\phi_{PL} \sim 1/\lambda \cdot \Delta n_{PL} \cdot \Delta\Gamma_d$. There is an inherent $1/\lambda$ dependence between the phase shift and the refractive index change as shown in Eq.(5.7). $\Delta n_{PL} \sim \lambda^2$ from Eqs.(3.2) and (3.3). $\Delta\Gamma_d$ is the change of Γ_d as V_b increases from 0 to -5V; it is slightly larger at lower wavelengths (Fig.5.7), $\Delta\Gamma_d \sim 1/\lambda$. Therefore, $\Delta\phi_{PL}$ remains unchanged over the wavelength range. The BS contribution increases by a factor of 2.2 for the wavelength change of 1.3 to 1.06 μm . This is mainly due to an increase of the BS coefficient $B(\lambda)$. $\Delta\phi_{BS} \sim 1/\lambda \cdot B(\lambda) \cdot \Delta\Gamma_d$. $B(\lambda)$ is 1.6 times larger at 1.06 μm according to Eq.(3.4). Again, $\Delta\Gamma_d \sim 1/\lambda$. Then, a simple calculation shows that the ratio $\Delta\phi_{BS}(1.06\mu\text{m})/\Delta\phi_{BS}(1.3\mu\text{m})$ is around 2.4. Despite a large increase of the BS coefficient at shorter wavelengths, the BS contribution is small due to a small variation of Γ_d .

The LEO effect provides the large phase shifts over the entire wavelength region because of the excellent overlap between the electric and optical fields. Looking at wavelength dependent terms in Eq.(5.10), $\Delta\phi_{LEO} \sim n^3/\lambda \cdot \Gamma_d$. A refractive index change of ~ 0.1 is estimated for $\lambda = 1.0$ to $1.5 \mu\text{m}$ from Eq.(5.5), and hence n can be considered almost constant. Γ_d is approximately proportional to $1/\lambda$. Therefore, $\Delta\phi_{LEO} \sim 1/\lambda^2$. The ratio of $\Delta\phi_{LEO}(1.06\mu\text{m})/\Delta\phi_{LEO}(1.3\mu\text{m})$ is calculated to be 1.5, which is very close to the experimental value of 1.55 (Fig.5.8). A significant variation of the phase shift is observed in the QEO effect. The QEO contribution increases dramatically as the wavelength approaches the GaAs bandgap value. This is a direct consequence of the Kramers-Kronig relation with an

electroabsorption near the bandgap, and it is represented by a strong wavelength dependence of the QEO coefficient $R(\lambda)$. $\Delta\phi_{\text{QEO}} \sim n^3/\lambda \cdot R(\lambda) \cdot \Gamma_d$. Referring to the reported wavelength dependence of R [Men88], $R \sim \exp(3/\lambda^3)$. It predicts $R(1.06\mu\text{m})/R(1.3\mu\text{m}) = 3.17$. Then, $\Delta\phi_{\text{QEO}}$ is 4.8 times larger at $\lambda=1.06\mu\text{m}$ than $1.3\mu\text{m}$, which explains very well the $\Delta\phi_{\text{QEO}}$ variation in Fig.5.8. It is found that the QEO effect provides 49 and 73 % of the total phase shift increases of the TE_0 and TM_0 modes, respectively, for the wavelength change from 1.3 to $1.06\mu\text{m}$.

5.4.3. Carrier Concentration Dependence

Clearly, the wavelength dependence of the phase shift variations of the propagating modes is a direct result of the changes of parameters such as $B(\lambda)$, $R(\lambda)$, Γ_d , and the overlap integral between the electric and optical fields. Γ_d and the overlap integral can also be altered by changing doping concentrations in the GaAs and AlGaAs layers. For example, the depletion width decreases for high doping concentrations, thus decreasing Γ_d . However, decrease in Γ_d does not necessarily mean a smaller contribution of the free carrier effects since the refractive index change due to those effects is proportional to the number of free carriers removed from the depletion region. The electric field, on the other hand, increases with increasing doping concentration although in a narrowed depletion region, resulting in phase shift variations of the electro-optic effects. Hence, the overlap integral is determined by the competing phenomena, namely, decrease of Γ_d and increase of the electric field.

Fig.5.9 shows calculated results of the phase shift efficiency versus the doping concentration in the p- and n-GaAs guiding layers at $\lambda=1.06\mu\text{m}$

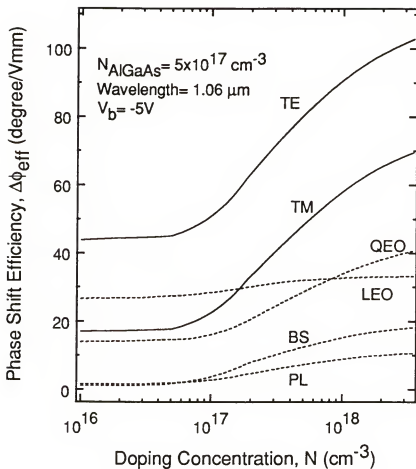


Figure 5.9 The phase shift efficiency as a function of doping concentration in p- and n-GaAs layers at $\lambda=1.06 \mu\text{m}$ and $V_b= -5\text{V}$. Up to $N= 5 \times 10^{16} \text{ cm}^{-3}$, the P-p-i-n-N modulator acts like a P-i-N modulator. When the depletion region is confined in the p-i-n GaAs layers, i.e., $N > 5 \times 10^{16} \text{ cm}^{-3}$, the phase shift efficiency begins to increase, utilizing the QEO and BS effect in the GaAs layers.

and $V_b = -5V$. The same doping concentration (N) has been assumed for the GaAs buffer layers and for the AlGaAs cladding layers; $N = 5 \times 10^{17} \text{ cm}^{-3}$. For low doping concentrations, less than $N = 5 \times 10^{16} \text{ cm}^{-3}$, the P-p-i-n-N phase modulator acts like a P-i-N phase modulator, since the GaAs buffer layers are essentially intrinsic. Limited contributions arise from the PL and BS effects due to little variation of Γ_d and negligible BS effect in the AlGaAs cladding layers. The phase shift is determined mostly by the electro-optic effects due to an extremely large overlap between the electric and optical fields. The phase shift efficiency for the low doping concentrations is estimated to be $44 \text{ }^{\circ}/\text{V}\cdot\text{mm}$ for the TE_0 mode.

As the doping concentration becomes significant enough to keep the depletion region within the GaAs guiding region for the bias voltage, the phase shift contributions from the free carrier and QEO effects increases while the LEO contribution remains almost constant. From Eqs.(5.8) and (5.9), for the PL and BS effects, the phase shift is proportional to $\sim N \cdot (x_n + x_p)$ where $(x_n + x_p) \sim 1/N^{1/2}$. Hence, $\Delta\phi_{\text{PL}}$ and $\Delta\phi_{\text{BS}}$ increase as $N^{1/2}$. From Eq.(5.10), the phase shift due to the LEO effect is proportional to $\sim F \cdot (x_n + x_p)$ where once again, $F \sim N \cdot (x_n + x_p) \sim N^{1/2}$, producing a contribution nearly independent on the doping concentration. However, the phase shift due to the QEO effect is proportional to $\sim F^2 \cdot (x_n + x_p)$, showing a $N^{1/2}$ dependence. The total phase shift efficiency for the TE_0 mode approaches $\sim 100 \text{ }^{\circ}/\text{V}\cdot\text{mm}$ for $N = 2 \times 10^{18} \text{ cm}^{-3}$ corresponding to a 130 % increase of the phase shift efficiency from that for the low doping concentrations. However, adverse effects such as large electroabsorption and free carrier absorption losses, and smaller phase shifts than expected due to the bandgap shrinkage effect, accompany the heavily-doped modulators.

5.4.4. Intrinsic Layer Thickness Dependence

A variation of the intrinsic GaAs layer thickness d_i is another way to affect the depletion width and electric field as seen in Eqs.(5.1)-(5.4), and hence a change in the phase shift of the propagating modes. The dependence of the phase shift efficiencies for the TE_0 and TM_0 modes and of the individual contributions (dotted lines) on d_i is shown in Fig.5.10 at $\lambda=1.06 \mu\text{m}$ and $V_b = -5\text{V}$. The total thickness of the p-i-n GaAs guiding layers is fixed at $0.35 \mu\text{m}$. In other words, the doped region (p- and n-GaAs) becomes wider as d_i decreases, and vice versa. The other device parameters are the same as before.

In the limiting case, for $d_i = 0.35 \mu\text{m}$, the P-p-i-n-N phase modulator corresponds to a P-i-N phase modulator with a phase shift efficiency of $43^\circ/\text{V}\cdot\text{mm}$ for the TE_0 mode. We see again very small contributions of $1.0 \sim 1.5^\circ/\text{V}\cdot\text{mm}$ from the PL and BS effects. Most of the phase shift efficiency arises from the electro-optic effects due to an extremely large overlap between the electric and optical fields, which is around 0.8 with and without the reverse bias voltage as shown in Fig.5.11. Therefore, the total phase shift for the TM_0 mode is almost the same as the QEO contribution, and that for the TE_0 mode appears to be a sum of the LEO and QEO contributions.

As d_i decreases, it is a matter of course that the depletion width and Γ_d are reduced since $(x_n + x_p) \sim \Gamma_d \sim d_i + \frac{2\epsilon_1}{qN} \frac{(V_o - V_b)}{d_i}$ as seen from Eq.(5.1) in the range $d_i > \frac{(x_n + x_p)}{2}$, i.e., $d_i \geq 0.1 \mu\text{m}$ in Fig.5.11. However, the change in Γ_d increases with decreasing d_i , since $\Delta\Gamma_d \sim V_b/d_i$. Therefore, the PL and

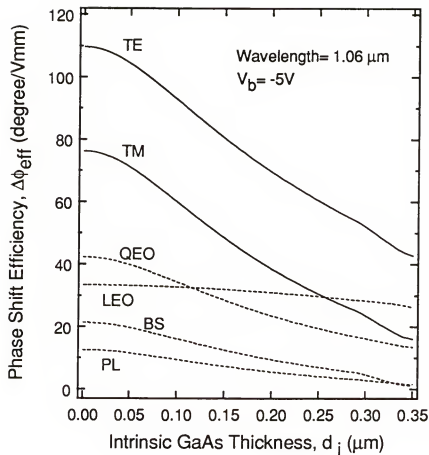


Figure 5.10 The phase shift efficiency as a function of intrinsic GaAs thickness at $\lambda = 1.06 \mu m$ and $V_b = -5V$. At $d_i = 0$, the P-p-i-n-N modulator corresponds to a p-n homojunction modulator. At $d_i = d$ ($= 0.35 \mu m$), it is a P-i-N modulator. With the decrease of d_i , the phase shift efficiency increases almost linearly down to $d_i = 0.05 \mu m$.

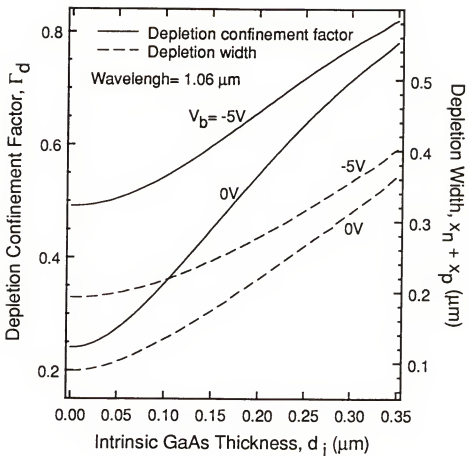


Figure 5.11 The depletion confinement factor and depletion region as a function of intrinsic GaAs thickness at $\lambda = 1.06 \mu m$ and $V_b = -5V$. At small d_i 's, larger changes in Γ_d and depletion width result in a substantial increase of the phase shift efficiency, but with large junction and dynamic capacitances. As d_i increases, less changes in Γ_d and depletion width cause small contributions from the free carrier effects, but with small capacitances.

BF contributions increase almost linearly down to $d_i = 0.05 \mu\text{m}$ as seen in Fig.5.10. The overlap between the electric and optical fields is also reduced as the Γ_d does, however the electric field in a narrowed depletion region will increase. Since $F \sim (V_o - V_b)/(x_n + x_p)$ and $(x_n + x_p) \sim d_i$, the LEO contribution proportional to $\sim F \cdot (x_n + x_p)$ is nearly independent on d_i and the QEO contribution proportional to $\sim F^2 \cdot (x_n + x_p)$ also increases linearly with the decrease of d_i .

At the other end, when d_i goes to zero, the P-p-i-n-N phase modulator behaves like a p-n homojunction phase modulator and the phase shift efficiency is estimated to be around $110^\circ/\text{V}\cdot\text{mm}$ for the TE_0 mode. The phase shift efficiency increases by factors of 2.6 and 4.7 for the TE_0 and TM_0 modes, respectively, as d_i varies from $0.35 \mu\text{m}$ to zero.

However, these substantial improvements of the phase shift efficiency are achieved at expense of a large junction capacitance and smaller speed due to a small d_i , as seen from the dependence of the depletion width on d_i in Fig.5.11. The capacitance is estimated to be about 130 and 32 nF/cm^2 at $d_i = 0$ and $0.35 \mu\text{m}$, respectively. The variation of the junction capacitance, i.e., the dynamic capacitance, also becomes significant as d_i decreases, hindering impedance matching. A 11 % variation of the junction capacitance is estimated at $d_i = 0.35 \mu\text{m}$ for the 5 V bias change and it increases up to 116 % at $d_i = 0$. As d_i decreases, the depletion region is reduced, developing a high electric field across it. The absorption loss increases by the combination of free carrier absorption in the highly-doped neutral regions and electroabsorption in the depletion region.

5.4.5. Cut-Off Frequency and Power/Bandwidth

Due to the complexity of the competing processes, it is not easy to design and optimize structure in terms of both high phase shift efficiency and speed. We focus our attention to high-frequency modulation since the high-speed operation is desirable for optical phase modulators. Since the maximum modulation speed is limited by the RC time constant, low junction capacitance as well as high phase shift efficiency is necessary. A low junction capacitance is essential for small total capacitance and a high phase shift efficiency is required for reducing the device length, resulting in a small RC time constant. In a ridge waveguide device with width much larger than the layer thickness, for π -phase shift at a given modulating voltage, the cut-off frequency can be expressed as

$$f_c = \frac{\Delta\phi_{\text{eff}} V}{2 \pi^2 R C_s w} \quad (5.15)$$

where $\Delta\phi_{\text{eff}}$ is the phase shift efficiency, V is the peak-to-peak reverse bias voltage, R is the resistance, C_s is the junction capacitance per unit area, and w is the ridge waveguide width. Using the data in Figs.5.10 and 5.11, we have calculated the cut-off frequency in Eq.(5.15) for the TE_0 mode as a function of the intrinsic GaAs layer thickness, in order to obtain an optimized DH waveguide phase modulator for high-speed operations. Driving source impedance of 50Ω and a voltage swing of 0 to -5 V were assumed. Since the speed is limited by the largest junction capacitance, C_s

was taken at $V_b = 0$. The ridge waveguide width was normalized to be $3 \mu\text{m}$. The results are shown in Fig.5.12.

For the limiting case, corresponding to a p-n homojunction phase modulator ($d_i=0$), the cut-off frequency is found to be the lowest value ~ 2.5 GHz, despite the highest phase shift efficiency available for the small d_i range. As discussed previously, this is not surprising since the phase shift efficiency was achieved at the cost of a large junction capacitance due to the narrowing of the depletion region or small d_i . Unfortunately, the resultant rate of increase of the junction capacitance C_s turns out to be larger than the phase shift efficiency $\Delta\phi_{\text{eff}}$ as d_i decreases. $f_c = 2.4$ GHz is estimated for the highest efficiency of $96^\circ/\text{V-mm}$ reported for the p-n homojunction phase modulator with doping concentration of $N = 4 \times 10^{17} \text{ cm}^{-3}$ [Men88], while a value of 4.7 GHz was estimated by using the junction capacitance at $V_b = -4$ V.

f_c increases steadily with increasing d_i , reaching a maximum value of ~ 4.1 GHz at $d_i = 0.3 \mu\text{m}$. It decreases slightly for $d_i > 0.3 \mu\text{m}$. This is due to reduced electro-optic contributions by the penetration of the depletion region into the AlGaAs cladding layers. We have estimated a bandwidth of ~ 3.5 GHz for our experimental devices with $d_i = 0.15 \mu\text{m}$.

It has been reported for P-i-N phase modulators [Fai87a, Fai87b] that measured junction capacitances at $V_b = 0$ were 1.5 - 2 times larger than expected ones. This is due to the spilling of free carriers into the intrinsic GaAs layer by the bandgap discontinuities at heterojunctions. This effect was also observed in a P-n heterojunction phase modulator [Fai87a]. Thus, there seems to be fundamental limitation in achieving high cut-off frequencies in structure where the depletion region meets the free-carrier accumulation region at heterojunction under bias. For example, by using

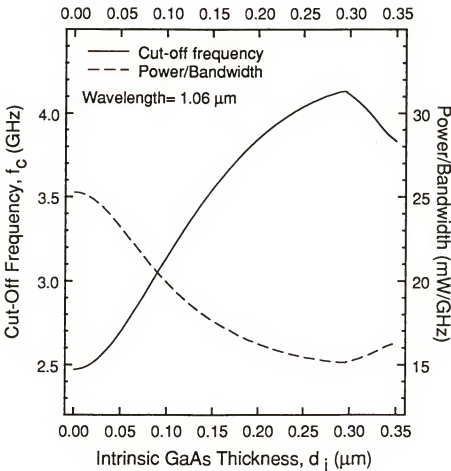


Figure 5.12 The cut-off frequency and power/bandwidth as a function of intrinsic GaAs layer thickness at $\lambda = 1.06 \mu\text{m}$ for a voltage swing from 0 to -5V. Highest f_c and lowest P/BW occur at $d_i = 0.3 \mu\text{m}$. Despite the highest efficiency, $d_i = 0$ case has the lowest f_c due to its large capacitance. When the depletion region extends into AlGaAs cladding layers ($d_i = 0.3 - 0.35 \mu\text{m}$), f_c decreases due to smaller electro-optic and BS contributions in the AlGaAs layers.

the reported junction capacitances, bandwidths of 2.5 and 1.4 GHz are estimated for reported efficiencies of $62^{\circ}/V\cdot mm$ of the P-i-N phase modulators and $100^{\circ}/V\cdot mm$ of the P-n heterojunction phase modulator, respectively.

It is clear that the p- and n-GaAs layers play an important role in increasing the phase shift efficiency and cut-off frequency by utilizing the higher-order effects in GaAs and preventing the extension of the depletion region over undesirable heterojunctions. It is suggested that the optimized structure consists of $d_i = 0.25 \sim 0.30 \mu m$ for the present parameters of $N = 5 \times 10^{17} cm^{-3}$, $d = 0.35 \mu m$, and $V_b = -5 V$. Of course, when lower values of N and d are used, the intrinsic layer thickness should be reduced so as to avoid the depletion region reaching the heterojunctions.

The figure of merit viz., power/bandwidth is an important parameter for characterizing high-speed performance of the phase modulators. Since we assumed a constant bias voltage swing for the π -phase shift, the power required to drive the modulator is $V^2/8R$. From Eq.(5.16), the power/bandwidth is given by

$$P/BW = \frac{2\pi^2}{8} \frac{C_s w V}{\Delta\phi_{eff}} \quad (5.17)$$

The data are plotted as dotted lines in Fig.5.12 as a function of the intrinsic GaAs layer thickness. Among the parameters in Eqs.(5.16) and (5.17), C_s and $\Delta\phi_{eff}$ are the only parameters affected by d_i . Since they counteract each other, the highest cut-off frequency 4.1 GHz gives lowest drive power/unit bandwidth viz., 15.2 mW/GHz at $d_i = 0.30 \mu m$. A largest figure of merit of 25 mW/GHz is estimated at $d_i = 0$ and 18 mW/GHz for our experimental devices.

5.5. Conclusion

A P-p-i-n-N waveguide structure consisting of p-i-n GaAs layers as guiding region and AlGaAs layers as cladding layers has been analyzed. The modal distribution is determined by the guiding and cladding layers, and the depletion region is usually confined in the p-i-n GaAs layers for the utilization of the higher-order (QEO and BS) effects, their wavelength dependences, and the LEO effect. Therefore, the electric and optical fields can be adjusted independently to obtain an optimized GaAs/AlGaAs phase modulator for high-speed operation.

We have described a detailed theoretical analysis of the P-p-i-n-N GaAs/AlGaAs waveguide phase modulator, which predicts and interprets the experimental phase shifts successfully by using well-known physical effects occurring in the depletion region. The experimental phase shift efficiency of the P-p-i-n-N phase modulator was 82 and 37.5 °/V·mm for the TE₀ mode at $\lambda = 1.06$ and $1.3 \mu\text{m}$, respectively. These values are very close to the reported highest efficiencies at the same wavelengths. The theoretical and experimental results show an excellent agreement with the QEO coefficient as a fitting parameter. From the theoretical and experimental results, we estimated R to be $4.3(\pm 0.5) \times 10^{-16} \text{ cm}^2/\text{V}^2$ and $1.3 (\pm 0.5) \times 10^{-16} \text{ cm}^2/\text{V}^2$ at $\lambda = 1.06$ and $1.3 \mu\text{m}$, respectively. The variation of R follows to the theoretical dispersion, i.e., $R \sim \exp(3/\lambda^3)$, and the values of R measured by us are slightly larger than the previous experimental values when calibrated to the same wavelengths.

The wavelength dependence of individual contributions from the PL, BS, LEO, and QEO effects has been studied. The QEO contribution increases

dramatically as the wavelength approach the GaAs bandgap value. The BS effect is also affected significantly but it shows a limited contribution because of the small variation of the depletion confinement factor. Hence, even at the short wavelength of $1.06 \mu\text{m}$, the electro-optic effects still account for 74 % of the total phase shift for the TE_0 mode. The carrier concentration dependence of the phase shift efficiency has also been investigated. As the carrier concentration N increases, the phase shift increases as $\sim N^{1/2}$, and the phase shift efficiency for the TE_0 mode reaches $\sim 100 \text{ }^{\circ}/\text{V}\cdot\text{mm}$ for $N = 2 \times 10^{18} \text{ cm}^{-3}$. However, due to the resulting large absorption loss and less-than-expected phase shift in heavily-doped GaAs and AlGaAs, it is suggested that the doping concentration should be less than $1 \times 10^{18} \text{ cm}^{-3}$.

Depending on the intrinsic GaAs layer thickness, the P-p-i-n-N phase modulator can be either a P-i-N or a p-n homojunction phase modulator. Therefore, direct comparisons between them have been possible in terms of the phase shift efficiency and junction capacitance, which determine the cut-off frequency. For a ridge waveguide modulator of $3 \mu\text{m}$ width, a highest cut-off frequency of $\sim 4 \text{ GHz}$ was estimated for the P-p-i-n-N phase modulator with an intrinsic layer thickness of $0.30 \mu\text{m}$. On the other hand, the p-n homojunction phase modulator with the same waveguide parameters shows a lower value of $\sim 2.5 \text{ GHz}$. The P-i-N phase modulator, on the other hand, has a cut-off value of slightly less than 4 GHz , but in practice, a significant reduction of the cut-off frequency is expected due to the increased capacitance on account of the accumulated free carriers at the P-i and N-i heterojunctions. A lowest power/bandwidth of 15.2 mW/GHz can be achieved for the P-p-i-n-N phase modulator with an intrinsic layer thickness of $0.30 \mu\text{m}$.

CHAPTER SIX
NOVEL MQW STRUCTURE FOR
LASER-PHASE MODULATOR INTEGRATED DEVICE

6.1. Introduction

While many semiconductor photonic devices have been well developed, their monolithic integration has been limited to some special cases including one or two devices, such as multistage couplers or switches using simple waveguide structures [Aji87, Ish89], (laser)-waveguide-detector integration [Cin87, Lio89], laser-high speed electronic device integration [Che87], laser-external cavity integration [Wer89], and laser-modulator integration [Ara86a, Kaw87, Suz87, Tar86, Tho88]. Especially, integration with lasers has been limited seriously in spite of its significant demand in integrated optics. This is due to a strict requirement that integrated components, except for detectors, have to have transparent active layers for the light generated by the laser. The bandgaps of the active layers have to be larger than that of laser.

The problem has been solved by growing a laser structure first, and regrowing desirable materials on selectively etched areas for the other components. However, looking at integration results to date, it does not seem feasible to integrate various devices by using only regrowth techniques. Present regrowth techniques still have a lot of difficulties such as rough interfaces between regrown and as-grown materials, and poor surface morphology. Moreover, the number of regrowth steps increases as

we add additional devices for integration. This procedure is impractical for future large scale integrated optical circuits useful for various functions. Therefore, it is essential that new growth technologies, novel integration schemes and device structures capable of reducing regrowth steps should be developed at the same time.

In this chapter, we discuss the requirements of integrating a novel MQW structure with a SQW laser and describe, conceptually, a novel integration scheme applicable on the MQW structure without regrowth. First, we discuss necessary operating conditions and fabrication techniques for laser-modulator integrated devices in section 6.2. Based on the discussions, we design a novel MQW structure for laser-phase modulator integration utilizing etching and/or impurity induced disordering, which is presented in section 6.3. For the purpose of testing the feasibility of an asymmetric SQW laser to be used in the proposed integrated device, we have fabricated and characterized broad-area asymmetric SQW lasers. They are shown to have good lasing characteristics such as low threshold current density and narrow linewidth in section 6.4. For efficient phase modulation, the wavelength detuning between the operating wavelength (lasing wavelength) and the bandgap of phase modulator (excitonic resonance peaks) is necessary. Therefore, to determine well thicknesses of the SQW and MQW's, and to obtain preliminary results for phase modulation, transverse MQW intensity modulators have been fabricated and characterized. This is described in section 6.5. MQW phase modulator as well as the asymmetric SQW laser are the two principal components in our proposed integrated device. Therefore, we discuss the promising operating characteristics of recently developed MQW phase modulators for

tens of GHz light modulation in section 6.6, in view of their applications to the laser-modulator integration.

6.2. Design Considerations for Laser-Modulator Integration

Laser-modulator integrations reported to date are largely divided into two types; laser-electroabsorption modulator integration and laser-phase modulator integration. Fig.6.1 shows a typical composite waveguide for the integrated devices. Laser operates at a constant injection current I_L , and coupled light is modulated with bias voltage V_m . A narrow active layer is preferred in the laser section for low threshold current and single mode operation. On the other hand, a thicker active layer is suitable for the modulator section in order to achieve a large overlap of optical and modulating electric fields. This usually calls for the guide material to be different from the laser active layer material for efficient modulation. Therefore, mode mismatch between two devices is inherent, resulting in significant coupling loss.

One of the advantages of laser-modulator integrated devices is good coupling efficiency. However, it does not always ensure desirable operating characteristics since the lasing conditions for the integrated devices with good optical coupling efficiency are severely affected by the change of optical reflection at the laser-modulator boundary [Suz88]. The lasing condition is determined by including the total waveguide loss occurring in laser and modulator waveguide sections. For the sake of our explanation, the two sections are separated in Fig.6.1, and the influence of the modulator waveguide loss on the lasing condition is represented by reflected power P_{mL} . The reflected light is a function of modulation bias V_m . The phase and

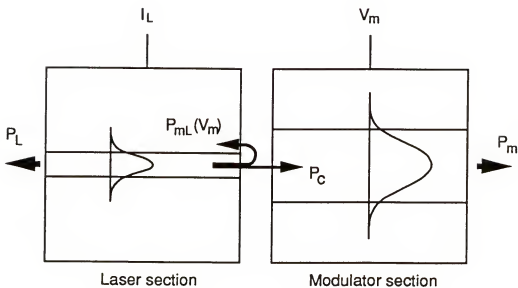


Figure 6.1 Schematic diagram of composite waveguide for laser-modulator integrated device. P_c and P_{mL} indicate the coupling of light from laser to modulator and the reflected light from modulator to laser, respectively.

magnitude of the reflected light are altered due to the changes of refractive index and absorption in the modulator waveguide by the modulation bias, causing lasing wavelength to shift and laser output power to vary. This corresponds to a kind of direct modulation with increasing linewidth even though the linewidth enhancement for integrated devices is still much less than that for directly modulated lasers.

In laser-electroabsorption modulator integration, the above effect is significant because intensity modulation is usually performed in the wavelength region with large changes of absorption and refractive index. Therefore, integrated electroabsorption modulators have not worked efficiently for intensity modulation [Tar86], although solitary electroabsorption modulators have shown promising modulation characteristics including small chirp, high speed and large on-off ratio [Nod86]. Instead, they have worked well as lossy waveguides for short optical pulse generation by Q-switching. This function has been implemented successfully in MQW laser-MQW electroabsorption modulator integrated devices [Ara86a, Tho88], by utilizing the large excitonic absorption and its significant shift with applied electric field (QCSE). Recently, distributed feedback (DFB) laser-electroabsorption modulator integrated devices have also been reported with much improved intensity modulation characteristics [Kaw87, Suz87]. However, the improvements could be achieved by poor optical coupling (1 - 2 percent) between the laser and the modulator, with reduced effect of the absorption changes on the lasing condition. Furthermore, they had to rely on complicated regrowth and etching techniques such as three-step VPE and hybrid LPE/MBE.

On the other hand, phase modulation utilizes only a small change of refractive index, ideally, without an absorption change. Refractive index changes useful for reverse-biased semiconductor phase modulators range in the order of 10^{-3} . These changes are so small compared to the refractive indices of semiconductors that they cause negligible variations in the reflected power, resulting in stable lasing condition. Hence, laser-phase modulator devices are considered more suitable for light modulation than laser-absorption modulator devices when they are monolithically integrated. Moreover, phase modulator can provide intensity modulation by combining coupler or interferometer geometries, and can be easily integrated with other optical devices utilizing similar refractive index changes in waveguides without additional regrowth. However, the wavelength detuning condition is indispensable for efficient phase modulation while it is not so restrictive for laser-electroabsorption modulator integration. Furthermore, as the recent demonstration of MQW laser-MQW phase modulator integrated device [Kor88] have indicated, regrowth was required for the wavelength detuning and large overlap of optical and modulating electric fields.

Electrical isolation between the two sections is another important factor for high-speed modulation. Since laser is forward-biased and modulator is reverse-biased, a small variation of modulation bias can change the injection condition for laser significantly. For example, when laser and modulator are poorly isolated, injection current into laser is decreased considerably due to leakage current into modulator as the modulation voltage V_m increases, resulting in an increase of the threshold current, consequently a decrease of the laser output power, and a change of the lasing wavelength. Furthermore, the leakage current increases the

capacitance of the modulator and the extremely large capacitance of the laser is coupled through the poor electrical resistance, affecting high-speed modulation seriously.

There are three well-known methods for electrical isolation. One is formation of p-n-p junctions between laser and modulator by diffusing n-type impurity such as silicon. However, it was found experimentally to give a very poor isolation, about few $100\ \Omega$ [Suz88], because it builds heavily-doped p-n junctions along the surface, permitting carrier tunneling under a small bias voltage. Another is etching the intermediate region between laser and modulator sections down to the intrinsic MQW layers and filling the etched region with an easy to deposit dielectric material such as polyimide. This provides good electrical isolation, of the order of $M\Omega$ [Suz88], but reduces the optical coupling efficiency significantly due to the light scattering at the etched boundary. The last approach is to proton bombard the intermediate regions. This is the most frequently used method as it gives an excellent isolation, about few $M\Omega$ [Tho88], although it increases somewhat the propagation loss. Theoretically, electrical resistance of at least $100\ K\Omega$ or more between the integrated components is recommended for high-speed modulation [Suz88]. Therefore, the latter two methods are considered suitable for integrated devices.

6.3. Novel MQW Structure for Laser-Phase Modulator Integration

We have discussed desirable integration techniques for laser-modulator integrated devices in the previous section. Based on the previous discussions, number of schemes for SQW laser-MQW phase modulator integration can be utilized, e.g., etching (Fig.6.2), regrowth [Suz87, Kaw87],

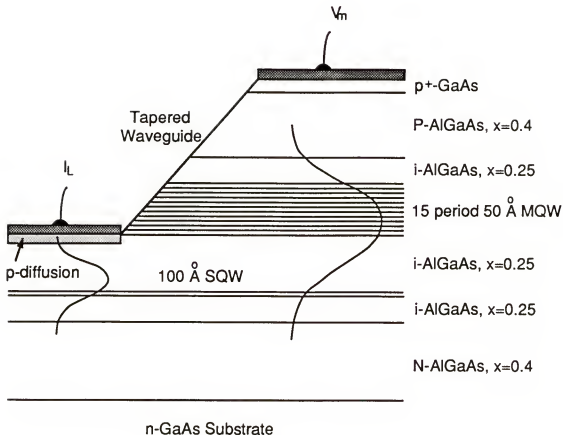


Figure 6.2 Cross-sectional view of the proposed MQW structure for SQW laser-MQW phase modulator integrated devices.

and impurity induced disordering [Tho87, Tho88]. The structure should contain SQW and MQW's in the intrinsic active region, with different well thicknesses, separated by a thick $\text{Al}_{0.25}\text{GaAs}$ barrier layer. These two QW regions act as active layers of the laser and phase modulator in the integrated device.

In the laser section, the MQW's are removed by using wet-chemical etching or reactive ion etching, resulting in an asymmetric SQW laser (Fig.6.2). In spite of the asymmetry, the SQW laser is found to be an efficient light generator with low threshold current and narrow linewidth, as described in section 6.4. The generated light is coupled to the phase modulator section through the tapered waveguide region. With appropriate design, the coupling efficiency can be maximized. In addition, as discussed in the previous section, phase modulation would provide the stable lasing condition even with large coupling efficiencies. Recently developed angled reactive ion etching (ARIE) [Tak89a] is considered to be the most useful and simple technique for fabricating such tapered waveguides as shown in Fig.6.2. Since the slope of the tapered waveguide is determined by an angled holder specially designed for mounting the sample during reactive ion etching and the preferential etching along certain planes, both the length and the coupling efficiency can be easily controlled. Furthermore, this kind of coupling scheme also provides excellent electrical isolation because the laser and modulator sections are separated by a thick intrinsic layer. Note that the electrical isolation techniques discussed in the previous section, in general, do not provide both efficient light coupling and good electrical isolation at the same time.

An alternative for the formation of tapered waveguides is to use impurity induced disordering (IID). IID in III-V compound semiconductor

MQW structures has received considerable attention recently because of the potential use for the fabrication of OEIC's. IID of quantum-well layers is known to occur due to enhanced interdiffusion of constituent elements of the alloy materials (i.e., Ga and Al) by impurity diffusion, resulting in large shift of the bandgap (or the PL peak) to higher energies in the QW layers. It has proved to be a very practical technique for defining lateral confinement of modal field by utilizing the bandgap shift to higher energies and the consequent decrease of refractive index in the disordered layers: For example, planar two-dimensional waveguides [Hau88, Kap87, Kap88] have been demonstrated without a ridge or a channel structure; buried heterostructure MQW lasers [Epl87, Wel87] have been produced; moreover, integration of laser, electroabsorption modulator, and low-loss waveguide [Tho87, Tho88] has been successfully implemented on as-grown MQW structures.

In the modulator section, the MQW's become the principal active region for phase modulation. Therefore, the well thickness of the SQW is designed to be larger than that of the MQW's to avoid serious absorption loss in the modulator waveguide. As the wavelength approaches the excitonic resonance, the phase shift efficiency increases significantly due to large refractive index change associated with the QCSE in the MQW's (section 2.4), accompanied by an increase in the absorption loss. Hence, a compromise between large phase shift efficiency and absorption loss is necessary for selecting the operating wavelength. Wavelength detunings of $300 \sim 400 \text{ \AA}^{\circ}$ between heavy-hole exciton peaks of the SQW and MQW's have been suggested for high phase shift efficiency with acceptable absorption loss (intensity modulation) [Zuc88a]. From previously reported data and our experimental results for transverse MQW intensity modulators described

in section 6.5, well thicknesses of 100 Å and 50 Å, and an AlAs mole fraction of 0.25 for $\text{Al}_x\text{Ga}_{1-x}\text{As}$ barrier layers have been chosen for the SQW and MQW's, which correspond to a wavelength detuning of ~ 370 Å.

6.4. Asymmetric SQW Laser

As mentioned in the previous section, the proposed laser-modulator integrated device will have an asymmetric waveguide as a result of etching of MQW's in laser section. An increase of the threshold current is expected due to poor light confinement caused by the asymmetry. Therefore, to test the feasibility, we have fabricated asymmetric SQW lasers (Fig.6.3), which have a similar structure as laser section of the integrated devices. We grew the asymmetric 100 Å SQW structure and replaced the MQW region in Fig.6.2 with a thick $\text{Al}_{0.25}\text{Ga}_{0.75}\text{As}$ barrier layer, instead of etching the MQW layers. Broad-area asymmetric SQW lasers were fabricated by evaporating 100 μm -wide Ti/Au stripes on the top surface for the p-type contact, and Au-Ge/Ni/Au on the bottom surface for the n-type contact. Thermal annealing at 450 °C for 2 minutes was performed in $\text{H}_2\text{-N}_2$ forming gas ambient to form ohmic contacts. Samples were cleaved into lengths of 300 - 700 μm .

Fig.6.4a shows the measured light output power versus injection current under pulsed operations with 1 μs duration and 2 KHz repetition rate. A calibrated Si photodiode was used to detect the optical power. The threshold current was 300 mA, which corresponds to a threshold current density of 577 A/cm^2 . This threshold current density is two times larger than the lowest low threshold current densities of 200 - 300 A/cm^2 reported for GaAs/AlGaAs GRIN-SCH (graded index waveguide-separate

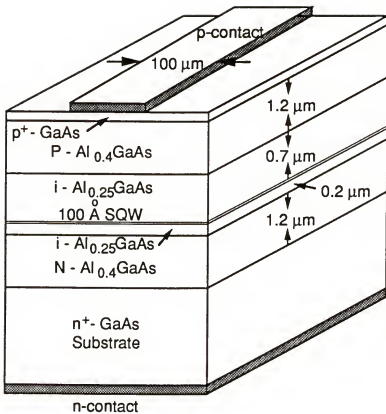


Figure 6.3 Schematic diagram of broad-area asymmetric SQW laser demonstrated with low threshold current density. 100 \AA SQW is located in the lower part of the intrinsic guiding region.

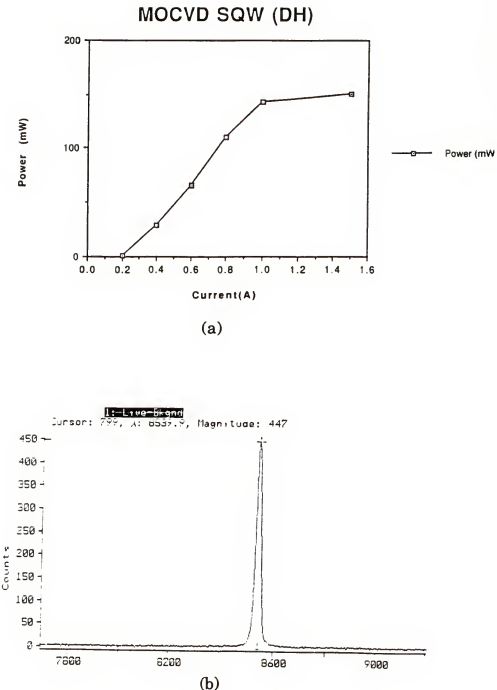


Figure 6.4 Lasing characteristics of the broad-area asymmetric SQW laser in Fig.6.3; (a) power vs. injection current, and (b) lasing spectrum.

confinement heterostructure) SQW lasers [Ara86b]. However, we must realize that the asymmetric SQW lasers are very efficient since they can lase with reasonably small threshold current density in spite of an extremely small confinement factor of less than 0.005 compared to confinement factors of ~ 0.03 for the GRIN-SCH SQW lasers. The maximum output power was ~ 150 mW from one facet. Fig.6.4b shows the measured spectrum of lasing wavelength. It peaks at $\lambda = 0.854 \mu\text{m}$ with the full width at half maximum (FWHM) of $\sim 20 \text{ \AA}^\circ$, which is a typical value for broad-area GaAs/AlGaAs SQW lasers. The lasing wavelength is found to be 70 \AA° below the heavy-hole excitonic resonance. The results show that the asymmetric SQW lasers with its good lasing characteristics, are quite suitable for the SQW laser-MQW phase modulator integration.

6.5. Transverse MQW Intensity Modulators

As discussed earlier, the wavelength detuning between the lasing wavelength and excitonic resonances of the MQW layers is absolutely necessary. For the purpose of determining well thicknesses of the SQW and MQW's, we have fabricated P-i-N GaAs/AlGaAs MQW structures containing MQW layers with various well thicknesses in the intrinsic region. The MQW structures with back-hole etched GaAs substrate allow us to evaluate the absorption spectrum including room-temperature exciton peaks by directly measuring the spectral transmittance. Furthermore, by depositing contacts on the top and bottom sides, we can measure the shift of excitonic absorption peaks as a function of applied electric fields (QCSE). This makes it possible to calculate the electrorefraction via the Kramers-

Kronig dispersion relation, and hence obtain a preliminary estimation of the phase shift in the proposed integrated device.

Figs.6.5a and 6.5b show schematic diagrams of contact and mesa patterns on the top side and cross section along the A-A' line for the P-i-N MQW structures, respectively. Monochromatic light is incident vertically, and its transmission is modulated by applying reverse bias voltage. This geometry pertains to the so-called transverse MQW intensity modulator. The absorptive p⁺-GaAs contact layer and n⁺-GaAs substrate were etched to provide optical windows on both sides, thus allowing absorption of incident light to occur only in the intrinsic MQW layers. Mesa structure was used to reduce the dark current by confining the depletion region in a small area. Anti-reflection coatings were also deposited on both the faces to eliminate, although not entirely, the Fabry-Perot resonances due to multiple reflections in the P-i-N layers over the wavelength region of interest. In addition to the above procedures, the fabrication of the transverse MQW intensity modulators includes a number of complicated steps. For instructive reasons, we describe the entire fabrication procedures in a simple manner as follows:

- **Ring contact formation on the top surface by lift-off technique:**
 - 1) Clean and degrease P-i-N MQW sample with TCE, acetone, methanol, and rinse with D.I.water, sequentially and without exposing the sample in air.
 - 2) Blow dry with N₂ and prebake at 130 °C for 30 min.
 - 3) Spin-coat positive photoresist (Shipley 1400-27) at 5000 rpm for 40 sec. (photoresist thickness of 1.2 μm).
 - 4) Soft-bake at 90 °C for 30 min.

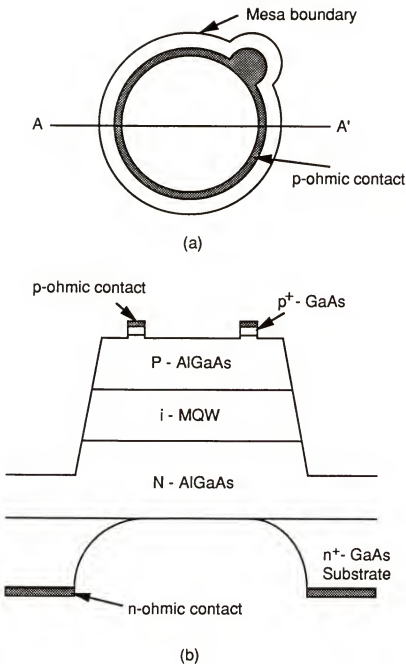
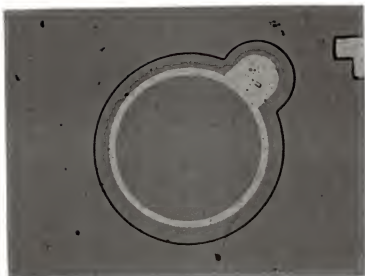
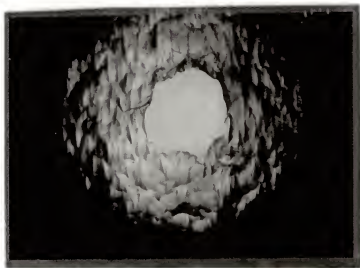


Figure 6.5 Schematic diagrams and pictures of transverse MQW intensity modulator.
 (a) Top view with ring contact and mesa patterns.
 (b) Cross sectional view along the line A-A'.



(c)



(d)

Figure 6.5 Continued.

- (c) Top view of transverse MQW intensity modulator fabricated following the described procedures.
- (b) Bottom view with back-hole etched substrate and bright-colored AlGaAs layer in the center.

- 5) Align to contact mask and expose to UV light for 9 sec.
- 6) Soak in chlorobenzene for 4 min. (solidification depth of 0.5 μm from the photoresist surface).
- 7) Develop using a diluted Shipley developer (MF-351 developer:H₂O =1:5) for about 1 min. until contact pattern is fully developed.
- 8) Wet chemical etch slightly just before metal deposition to remove native oxides (NH₄OH:H₂O₂:H₂O=20:7:100, etch rate= ~ 2 $\mu\text{m}/\text{min.}$).
- 9) Deposit Ti/Au=100/2000 \AA or Cr/Au-Zn/Au=100/1500/1000 \AA by electron-beam evaporation at a pressure of less than 10⁻⁶ Torr and at a deposition rate of 2 $\text{\AA}/\text{sec.}$
- 10) Remove unwanted metal film with photoresist by soaking in acetone and agitating slightly. See Fig.6.5c.
- 11) Rinse with methanol and D.I. water, and blow dry with N₂.

- **Mesa structure and optical window formations on the top side:**
 - 12) Wet chemical etch the p⁺-GaAs contact layer for 15 sec. by using NH₄OH:H₂O₂:H₂O=20:7:100 etching solution (etching depth of 0.5 μm).
 - 13) Repeat the steps 3) - 4).
 - 14) Align to mesa mask and expose to UV light for 9 sec.
 - 15) Develop using the same developer for 10 sec.
 - 16) Hard-bake at 115 - 120 °C for 30 min.
 - 17) Wet chemical etch down to the middle of the lower AlGaAs layer for 1 min. 15 sec. by using NH₄OH:H₂O₂:H₂O=20:7:100 etching solution (etching depth of 2.5 μm). See Fig.6.5c.
 - 18) Remove photoresist in acetone and rinse with methanol and D.I. water.
- **Back-hole etching for optical window on the bottom side:**

- 19) Lap down to 4 mils by using aluminum oxide polishing powder.
- 20) Repeat the steps 1) - 4).
- 21) Repeat the steps 15) - 17) with back-hole mask on the bottom side.
- 22) Wet chemical etch the GaAs substrate through the back-holes for 5 min. by using highly-selective etchant $\text{NH}_4\text{OH}:\text{H}_2\text{O}_2=1:20$ (pH= 8.2, etching rate of $\sim 4 \mu\text{m}/\text{min.}$).
- 23) Remove residual arsenic oxide for 30 sec. by using $\text{HCl}:\text{H}_2\text{O}=1:1$ etching solution.
- 24) Repeat the steps 22) - 23) until shiny surface of the lower AlGaAs layer appears. See Fig.6.5d.
- 25) Remove photoresist in acetone and rinse with methanol and D.I. water.

- **Back contact formation and antireflection coating deposition:**
 - 26) Repeat the steps 3) - 9) with back contact mask and thicker photoresist (Shipley 1400-33 at 4000 rpm).
 - 27) Deposit $\text{Au-Ge/Ni/Au}=1500/300/1000\text{\AA}$ by electron-beam evaporation at a pressure of less than 10^{-6} Torr and at a slow deposition rate.
 - 28) Repeat the steps 10) - 11).
 - 29) Thermal anneal at 450°C for 2.5 min in $\text{H}_2\text{-N}_2$ (5-95 %) forming gas ambient to make ohmic contacts.
 - 30) Evaporate SiO for antireflection coating on both sides, shining the white light on the coated surface, monitoring the reflection of the near-monochromatic light of interest through the filter, and stopping the evaporation at the minimum reflection.

MQW intensity modulators fabricated by following the above steps are mounted on the optical setup (Fig.6.6) for measuring the transmission. The

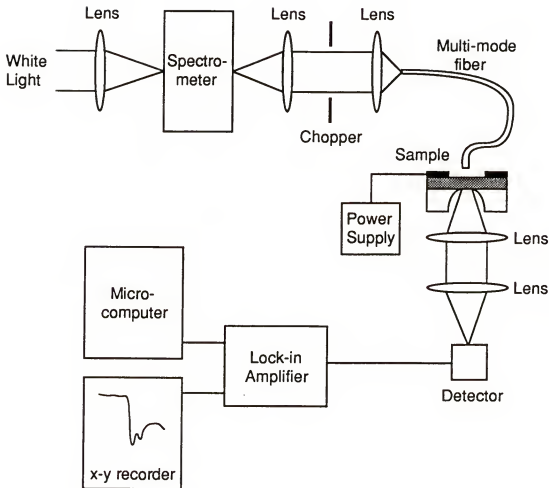


Figure 6.6 Experimental setup for the measurement of light transmission through MQW intensity modulator. The absorption coefficient and the QCSE can be estimated from measured transmittance.

monochromatic light is produced by the use of a spectrometer and a white light source. The system is easy to use since the spectrometer can be controlled by a computer. The power of the monochromatic light ranges from a few μW to tens of nW depending on the wavelength and input and output slit widths of the spectrometer. It is desirable to use small power (tens of nW) as long as the signal to noise ratio is reasonable. This avoids possible absorption modulation due to carrier generation. We obtain $\sim 5 \text{ \AA}^{\circ}$ resolution with slits in the range of $50 - 100 \text{ \mu m}$. The monochromatic light is coupled into a multi-mode fiber by a microscope objective. The use of multi-mode fiber makes it easy to align the input light and the optical window of MQW modulator by bringing them in close proximity, and, in addition, to couple the monochromatic light onto the sample vertically, which is necessary for applying the bias voltage by using pin probes (without wire bonding) as seen in Fig.6.6.

The light transmitted through the MQW layers is focused onto a thermoelectrically-cooled germanium detector or a silicon detector by using a microscope objective. The detected signal is sent to the lock-in amplifier where the background noise is eliminated by using reference from the chopper signal. The recovered signal is sent to both x-y recorder for monitoring the data directly and to the computer for collecting the data. Since the response of the detector and the monochromator depend on the wavelength, the signal transmitted through sample is normalized to the detected signal without the sample. The results are shown in Figs.6.7a and 6.7b for 75 periods of 100 \AA° MQW and 100 periods of 50 \AA° MQW intensity modulators, respectively. For the 100 \AA° sample, the heavy-hole exciton peak is at $\lambda = 0.848 \text{ \mu m}$ and the light-hole peak at $\lambda = 0.842 \text{ \mu m}$. For the 50 \AA° sample, the heavy-hole exciton peak is at $\lambda = 0.817 \text{ \mu m}$ and the light-hole

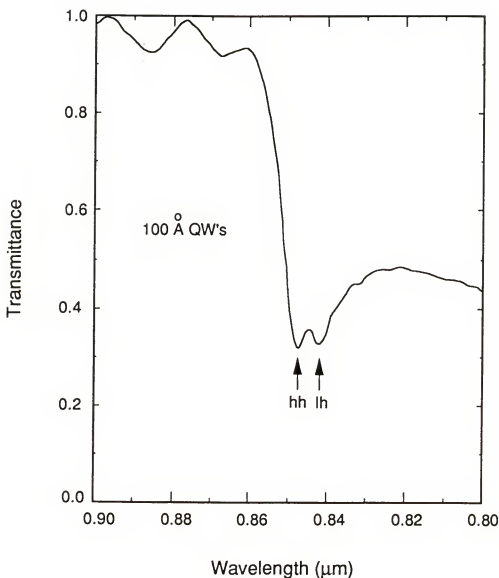


Figure 6.7 Light transmittances as a function of wavelength measured by using the setup in Fig.6.6.
(a) 75 period 100 Å MQW intensity modulator.

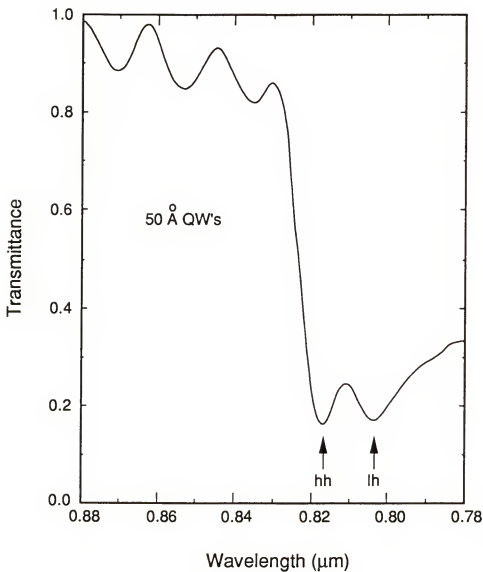


Figure 6.7 Continued.

(b) 100 period 50 Å MQW intensity modulator.

peak at $\lambda = 0.804 \mu\text{m}$. A wavelength detuning corresponding to 310 \AA° is obtained between the two heavy-hole exciton peaks. However, as we observed in the previous section, the lasing wavelength of the asymmetric 100 \AA° SQW laser is at $\lambda = 0.854 \mu\text{m}$. Thus, the actual wavelength detuning will be about 370 \AA° , which is sufficient to ensure both high phase shift efficiency and low intensity modulation if the 100 \AA° SQW and 50 \AA° MQW's are incorporated in the laser-phase modulator integrated device.

Without antireflection coatings, we could not observe exciton peaks due to significant Fabry-Perot resonances over the entire wavelength region. To overcome this problem, silicon oxide (SiO) was evaporated on both the sides of the samples. Setting the reflection detecting equipment including white light source, detector and filter on the electron-beam evaporator, the film thickness was controlled by observing the reflection of near-monochromatic light at $\lambda = 0.85 \mu\text{m}$ from the sample surface. Assuming 30 % reflection from the initial surface, the reflection was reduced down to $\sim 5 \%$ corresponding to a film thickness of $\sim 0.12 \mu\text{m}$ (royal blue). As seen in Fig.6.7, although there are still some Fabry-Perot resonances in the high transmission region, they are negligible in the low transmission region, showing clear room-temperature heavy-hole and light-hole exciton peaks. However, in order to estimate the absorption coefficient and its change as a function of bias voltage, more accurate measurements are needed with better antireflection coatings (less than 1 % reflection) or by stain etching the surface.

The measurement for absorption modulation as a function of reverse bias voltage was not successful due to low doping (the order of 10^{16} cm^{-3}) in the upper P-AlGaAs layer. The poor conductivity in that layer resulted in insufficient electrical potential to permit the depletion of the intrinsic MQW

layers under the optical window region. As a result, small shifts of the heavy-hole exciton peak of ~ 35 and $\sim 10 \text{ \AA}^\circ$ were observed at the reverse bias voltage of 20 V for the 100 and 50 \AA MQW intensity modulators, respectively. These shifts are much smaller than $100 - 200 \text{ \AA}^\circ$ reported for similar MQW intensity modulators [Whi88].

6.6. MQW Waveguide Phase Modulator

As discussed in section 2.4, there has been considerable interest in the electric field dependence of the optical properties in semiconductor quantum well structure. Even under large electric field applied perpendicular to the QW layers, the absorption edge near the bandgap is shifted to lower energies while preserving the room temperature exciton resonance peaks (QCSE), and maintaining the sharp absorption edge. This is of practical interest for intensity modulators and optical switches operated at wavelengths compatible with diode lasers. Recently, large refractive index change associated with the QCSE has attracted much interest because of its application for electro-optic devices such as phase modulators, couplers, and switches.

An extremely high phase shift efficiency of $520 \text{ }^\circ\text{V}\cdot\text{mm}$ (Fig.6.8) for a GaAs/AlGaAs MQW modulator has been reported at $\lambda = 0.8857 \text{ } \mu\text{m}$ and an operating bias voltage of -26 V [Zuc88a]. The wavelength detuning was 400 \AA° and 50 QW's was employed in the active region. Most of the high efficiency is due to the refractive index change associated with the QCSE, showing a quadratic dependence on the bias voltage. However, as seen in Fig.6.8, the increase in the phase shift efficiency with DC bias voltage is accompanied by a gradual decrease in the chirp factor ($\Delta n/\Delta k$) where Δk is

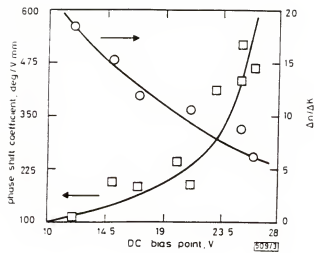


Figure 6.8 Phase shift efficiency (squares) and chirp factor (circles) as a function of reverse bias voltage, measured in the 50 period 100 \AA MQW phase modulator for 1 V voltage swing [Zuc88a].

the change of the imaginary part of the refractive index. In other words, an increase in residual intensity modulation was observed. This is a direct result of the QCSE and its associated refractive index change. For the 50 period MQW phase modulators, 1.2 dB intensity modulation was estimated for a 100 μm long device operating at - 26 V with a 400 \AA detuning. This intensity modulation is too large for MQW phase modulator to produce efficient modulation in the laser-phase modulator integrated devices shown in Fig.6.2. The generally accepted chirp factor for efficient phase modulation, i.e., when phase modulation is dominant over intensity modulation, is at least 10. Thus, the 50 period MQW phase modulator is desirable to be operated at the reverse bias voltages of less than -20 V.

It has been reported [Hau89, Zuc88b] that the chirp factor ($\Delta n/\Delta k$) becomes very large with decrease in the number of QW's and increase in the wavelength detuning, although the phase shift efficiency decreases. For the reduction of intensity modulation, a 15 period 50 \AA MQW phase modulator in our integrated device (Fig.6.2) has been designed with a 370 \AA wavelength detuning mentioned in the previous section. There are two factors involved in our MQW phase modulator for reducing the 1.2 dB intensity modulation observed in the 50 period 100 \AA MQW phase modulator; one is a small number of QW's and the other is narrow thickness of QW's. Intensity modulation is expected to be decreased by a factor of 3 due to the corresponding reduction of QW's. The shift of the absorption edge becomes small at a fixed applied electric field as the well thickness is decreased. Therefore, the 370 \AA detuning in our integrated device is considered to be much larger effectively than the 400 \AA in the 100 \AA MQW phase modulator, resulting in a further reduction of intensity modulation. Of course, we expect smaller QCSE for the 50 \AA MQW's, and

hence smaller refractive index change. However, this may not necessarily be true due to the following reasons; 1) the exciton absorption peaks are much stronger in thin QWs than in thick QW's because of close spatial binding of excitons (~ 1.5 times stronger heavy-hole exciton absorption for 50 Å QW's than 100 Å QW's), 2) the exciton absorption peak for thin QW's maintains its shape with less broadening during the quantum-confined Stark shift, and 3) the maximum applied electric field is much higher in thin QW's (~ 3 times higher in 50 Å than 100 Å QW's). Note that the phase shift in MQW structures mainly depends on the QEO effect associated with the QCSE, and hence the phase shift efficiency increases quadratically as the applied bias voltage increases (Fig.6.8). Therefore, very high phase shift efficiencies are expected in our integrated device with significantly reduced intensity modulation.

CHAPTER SEVEN SUMMARY AND RECOMMENDATION

7.1. Summary

The objective of this dissertation is to develop novel GaAs/AlGaAs double-heterostructures (DH) and multiple quantum-well (MQW) structures for high-speed laser-phase modulator integrated devices. For this purpose, detailed theoretical analyses for the refractive index change under the reverse-biased and forward-biased conditions have been accomplished in chapters three through six, following the review of the absorption and refractive index in GaAs bulk and quantum-well structures in chapter two. In addition, experimental demonstrations for DH, MQW, and single quantum-well (SQW) devices utilizing the refractive index and absorption changes have been described in chapters five and six. Accomplishments achieved in the course of this study are summarized in the following.

For the reduction of linewidth in diode lasers:

1. Development of an analytical model for calculating the linewidth enhancement factor - Employing new expressions, capable of describing sufficiently both the absorption spectra with and without current injection, and also integrable in the Kramers-Kronig dispersion relation, we have demonstrated that analytical estimation for the linewidth enhancement factor is possible.

2. Theoretical demonstration of the laser geometry dependence of the linewidth enhancement factor and hence linewidth, in a quantitative manner - The geometrical parameters include active layer thickness, laser length, and facet reflectivity. Excluding unreal assumptions such as parabolic bands and Fermi levels, the results show very practical magnitudes of the linewidth enhancement factor at actual lasing wavelengths.
3. Clarification of the wide distribution of experimental linewidth enhancement factors measured in various diode lasers with different laser geometries, different lateral waveguiding, and different AlAs mole fractions in the active layers - Thorough comparisons of experimental and theoretical data have enabled us to predict the dependence of the linewidth enhancement factor on the laser type and the lasing wavelength.
4. Development of practical methods for the reduction of laser linewidth - The narrowing of the active layer has been found more efficient for the linewidth reduction than the other methods known to date, viz., longer laser length, high reflectivity coatings on facets and use of an external cavity. The results show that the linewidth enhancement factor reduces by a factor of 3 - 3.5 with a reduction of active layer thickness from 0.2 to 0.05 μm , which corresponds to a reduction of linewidth by an order of magnitude.

For the optimization of GaAs/AlGaAs DH waveguide phase modulator:

1. Development of the theory for the refractive index change induced in a p-n junction under the reverse bias - There are four physical phenomena involved in the refractive index change. Two effects are

associated with the depletion of free carriers - the free carrier plasma (PL) effect, and the bandgap shift (BS) consisting of the band-filling (BF) and bandgap shrinkage (BGS). The other two are caused by the development of electric field in the depletion region - the linear electro-optic (LEO) and quadratic electro-optic (QEO) effects.

- 2 Demonstration of a novel high speed, high efficiency P-p-i-n-N DH waveguide phase modulator - The P-p-i-n-N modulators utilizing the higher-order (QEO and BS) effects in GaAs, have been fabricated, and characterized by using a Mach-Zehnder interferometer, producing very high phase shift efficiencies (82 and 37.5 °/V-mm at $\lambda = 1.06$ and 1.3 μm , respectively, for the TE_0 mode). These are very close to the highest efficiencies reported, but with low junction and dynamic capacitances unattainable previously in high-efficiency phase modulators.
3. Development of a detailed theoretical analysis for the phase shift in the P-p-i-n-N waveguide phase modulator - The analysis includes calculations of refractive index changes due to the four physical effects, depletion region, electric field distributions, optical modal field, and derivation of combined equations for the phase shift calculation of the propagating mode. Excellent agreements between experimental and theoretical results for the phase shift dependences on wavelength, carrier concentration, and intrinsic layer thickness, have been obtained.
4. Optimization of DH waveguide phase modulators for high-speed operations - Since the P-p-i-n-N phase modulator can be reduced to either recently reported p-n junction or P-i-N phase modulator depending on the intrinsic layer thickness and carrier concentration,

the detailed analysis for the P-p-i-n-N phase modulator not only provides performance comparisons of the three types of high-efficiency modulators, but also facilitates optimization of DH phase modulators in terms of high-speed operation. Highest cut-off frequency of ~ 4 GHz was estimated for the P-p-i-n-N phase modulator with an intrinsic layer thickness of $0.3 \mu\text{m}$ for the total GaAs thickness of $0.35 \mu\text{m}$.

5. Presentation of design criteria for high-speed DH phase modulator - Using a thick intrinsic GaAs layer available for a given structure, it is necessary to confine depletion region and hence electric field within GaAs active layers for utilizing the higher-order effects in GaAs rather than AlGaAs layers, and preventing depletion edges from approaching carrier-accumulation regions at heterointerfaces. For this purpose, p- and n-GaAs were inserted between the intrinsic layer and the AlGaAs cladding layers.

For the integration of laser and phase modulator:

1. Development of novel MQW structure for SQW laser-MQW phase modulator integrated devices - The structure contains a SQW and MQW's with different well thicknesses in the active region. The SQW and MQW's are the active layers in the laser and phase modulator, respectively. Angled reactive ion etching (ARIE) and Impurity-induced disordering (IID) are used to fabricate asymmetric SQW laser in the laser section and tapered waveguide between the laser and modulator sections. The main advantage of this novel integration scheme is that it does not require complicated growth and fabrication techniques, and therefore offers an alternative for laser-modulator integration.

2. Demonstration of asymmetric SQW lasers with low threshold current density - Prior to integration, separate SQW lasers and MQW modulators have been fabricated and characterized. First, asymmetric 100 \AA GaAs/AlGaAs SQW lasers, whose structure is similar to the laser section in the proposed integrated device, were grown by MOCVD at the University of Florida, and fabricated with 100 \mu m - contact stripes. A very low threshold current density of $\sim 0.577\text{ KA/cm}^2$ was obtained despite the asymmetric waveguide structure, i.e., poor modal confinement in the SQW. A typical linewidth was around 20 \AA at $\lambda = 0.854\text{ \mu m}$.
3. Fabrication and characterization of GaAs/AlGaAs MQW transverse electroabsorption modulators with various well thicknesses - The purpose of the intensity modulation is twofold: First, the positions of the exciton resonance peaks can be investigated to determine suitable well sizes for SQW and MQW's to satisfy the wavelength detuning requirement. Second, absorption changes due to the quantum-confined Stark effect (QCSE) can give preliminary estimations for the phase shift modulation via the Kramers-Kronig relation. 50 \AA and 100 \AA GaAs/AlGaAs MQW structures were grown by MOCVD at University of Florida for the intensity modulators. Experimental results show clear room temperature heavy-hole exciton peaks at 0.847 \mu m and 0.817 \mu m for 100 \AA and 50 \AA MQW structures, respectively.
4. Design of GaAs/AlGaAs MQW waveguide phase modulator with 50 \AA MQW's in the active layer - Important parameters for phase modulation utilizing MQW phase modulators, viz., the phase shift efficiency and the chirp factor have been discussed as a function of well thickness, number of QW's, and operating bias voltage. 50 \AA thin QW's

are needed for our integrated devices in order to provide not only high phase shift efficiency but also significantly large chirp factor.

5. Discussion of integration techniques necessary for the SQW laser-MQW modulator integrated devices - This includes ARIE and IID techniques for defining laser section and optical coupling region as well as electrical isolation between laser and modulator sections.

7.2. Recommendation for Further Study

In this section, we briefly describe the research which remains to be performed for the completion of the laser-phase modulator integration at the Photonics Research Laboratory, and applications of the design concepts developed in this study to devices in other material systems. Finally, we point out the future research which should be conducted to achieve practical laser-phase modulator integrated devices.

7.2.1. Completion of the SQW Laser-MQW Phase Modulator Integration

As mentioned in the previous sections, the ARIE technique is one of the most important processes in our integration schemes to provide efficient optical coupling as well as good electrical isolation. Small coupling efficiencies are desirable for stable lasing condition, but on the other hand, one of the merits of the integrated devices is large coupling efficiencies. Hence, theoretical work for optimizing the coupling efficiency is needed.

At the Photonics Research Laboratory, the IID research is currently being done by diffusion and ion implantation of impurities viz., zinc for the p-type impurity, silicon for the n-type impurity, and fluorine (F) for the

neutral impurity. Upon completion of this study, we can expect to make significant progress toward integration. Zn and Si IID's would enable us to fabricate low threshold single-mode SQW lasers by providing efficient injection of the carriers and lateral confinement of the light. Moreover, a recent report has shown that IID using electrically neutral impurities such as F and boron (B) is extremely useful for the formation of low-loss MQW waveguides [One89]. Not only the blue-shift of the absorption edge of MQW waveguide but also no addition of free carriers (which is not the case of IID by dopant impurities) are involved resulting in a reduction of the absorption loss.

Characterization of MQW intensity modulators is more desirable in the waveguide structure rather than the transverse structure, provided that a tunable light source with sufficient power is available. As discussed in section 2.4, MQW waveguide structure has several advantages for the measurement of the QCSE: a) Both the TE and TM polarizations, showing remarkably different excitonic features, can be used, b) much stronger electric fields can be applied and c) broadening of excitonic resonances due to inhomogeneous electric field across the MQW can be significantly reduced. This measurement will be conducted in our laboratory by using a Ti:sapphire tunable laser.

Careful characterization of MQW phase modulators involving both the 100 \AA SQW and 50 \AA MQW's is necessary since the results will be the combined output from the two different QW's. Therefore, characterization of separate MQW phase modulators with either 100 \AA or 50 \AA well size, in terms of the phase shift efficiency and the absorption loss should precede. By comparisons with the QCSE results obtained for the MQW intensity

modulators, these preliminary results enable us to optimize the MQW structures for the integrated devices experimentally.

7.2.2. Applications to Other Material Systems

As seen through this study, all the theory and design concepts have been developed for GaAs/AlGaAs DH and MQW structures. However, physical mechanisms for carrier movements as a function of bias voltage and optical excitation are essentially the same as those in other semiconductors, especially, III-V and II-VI material systems with direct-bandgaps. The only differences are the carrier effective masses and bandgap energies.

The most useful material systems for application in the 1.3 - 1.5 μm wavelength range are InGaAsP/InP, InGaAs/InP, and InGaAlAs/InP, and InGaAs/InAlAs. While lasers made of these materials are well developed due to their optical communication applications, results on the development of 1.3 - 1.5 μm DH phase modulators have been very poor. Phase shift efficiencies of 1.4 - 7 $^{\circ}/\text{V}\cdot\text{mm}$ [Don85b, Tak89b] have been reported, which are much smaller than those discussed in chapter five. It would be very interesting to use the P-p-i-n-N structure in these material systems. On the other hand, InGaAs/InAlAs MQW phase modulators have been reported with high efficiencies of 66 - 240 $^{\circ}/\text{V}\cdot\text{mm}$ at $\lambda = 1.5 - 1.6 \mu\text{m}$ [Wak87, Wak89] and monolithic integration of InGaAs/InGaAsP MQW laser-phase modulator [Kor88] has also been reported. Recent regrowth techniques have been applied to these materials. Therefore, our proposed integration scheme for these materials along with the well-developed regrowth techniques will not be too difficult to implement; monolithic

integration of three or four devices resulting in low fiber-device insertion loss should be possible. The examples of such integrated devices include laser-phase modulator -tapered waveguide and laser-direction coupler (or interferometers)-tapered waveguide. These monolithically integrated devices are not available at present but are expected to be developed sooner or later along with the progress in regrowth techniques.

Assuming that selective regrowth techniques are developed in near future, AlGaAs active layers are needed to be characterized in the same way as GaAs active layers since the active layers of other optical devices, except the laser and detector, must be larger bandgap materials than GaAs (or Al_xGaAs with $x < 0.1$). This study will give us a complete set of design parameters for GaAs/AlGaAs integrated devices.

Another application is for GaAs/Si materials. Recently, Schottky-barrier ridge-waveguide GaAs/AlGaAs phase modulators on Si substrates grown by MOCVD [Kim89] and MBE [Kim90] have been demonstrated. Higher phase shift efficiencies of $3.5 - 4.7 \text{ }^{\circ}/\text{V}\cdot\text{mm}$ compared to those ($\sim 1.8 \text{ }^{\circ}/\text{V}\cdot\text{mm}$) measured for similar device structures grown on GaAs substrates [Wa87b] have been achieved. The reason for the efficiency improvements is not been well understood and is currently being investigated experimentally as well as theoretically. However, the phase shift efficiencies of the above Schottky- barrier modulators are so small that it is very difficult to distinguish the changes of the phase shift efficiencies due to external perturbations, such as variations of waveguide geometries, and potential stress effects. Therefore, utilization of high-efficiency P-p-i-n-N GaAs/Si phase modulators, would help us identify the physical mechanisms leading to the improved phase shift efficiencies in the GaAs/Si

phase modulators as well as demonstrate higher efficiency GaAs/Si phase modulators.

7.2.3. Future Study for Laser-Modulator Integration

Recently, lasers monolithically integrated with tapered waveguides have been demonstrated [Koc90], by using complicated stacks of QW's with different well sizes. In chapter six, we have also proposed a novel ARIE-MQW structure for SQW laser-MQW phase modulator integration utilizing different well sizes. It is believed that future integrated devices will employ various materials and well sizes of QW's in their active layers to produce versatile functions. Therefore, the optical properties of the QW structures with various well sizes are needed to be characterized. The QCSE's as a function of the well size have already been reported for GaAs/AlGaAs QW structures [Whi88]. However, the change of the electroabsorption associated with the QCSE variations as a function of the well size, which should play the principal role in the future integrated devices, has not been reported. In chapter six, we have discussed the electrorefraction change in a qualitative manner based on the reported QCSE results. Therefore, experimental and theoretical investigations for the electrorefraction change are essential for the successful implementation of our integration scheme and the development of more useful integrated devices.

The tapered waveguides mentioned above were made by regrowth techniques consisting of a series of etching-stop layer growth, etching, and subsequent regrowth, removing higher-index layers (the active and cladding layers of the laser) gradually and guiding the light into the larger guiding region along the waveguide. This tapered guiding scheme as well

as lateral waveguiding can be obtained by applying IID techniques on as-grown MQW structures including all the necessary layers for lasers, modulators, and waveguides. Necessary impurities (Si, Zn, and F) for the specified areas should be implanted with appropriate depths, and thermal annealing be performed during an annealing time optimized for the impurities. This scheme is very simple, provided that the IID techniques are well understood and fully developed. It is believed that this scheme should play a major role in the practical integration schemes of the future.

REFERENCES

- [Ada85] S. Adachi, "GaAs, AlAs and $Al_xGa_{1-x}As$: Material parameters for use in research and device applications," *J. Appl. Phys.*, vol. 58, pp. R1-R29, 1985.
- [Afr74] M. A. Afromowitz, "Refractive index of $Ga_{1-x}Al_xAs$," *Solid State Commun.*, vol. 15, pp. 59-63, 1974.
- [Aji87] A. Ajisawa, M. Fujiwara, J. Shimizu, M. Uchida, and Y. Ohta, "Monolithically integrated optical gate 2x2 switch using GaAs/AlGaAs multiple quantum well structures," *Electron. Lett.*, vol. 23, pp. 1121-1122, 1987.
- [Alf82] R. C. Alferness, "Waveguide electrooptic modulator," *IEEE Trans. Microwave Tech.*, vol. MTT-30, pp. 1121-1137, 1982.
- [Alp87a] A. Alping and L. A. Coldren, "Electrorefraction in GaAs and InGaAsP and its application to phase modulators," *J. Appl. Phys.*, vol. 61, pp. 2430-2433, 1987.
- [Alp87b] A. Alping, X. S. Wu, and L. A. Coldren, "Wavelength dependence of high-performance AlGaAs/GaAs waveguide phase modulators," *Electron. Lett.*, vol. 23, pp. 93-95, 1987.
- [Ara86a] Y. Arakawa, A. Larsson, J. Paslaski, and A. Yariv, "Active Q switching in a GaAs/AlGaAs multiquantum well laser with an intracavity monolithic loss modulator," *Appl. Phys. Lett.*, vol. 48, pp. 561-563, 1986.
- [Ara85] Y. Arakawa and A. Yariv, "Fermi energy dependence of linewidth enhancement factor of GaAlAs buried heterostructures lasers," *Appl. Phys. Lett.*, vol. 47, pp. 905-907, 1985.
- [Ara86b] Y. Arakawa and A. Yariv, "Quantum well lasers - gain, spectra, dynamics," *IEEE J. Quantum Electron.*, vol. QE-22, pp. 1887-1899, 1986.
- [Bey81] W. H. Beyer, Ed., *CRC Standard Mathematical Tables*, Boca Raton, FL: CRC, 1981, pp. 421-423.
- [Bla82] J. S. Blakemore, "Semiconducting and other major properties of gallium arsenide," *J. Appl. Phys.*, vol. 53, pp. R123-R181, 1982.

- [Bot79] D. Botez, "Optimal cavity design for low-threshold-current-density operation of double-heterojunction diode lasers," *Appl. Phys. Lett.*, vol. 35, pp. 57-60, 1979.
- [Boy72] J. T. Boyd, "Theory of parametric oscillation phase matched in GaAs thin-film waveguides," *IEEE J. Quantum Electron.*, vol. QE-8, pp. 788-796, 1972.
- [Bra62] R. Braunstein and E. O. Kane, "The valence band structure of the III-V compounds," *J. Phys. Chem. Solids*, vol. 23, pp. 1423-1431, 1962.
- [Bur54] E. Burstein, "Anomalous optical absorption limit in InSb," *Phys. Rev.*, vol. 93, pp. 632-633, 1954.
- [But82] J. K. Butler and D. Botez, "Spatial mode discrimination and control in high-power single-mode constricted double-heterojunction large-optical-cavity diode lasers," *Appl. Phys. Lett.*, vol. 41, pp. 1118-1120, 1982.
- [Cal63] J. Callaway, "Optical absorption in an electric field," *Phys. Rev.*, vol. 130, pp. 549-553, 1963.
- [Cam75] J. C. Campbell, F. A. Blum, and D. W. Shaw, "GaAs electro-optic channel waveguide modulator," *Appl. Phys. Lett.*, vol. 26, pp. 640-642, 1975.
- [Cas78] H. C. Casey, Jr. and M. B. Panish, *Heterostructure Lasers, Part A*, New York: Academic, 1978, pp. 194-253.
- [Cas74] H. C. Casey, Jr., D. D. Sell, and M. B. Panish, "Refractive index of $\text{Al}_x\text{Ga}_{1-x}\text{As}$ between 1.2 and 1.8 eV," *Appl. Phys. Lett.*, vol. 24, pp. 63-65, 1974.
- [Cas75] H. C. Casey, Jr., D. D. Sell, and K. W. Wecht, "Concentration dependence of the absorption coefficient for n- and p-type GaAs between 1.3 and 1.6 eV," *J. Appl. Phys.*, vol. 46, pp. 250-257, 1975.
- [Cas76] H. C. Casey, Jr. and F. Stern, "Concentration-dependent absorption and spontaneous emission of heavily doped GaAs," *J. Appl. Phys.*, vol. 47, pp. 631-643, 1976.
- [Che88] R. Chen and C. S. Tsai, "GaAs-GaAlAs heterostructure single-mode channel-waveguide cutoff modulator and modulator array," *IEEE J. Quantum Electron.*, vol. QE-23, pp. 2205-2209, 1988.
- [Che87] T. R. Chen, K. Utaka, Y. H. Zhuang, Y. Y. Liu, and A. Yariv, "Vertical integration of an InGaAsP/InP heterojunction bipolar

transistor and a double heterostructure laser," *Appl. Phys. Lett.*, vol. 50, pp. 874-876, 1987.

[Cin87] P. Cingino, F. Genova, C. Rigo, C. Cacciatore, and A. Satano, "Monolithic integrated InGaAlAs/InP ridge waveguide photodiodes for 1.55 μm operation grown by molecular beam epitaxy," *Appl. Phys. Lett.*, vol. 50, pp. 1515-1517, 1987.

[Col87] L. A. Coldren, J. G. Mendoza-Alvarez, and R. H. Yan, "Design of optimized high-speed depletion-edge-translation optical waveguide modulators in III-V semiconductors," *Appl. Phys. Lett.*, vol. 51, pp. 792-794, 1987.

[Dec90] B. C. DECooman, G. L. A. Van der Hofstad, P. I. Kuindersma, W. Scheepers, J. A. M. Cnoops, and I. A. F. Baele, "Efficient Linewidth reduction in conventional 1.5 μm laser diodes by integration to a weakly coupled InGaAsP Bragg waveguide with low optical losses," *IEEE Photon. Technol. Lett.*, vol. 2, pp. 111-113, 1990.

[Don85a] J. P. Donnelly, N. L. Demeo, G. A. Ferrante, and K. B. Nichols, "A high-frequency GaAs optical guided-wave electrooptic interferometric modulator," *IEEE J. Quantum Electron.*, vol. QE-21, pp. 18-21, 1985.

[Don85b] J. P. Donnelly, N. L. Demeo, F. J. Leonberger, S. H. Groves, P. Vohl, and F. J. O'Donnell, "Single-mode optical waveguides and phase modulators in the InP material system," *IEEE J. Quantum Electron.*, vol. QE-21, pp. 1147-1150, 1985.

[Epl87] J. E. Epler, R. D. Burnham, R. L. Thornton, and T. L. Paoli, "Low threshold buried heterostructure quantum well diode lasers by laser-assisted disordering," *Appl. Phys. Lett.*, vol. 50, pp. 1637-1693, 1987.

[Fai90] J. Faist and F. K. Reinhart, "Phase modulation in AlGaAs/GaAs double heterostructures. Part I: Theory and Part II: Experiment," Submitted to *J. Appl. Phys.* 1990.

[Fai87a] J. Faist, F. K. Reinhart and D. Martin, "Comparison of phase modulation of GaAs/AlGaAs double heterostructures," *Electron. Lett.*, vol. 23, pp. 1391-1392, 1987.

[Fai87b] J. Faist, F. K. Reinhart, D. Martin, and E. Tuncel, "Orientation dependence of the phase modulation in a p-n junction GaAs/AlGaAs waveguide," *Appl. Phys. Lett.*, vol. 50, pp. 68-70, 1987.

- [Fer71] R. E. Fern and A. Onton, "Refractive index of AlAs," *J. Appl. Phys.*, vol. 42, pp. 3499-3450, 1971.
- [Fle81] M. W. Fleming and A. Mooradian, "Fundamental line broadening of single-mode (GaAl)As diode lasers," *Appl. Phys. Lett.*, vol. 38, pp. 511-513, 1981.
- [Fur85] K. Furuya, "Dependence of linewidth enhancement factor α on waveguide structure in semiconductor lasers," *Electron. Lett.*, vol. 21, pp. 200-201, 1985.
- [Gli86] M. Glick, F. K. Reinhart, G. Weimann, and W. Schlapp, "Quadratic electro-optic light modulation in a GaAs/AlGaAs multiquantum well heterostructure near the excitonic gap," *Appl. Phys. Lett.*, vol. 48, pp. 989-991, 1986.
- [Gos86] A. C. Gossard, "Growth of microstructures by molecular beam epitaxy," *IEEE J. Quantum Electron.*, vol. QE-22, pp. 1649-1655, 1986.
- [Har83] C. Harder, K. Vahala, and A. Yariv, "Measurement of the linewidth enhancement factor α of semiconductor lasers," *Appl. Phys. Lett.*, vol. 42, pp. 328-330, 1983.
- [Hau84] H. A. Haus, *Waves and Fields in Optoelectronics*. Englewood Cliffs, NJ: Prentice-Hall, 1984, pp. 189.
- [Hau88] T. R. Hausken, T. C. Huang, K. W. Lee, R. J. Simes, N. Dagli, and L. A. Coldren, "Phase modulation in impurity-induced-disordered AlGaAs/GaAs quantum-well and double-heterostructure waveguides," *Tech. Dig., Conf. on Integrated and Guided-Wave Optics (IGWO)*, Santa Fe, New Mexico, March 1988, paper MA3.
- [Hau89] T. Hausken, K. W. Lee, R. J. Simes, R. H. Yan, and L. A. Coldren, "Dependence of chirp on the number of quantum wells in GaAs/AlGaAs waveguide modulators," *Tech. Dig., Conf. on Integrated and Guided-Wave Optics (IGWO)*, Houston, Texas, Feb. 1989, paper WAA2.
- [Hen83] I. D. Henning and J. V. Collins, "Measurements of the semiconductor laser linewidth broadening factor," *Electron. Lett.*, vol. 19, pp. 927-929, 1983.
- [Hen82] C. H. Henry, "Theory of the linewidth of semiconductor lasers," *IEEE J. Quantum Electron.*, vol. QE-18, pp. 259-264, 1982.
- [Hen81] C. H. Henry, R. A. Logan, and K. A. Bertness, "Spectral dependence of the change in refractive index due to carrier

injection in GaAs lasers," *J. Appl. Phys.*, vol. 52, pp. 4457-4461, 1981.

- [Hen80] C. H. Henry, R. A. Logan, and F. R. Merritt, "Measurement of gain and absorption spectra in AlGaAs buried heterostructure lasers," *J. Appl. Phys.*, vol. 51, pp. 3042-3050, 1980.
- [Hil64] D. E. Hill, "Infrared transmission and fluorescence of doped Gallium Arsenide," *Phys. Rev.*, vol. 133, pp. A866-A872, 1964.
- [Hou84] A. J. N. Houghton, P. M. Rodgers, and D. A. Andrews, "High-performance GaAs-GaAlAs phase modulators for PSK fibre systems," *Electron. Lett.*, vol. 20, pp. 479-481, 1984.
- [Hwa69] C. J. Hwang, "Optical properties of n-type GaAs.- I. Determination of hole diffusion length from optical absorption and photoluminescence measurements," *J. Appl. Phys.*, vol. 40, pp. 3731-3739, 1969.
- [Ino89] H. Inoue, "InP-based optical switch array exploiting carrier-induced refractive index change," *Tech. Dig., Conf. on Integrated Optics and Optical Fiber Communications (IOOC)*, Kobe, Japan, July 1989, paper 21A3-2.
- [Ish89] K. Ishida and H. Inoue, "InP-based carrier injection optical switch array," *Tech. Dig., Conf. on Integrated and Guided-Wave Optics (IGWO)*, Houston, Texas, Feb. 1989, paper TuCC1.
- [Joy78] W. B. Joyce, "Analytic approximations for the Fermi energy in (Al,Ga)As," *Appl. Phys. Lett.*, vol. 32, pp. 680-681, 1978.
- [Kap87] E. Kapon, N. G. Stoffel, E. A. Dobisz, and R. Bhat, "GaAs/AlGaAs channel waveguide made by impurity-induced superlattice disordering," *Tech. Dig., Conf. on Lasers and Electro-optics (CLEO)*, 1987, paper WQ4.
- [Kap88] E Kapon, N. G. Stoffel, E. A. Dobisz, and R Bhat, "Birefringent channel waveguide defined by impurity induced disordering," *Appl. Phys. Lett.*, vol. 52, pp. 351-353, 1988.
- [Kaw87] Y. Kawamura, K. Wakita, Y. Yoshikuni, Y. Itaya, and H. Asahi, "Monolithic integration of a DFB laser and a MQW optical modulator in the 1.5 μm wavelength range," *IEEE J. Quantum Electron.*, vol. QE-23, pp. 915-918, 1987.
- [Kik83] K. Kikuchi and T. Okoshi, "Measurement of spectra of and correlation between FM and AM noises in GaAlAs lasers," *Electron. Lett.*, vol. 19, pp. 812-813, 1983.

- [Kik85] K. Kikuchi and T. Okoshi, "Estimation of linewidth enhancement factor of AlGaAs lasers by correlation measurement between AM and FM noises," *IEEE J. Quantum Electron.*, vol. QE-21, pp. 669-673, 1985.
- [Kim89] Y. S. Kim, S. S. Lee, and R. V. Ramaswamy, "Reverse biased GaAs/AlGaAs phase modulator grown on Si substrate by metalorganic chemical vapor deposition," *Conf. Dig., Inter. Meet. on Advanced Processing and Characterization Technologies (APCT)*, Tokyo, Japan, Oct. 1989, paper J-1.
- [Kim90] Y. S. Kim, S. S. Lee, R. V. Ramaswamy, S. Sakai, Y. C. Kao, and H. Shichijo, "Low loss GaAs/AlGaAs optical waveguides and phase modulators on silicon substrate grown by molecular beam epitaxy," *Appl. Phys. Lett.*, vol. 56, pp. 802-804, 1990
- [Kir77] P. A. Kirkby, A. R. Goodwin, G. H. B. Thompson, and P. R. Selway, "Observation of self-focusing in stripe geometry semiconductor lasers and the development of a comprehensive model of their operation," *IEEE J. Quantum Electron.*, vol. QE-13, pp. 705-719, 1977.
- [Kis82] K. Kishino, S. Aoki, and Y. Suematsu, "Wavelength variation of 1.6 μ m wavelength buried heterostructure GaInAsP/InP lasers due to direct modulation," *IEEE J. Quantum Electron.*, vol. QE-18, pp. 343-351, 1982.
- [Koc90] T. L. Koch, U. Koren, G. Eisenstein, M. G. Young, M. Oron, C. R. Giles, and B. I. Miller, "Tapered waveguide InGaAs/InGaAsP multiple-quantum-well lasers," *IEEE Photon. Technol. Lett.*, vol. 2, pp. 88-90, 1990.
- [Kor88] U. Koren, T. L. Koch, B. I. Miller, and A. Shahar, "InGaAs/InGaAsP distributed feedback quantum well laser with an intracavity phase modulator," *Appl. Phys. Lett.*, vol. 53, pp. 2132-2134, 1988.
- [Kor87] S. K. Korotky, G. Eisenstein, R. S. Tucker, J. J. Veselka, and G. Raybon, "Optical intensity modulation to 40 GHz using a waveguide electro-optic switch," *Appl. Phys. Lett.*, vol. 50, pp. 1631-1633, 1987.
- [Kud62] I. Kudman and T. Seidel, "Absorption edge in degenerate p-type GaAs," *J. Appl. Phys.*, vol. 33, pp. 771-773, 1962.
- [Lan79] R. Lang, "Lateral transverse mode instability and its stabilization in stripe geometry injection lasers," *IEEE J. Quantum Electron.*, vol. QE-15, pp. 718-726, 1979.

- [Lee89a] S. S. Lee, L. Figueroa, and R. V. Ramaswamy, "Variations of linewidth enhancement factor and linewidth as a function of laser geometry in (AlGa)As lasers," *IEEE J. Quantum Electron.*, vol. QE-25, pp. 862-870, 1989.
- [Lee89b] S. S. Lee, Y. S. Kim, R. V. Ramaswamy, and V. S. Sundaram, "Highly efficient separate-confinement PpinN GaAs/AlGaAs waveguide phase modulator," *Appl. Phys. Lett.*, vol. 55, pp. 1865-1867, 1989.
- [Lee90] S. S. Lee and R. V. Ramaswamy, "Analysis and optimization of high-speed GaAs/AlGaAs double-heterostructure waveguide phase modulators," submitted to *IEEE J. Quantum Electron.*, 1990.
- [Len84] W. Lenth, "Linewidth measurement of a (GaAl)As diode laser with a high reflectivity coating," *Appl. Phys. Lett.*, vol. 44, pp. 283-285, 1984.
- [Lio89] K. Y. Liou, U. Koren, S. Chandrasekhar, T. L. Koch, A. Shahar, C. A. Burrus, and R. P. Gnall, "Monolithically integrated 1.5 μm DFB laser with Y-branching waveguide and a monitoring photodetector," *Tech. Dig., Conf. on Integrated and Guided-Wave Optics (IGWO)*, Houston, Texas, Feb. 1989, paper TuCC2.
- [Lud85] M. J. Ludowise, "Metalorganic chemical vapor deposition of III-V semiconductors," *J. Appl. Phys.*, vol. 58, pp. R31-R55, 1985.
- [Man83] J. Manning, R. Olshansky, and C. B. Su, "The carrier-induced index change in AlGaAs and 1.3 μm InGaAsP diode lasers," *IEEE J. Quantum Electron.*, vol. QE-19, pp. 1525-1530, 1983.
- [Mar64] D. T. F. Marple, "Refractive index of GaAs," *J. Appl. Phys.*, vol. 35, pp. 1241-1242, 1964.
- [Mar85] W. K. Marshall and J. Katz, "Waveguide PIN junction electrooptic phase modulators: theoretical analysis and design criteria," *Appl. Opt.*, vol. 24, pp. 1996-2000, 1985.
- [Men88] G. Mendoza-Alvarez, L. A. Coldren, A. Alping, R. H. Yan, T. Hausken, K. Lee, and K. Pedrotti, "Analysis of depletion edge translation lightwave modulators," *J. Lightwave Technol.*, vol. LT-6, pp. 793-808, 1988.
- [Men80] J. G. Mendoza-Alvarez, F. D. Nunes, and N. B. Patel, "Refractive index dependence on free carriers for GaAs," *J. Appl. Phys.*, vol. 51, pp. 4365-4367, 1980.

- [Men87] J. G. Mendoza-Alvarez, R. H. Yan, and L. A. Coldren, "Contribution of the band-filling effect to the effective refractive-index change in double-heterostructure GaAs/AlGaAs phase modulators," *J. Appl. Phys.*, vol. 62, pp. 4548-4553, 1987.
- [Mil84] D. B. A. Miller, C. S. Chemla, T. C. Damen, A. C. Gossard, W. Wiegmann, T. H. Wood, and C. A. Burrus, "Band-edge electroabsorption in quantum well structure: The quantum-confined Stark effect," *Phys. Rev. Lett.*, vol. 53, pp. 2173-2176, 1984.
- [Mil85] D. B. A. Miller, C. S. Chemla, T. C. Damen, A. C. Gossard, W. Wiegmann, T. H. Wood, and C. A. Burrus, "Electric field dependence of optical absorption near the band gap of quantum-well structures," *Phys. Rev. B*, vol. 32, pp. 1043-1060, 1985.
- [Mos61] T. S. Moss, "Optical absorption edge in GaAs and its dependence on electrical field," *J. Appl. Phys.*, vol. 32, pp. 2136-2139, 1961.
- [Nam61] S. Namba, "Electro-optical effect of zincblende," *J. Opt. Soc. Ame.*, vol. 51, pp. 148-151, 1961.
- [Nas73] F. R. Nash, "Mode guidance parallel to the junction plane of double-heterostructure GaAs lasers," *J. Appl. Phys.*, vol. 44, pp. 4696-4707, 1973.
- [Nod87] S. Noda, K. Kojima, K. Kyuma, K. Hamanaka, and T. Nakayama, "Reduction of spectral linewidth in AlGaAs/GaAs distributed feedback lasers by a multiple quantum well structure," *Appl. Phys. Lett.*, vol. 50, pp. 863-865, 1987.
- [Nod86] Y. Noda, M. Suzuki, Y. Kushino, and S. Akiba, "High-speed electroabsorption modulator with strip-loaded GaInAsP planar waveguide," *IEEE J. Lightwave Technol.*, vol. LT-4, pp. 1445-1453, 1986.
- [Oga85] N. Ogasawara, R. Ito, and R. Morita, "Linewidth enhancement factor in GaAs/AlGaAs multi-quantum-well lasers," *Japan. J. Appl. Phys.*, vol. 24, pp. L519-L521, 1985.
- [Oga84] N. Ogasawara, R. Ito, K. Tone, and N. Nakae, "Dispersion of the linewidth enhancement factor in semiconductor injection lasers," *Japan J. Appl. Phys.*, vol. 23, pp. L518-L520, 1984.
- [One89] M. O'Neill, J. H. Marsh, R. M. DeLaRue, J. Lamb, J. S. Roberts, and C. Jeynes, "MQW optical waveguides with large absorption-edge blue-shift produced by boron and fluorine impurity induced disordering," *Tech. Dig., Conf. on Integrated Optics and Optical Fiber Communication (IOOC)*, Kobe, Japan, July 1989, paper 20B2-18.

- [Osi87] M. Osinski and J. Buus, "Linewidth broadening factor in semiconductor lasers - An overview," *IEEE J. Quantum Electron.*, vol. QE-23, pp. 9-29, 1987.
- [Pan71] J. I. Pankove, *Optical Processes in Semiconductors*, New York: Dover Publications, 1971, pp. 75.
- [Pin85] M. R. Pinto, C. S. Rafferty, H. R. Yeager, and R. W. Dutton, "PISCES- IIB: User Manual," Stanford Electron. Lab., Stanford Univ., Palo Alto, CA, 1985.
- [Rei72] F. K. Reinhart and B. I. Miller, "Efficient GaAs-AlGaAs double heterostructure light modulators," *Appl. Phys. Lett.*, vol. 20, pp. 36-38, 1972.
- [Sak86] S. Sakano, H. Inoue, H. Nakamura, T. Katsuyama, and H. Maysumura, "InGaAsP/InP monolithic integrated circuit with lasers and an optical switch," *Electron. Lett.*, vol. 20, pp. 594-596, 1986.
- [Sal83] H. W. M. Salemink and J. W. M. Biesterbos, "Optical stability of narrow stripe, proton-isolated AlGaAs double heterostructure lasers with gain guiding," *Appl. Phys. Lett.*, vol. 43, pp. 434-436, 1983.
- [Sch83] R. Schimpe and W. Harth, "Theory of FM noise of single-mode injection lasers," *Electron. Lett.*, vol. 19, pp. 136-137, 1983.
- [Sch84] R. Schimpe, B. Stegmüller, and W. Harth, "FM noise of index-guided GaAlAs diode lasers," *Electron. Lett.*, vol. 20, pp. 206-208, 1984.
- [Sch89] A. Schremer and C. L. Tang, "Electro-optically tunable external-cavity semiconductor lasers," *Conf. Dig., Conf. on IEEE Lasers and Electro-Optics Annual Meeting (LEO)*, Orlando, Florida, October 1989, paper OE4.3.
- [Sel74] D. D. Sell, H. C. Casey Jr., and K. W. Wecht, "Concentration dependence of the refractive index for n- and p-type GaAs between 1.2 and 1.8 eV," *J. Appl. Phys.*, vol. 45, pp. 2650-2657, 1974.
- [Spi59] W. G. Spitzer and J. M. Whelan, "Infrared absorption and electron effective mass in n-type gallium arsenide," *Phys. Rev.*, vol. 114, pp. 59-63, 1959.
- [Ste64] F. Stern, "Dispersion of the index of refraction near the absorption edge of semiconductors," *Phys. Rev.*, vol. 133, pp. A1653-A1664, 1964.

- [Sti76] G. E. Stillman, C. M. Wolfe, and J. A. Rossi, "Electroabsorption in GaAs and its application to waveguide detectors and modulators," *Appl. Phys. Lett.*, vol. 28, pp. 544-546, 1976.
- [Str79] W. Streifer, R. D. Burnham, and D. R. Scifres, "Symmetrical and asymmetrical waveguiding in very narrow conducting stripe lasers," *IEEE J. Quantum Electron.*, vol. QE-15, pp. 136-141, 1979.
- [Str81] W. Streifer, R. D. Burnham, and D. R. Scifres, "Channeled substrate nonplanar laser analysis - Part I: Formulation and the plano-convex waveguide laser," *IEEE J. Quantum Electron.*, vol. QE-17, pp. 736-744, 1981.
- [Str80] W. Streifer, D. R. Scifres, and R. D. Burnham, "Above-threshold analysis of double-heterostructure diode lasers with laterally tapered active regions," *Appl. Phys. Lett.*, vol. 37, pp. 877-879, 1980.
- [Str83] W. Streifer, D. R. Scifres, and R. D. Burnham, "Diode laser threshold current density and lasing wavelength as functions of active region thickness," *Appl. Phys. Lett.*, vol. 42, pp. 401-403, 1983.
- [Stu62] M. D. Sturge, "Optical absorption of gallium arsenide between 0.6 and 2.75 eV," *Phys. Rev.*, vol. 127, pp. 768-773, 1962.
- [Suz87] M. Suzuki, Y. Noda, H. Tanaka, A. Akiba, Y. Kushiro, and H. Isshiki, "Monolithic integration of InGaAsP/InP distributed feedback laser and electroabsorption modulator by vapor phase epitaxy," *IEEE J. Lightwave Technol.*, vol. LT-5, pp. 1277-1285, 1987.
- [Suz88] M. Suzuki, H. Tanaka, S. Akiba, and Y. Kushiro, "Electrical and optical interactions between integrated InGaAsP/InP DFB lasers and electroabsorption modulators," *IEEE J. Lightwave Technol.*, vol. LT-6, pp. 779-785, 1988.
- [Tak89a] T. Takamori, L. A. Coldren, and J. L. Merz, "A folded-cavity TJS surface emitting laser," *Tech. Dig., Conf. on Integrated and Guided-Wave Optics (IGWO)*, Houston, Texas, Feb. 1989, paper MCC6-1.
- [Tak89b] H. Takeuchi, K. Kasaya, and K. Oe, "Low-switching-voltage InGaAs/InP waveguide interferometric modulator for integrated optics," *IEEE Photon. Technol. Lett.*, vol. 1, pp. 227-229, 1989.
- [Tar86] S. Tarucha and H. Okamoto, "Monolithic integration of a laser diode and an optical waveguide modulator having a GaAs/

AlGaAs quantum well double heterostructure," *Appl. Phys. Lett.*, vol. 48, pp. 1-3, 1986.

[Tha63] K. Tharmalingham, "Optical absorption in the presence of a uniform field," *Phys. Rev.*, vol. 130, pp. 2204-2206, 1963.

[Tho87] R. L. Thornton, J. E. Epler, and T. Paoli, "Monolithic integration of a transparent dielectric waveguide into an active laser cavity by impurity induced disordering," *Appl. Phys. Lett.*, vol. 51, pp. 1983-1985, 1987.

[Tho88] R. L. Thornton, W. J. Mosby, and T. L. Paoli, "Monolithic waveguide coupled cavity lasers and modulators fabricated by impurity induced disordering," *IEEE J. Lightwave Technol.*, vol. LT-6, pp. 786-792, 1988.

[Tie77] P. K. Tien, "Integrated optics and wave phenomena in optical waveguides," *Rev. Mod. Phys.*, vol. 49, pp. 361-420, 1977.

[Tuc85] R. S. Tucker, "High-speed modulation of semiconductor lasers," *IEEE J. Lightwave Technol.*, vol. LT-3, pp. 1180, 1985.

[Tur79] S. E. H. Turley, G. H. B. Thompson, and D. F. Lovelace, "Effect of injection current on the dielectric constant of an inbuilt waveguide in twin-transverse-junction stripe lasers," *Electron. Lett.*, vol. 15, pp. 256-257, 1979.

[Vah83] K. Vahala, L. C. Chiu, S. Margalit, and A. Yariv, "On the linewidth enhancement factor α in semiconductor injection lasers," *Appl. Phys. Lett.*, vol. 42, pp. 631-633, 1983.

[Wad87] O. Wada, "Recent progress in optoelectronic integrated circuits (OEIC's)," *Proc. SPIE*, vol. 797, 1987.

[Wak89] K. Wakita, O. Mitomi, I. Kotaka, S. Nojima, and Y. Kawamura, "High-speed electro-optic phase modulators using InGaAs/InAlAs multiple quantum well waveguides," *IEEE photon. Technol. Lett.*, vol. 1, pp. 441-442, 1989.

[Wak87] K. Wakita, Y. Yoshikuni, and Y. Kawamura, "Highly efficient InGaAs/InAlAs MQW waveguide phase shifter," *Electron. Lett.*, vol. 23, pp. 303-304, 1987.

[Wan87] S. Y. Wang, S. H. Lin, and Y. M. Houng, "GaAs traveling-wave polarization electro-optic waveguide modulator with bandwidth in excess of 20 GHz at 1.3 μm ," *Appl. Phys. Lett.*, vol. 51, pp. 83-85, 1987.

- [Wei87] J. S. Weiner, D. A. B. Miller, and D. S. Chemla, "Quadratic electro-optic effect due to the quantum-confined Stark effect in quantum wells," *Appl. Phys. Lett.*, vol. 50, pp. 842-844, 1987.
- [Wei85] J. S. Weiner, D. B. A. Miller, D. S. Chemla, T. C. Damen, C. A. Burrus, T. H. Wood, A. C. Gossard, and W. Wiegmann, "Strong polarization-sensitive electroabsorption in GaAs/AlGaAs quantum well waveguides," *Appl. Phys. Lett.*, vol. 47, pp. 1148-1150, 1985.
- [Wel87] D. F. Welch, D. R. Scifres, P. S. Cross, and W. Streifer, "Buried heterostructure lasers by silicon implanted, impurity induced disordering," *Appl. Phys. Lett.*, vol. 51, pp. 1401-1403, 1987.
- [Wel82] D. Welford and A. Mooradian, "Output power and temperature dependence of the linewidth of single-frequency cw (GaAl)As diode lasers," *Appl. Phys. Lett.*, vol. 40, pp. 865-867, 1982.
- [Wer89] J. Werner, E. Kapon, N. G. Stoffel, E. Colas, S. A. Schwarz, C. L. Schwartz, and N. Andreadakis, "Integrated external cavity GaAs/AlGaAs lasers using selective quantum well disordering," *Appl. Phys. Lett.*, vol. 55, pp. 540-542, 1989.
- [Whi88] M. Whitehead, P. Stevens, A. Rivers, P. Parry, J. S. Roberts, P. Mistry, M. Pate, and G. Hill, "Effects of well width on the characteristics of GaAs/AlGaAs multiple quantum well electroabsorption modulators," *Appl. Phys. Lett.*, vol. 53, pp. 956-958, 1988.
- [Woo88] T. H. Wood, "Multiple quantum well (MQW) waveguide modulators," *IEEE J. Lightwave Technol.*, vol. LT-6, pp. 743-757, 1988.
- [Zor73a] J. Zoroofchi and J. K. Butler, "Refractive index of n-type gallium arsenide," *J. Appl. Phys.*, vol. 44, pp. 3697-3699, 1973.
- [Zor73b] P. Zory, "Laser oscillation in corrugated optical waveguides," *Appl. Phys. Lett.*, vol. 22, pp. 125-127, 1973.
- [Zuc88a] J. E. Zucker, T. L. Hendrickson, and C. A. Burrus, "Low-voltage phase modulation in GaAs/AlGaAs quantum well optical waveguides," *Electron. Lett.*, vol. 24, pp. 112-113, 1988.
- [Zuc88b] J. E. Zucker, T. L. Hendrickson, and C. A. Burrus, "Electro-optic phase modulation in GaAs/AlGaAs quantum well waveguides," *Appl. Phys. Lett.*, vol. 52, pp. 945-947, 1988.

BIOGRAPHICAL SKETCH

Sang Sun Lee was born in Seoul, Korea, in 1955. He received the B. S. and M. S. degrees in electronic engineering from the Hanyang University in 1978 and 1983, respectively.

From August 1984, he has been studying in the Department of Electrical Engineering, the University of Florida at Gainesville. From May 1985 to May 1986, he was involved in the development of high-quality silicon-tub devices in the Microelectronics Laboratory. Transferring his research interest to photonic devices in May 1986, he joined the Photonics Research Laboratory in the same department. During the first one and one-half years, he was involved in research on the linewidth and linewidth broadening mechanisms of semiconductor diode lasers. Based on inherent chirps of directly modulated diode lasers, he has been working on the external modulation using double-heterostructure or quantum-well structure phase modulators.

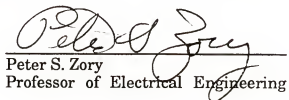
His current research interest includes theoretical and experimental developments of optoelectronic devices such as laser, modulator, coupler, switch, and detector, and their monolithic integrations for optical communication and high-speed signal processing applications.

I certify that I have read this study and that in my opinion it conforms to acceptable standards of scholarly presentation and is fully adequate, in scope and quality, as a dissertation for the degree of Doctor of Philosophy.



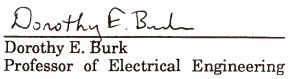
Ramu V. Ramaswamy, Chairman
Professor of Electrical Engineering

I certify that I have read this study and that in my opinion it conforms to acceptable standards of scholarly presentation and is fully adequate, in scope and quality, as a dissertation for the degree of Doctor of Philosophy.



Peter S. Zory
Professor of Electrical Engineering

I certify that I have read this study and that in my opinion it conforms to acceptable standards of scholarly presentation and is fully adequate, in scope and quality, as a dissertation for the degree of Doctor of Philosophy.



Dorothy E. Burk
Professor of Electrical Engineering

I certify that I have read this study and that in my opinion it conforms to acceptable standards of scholarly presentation and is fully adequate, in scope and quality, as a dissertation for the degree of Doctor of Philosophy.



Ramakant Srivastava
Professor of Electrical Engineering

I certify that I have read this study and that in my opinion it conforms to acceptable standards of scholarly presentation and is fully adequate, in scope and quality, as a dissertation for the degree of Doctor of Philosophy.

Timothy J. Anderson
Timothy J. Anderson
Professor of Chemical Engineering

This dissertation was submitted to the Graduate Faculty of the College of Engineering and to the Graduate School and was accepted as partial fulfillment of the requirements for the degree of Doctor of Philosophy.

August 1990

Winfred M. Phillips
Winfred M. Phillips
Dean, College of Engineering

Madelyn M. Lockhart
Dean, Graduate School